

**DEVELOPMENT OF NANOPARTICLE-BASED CONTRAST AGENTS FOR
APPLICATIONS WITH CONVENTIONAL AND PHOTON-COUNTING CT
IMAGING**

Johoon Kim

A DISSERTATION

in

Bioengineering

Presented to the Faculties of the University of Pennsylvania

in

Partial Fulfillment of the Requirements for the

Degree of Doctor of Philosophy

2021

Supervisor of Dissertation

David P. Cormode, D.Phil

Associate Professor of Radiology

Graduate Group Chairperson

Yale E. Cohen, Ph.D., Professor of Otorhinolaryngology

Dissertation Committee

Andrew Tsourkas, Ph.D., Professor of Bioengineering

Peter B. Noël, Ph.D., Assistant Professor of Radiology

Harold I. Litt, M.D., Ph.D., Associate Professor of Radiology

ACKNOWLEDGEMENTS

I would like first to thank my advisor and mentor, Dr. David Cormode, for giving me an opportunity to pursue my passion in the field of nanomedicine and medical imaging as a PhD student. I am very grateful for all of his encouraging words and endless support that allowed me to stay engaged and leap over the hurdles I faced during my PhD studies. I am especially thankful for all his dedication for his trainees, including myself. He always made time to closely guide me whenever I felt lost. I will always be grateful for his mentorship.

I would also like to thank my thesis committee chair and members Dr. Andrew Tsourkas, Dr. Peter Noël, and Dr. Harold Litt for their continuous support and guidance throughout my graduate studies.

I would also like to thank our collaborators, Dr. Peter Noël, Dr. Philippe Douek, Dr. Avery Posey, Dr. Cho-Park, Dr. Tilo Grosser, and their group members for making this work possible.

I would like to thank my friends for their support and for giving me momentary and healthy distractions from my research. Finally, my sincere gratitude to my family for their unparalleled love and support.

ABSTRACT

DEVELOPMENT OF NANOPARTICLE-BASED CONTRAST AGENTS FOR APPLICATIONS WITH CONVENTIONAL AND PHOTON-COUNTING CT IMAGING

Johoon Kim

David P. Cormode

X-ray computed tomography (CT) is one of the most widely used clinical imaging modalities, and recent developments in CT detectors and reconstruction methods are fueling its rapid innovation and expansion of its diagnostic values. However, despite the advancement in nanotechnology and nanoparticle-based contrast agents, small molecule-based iodinated contrast agents with several drawbacks, such as short blood half-lives, low CT contrast generation at high tube potential, and potential adverse effects, remain to be the only FDA approved CT contrast agents for intravascular administration. Development of novel nanoparticle-based CT contrast agents will not only resolve these drawbacks, but also facilitate the emergence of new CT technologies, such as photon-counting CT (SPCCT), and novel CT imaging applications. In this thesis, we present the development of nanoparticles that are specifically designed for numerous CT and SPCCT imaging applications. Sub-5 nm tantalum oxide nanoparticles (TaONP) were developed after investigating CT contrast generation properties and material differentiation of several candidate elements for SPCCT-specific contrast agent. To prolong blood circulation time and improve CT contrast production, TaONP were encapsulated in polymeric nanoparticles along with other sub-5 nm nanoparticles made of cerium (CeONP) and gold (AuNP). These polymeric nanoparticles produced consistently high CT attenuation across

multiple clinical settings and were efficiently degraded into small nanoparticles within 7 days in biological fluids. Our CT contrast generation results also revealed that CeONP were able to produce higher CT contrast when compared to other experimental contrast agents especially at low tube potentials. Understanding that CeONP can also have immunomodulatory properties, we further investigated them as both CT contrast agents and therapeutic agents for targeted imaging and treatment of inflammatory diseases, expanding the potential CT imaging applications. Moreover, 85 % of the injected dose were excreted within 24 hours of intravenous injection, indicating CeONP's feasibility of clinical translation. To further expand the CT imaging applications to cell tracking, sub-5 nm AuNP were encompassed in lipid-based transfection reagents to label chimeric antigen receptor (CAR)-T cells to monitor their behavior in cancer immunotherapy against solid tumors. This work highlights key considerations in the development of CT and SPCCT-specific contrast agents and the potential use of nanoparticle-based contrast agents for broadening CT and SPCCT imaging applications.

TABLE OF CONTENTS

CHAPTER 1: INTRODUCTION TO APPLICATIONS OF NANOPARTICLE-BASED CONTRAST AGENTS FOR CT IMAGING AND OTHER BIOMEDICAL APPLICATIONS.....	1
1.1 INTRODUCTION	1
1.2 BACKGROUND	2
1.2.1 X-RAY COMPUTED TOMOGRAPHY	2
1.2.1.1 CT PRINCIPLES	3
1.2.1.2 SPECTRAL PHOTON COUNTING CT TECHNOLOGY.....	9
1.2.2 NANOPARTICLE CONTRAST AGENTS FOR CT AND SPCCT IMAGING	12
1.2.2.1 IODINATED CONTRAST AGENTS	12
1.2.2.2 NANOPARTICLE-BASED CT CONTRAST AGENTS	13
1.2.2.3 NANOPARTICLE-BASED SPCCT CONTRAST AGENTS	15
1.2.3. OTHER BIOMEDICAL APPLICATIONS OF METAL-BASED NANOPARTICLES	17
1.2.3.1 CT CELL TRACKING	17
1.2.3.2 ROS SCAVENGER FOR IMMUNOMODULATION	17
1.3 CONCLUSION	18
1.4 REFERENCES	19
CHAPTER 2: ASSESSMENT OF CANDIDATE ELEMENTS FOR DEVELOPMENT OF ULTRASMALL NANOPARTICLE-BASED PHOTON-COUNTING CT CONTRAST AGENTS.....	28
2.1 ABSTRACT.....	28
2.2 INTRODUCTION	29
2.3 MATERIALS AND METHODS	33
2.3.1 MATERIALS.....	33
2.3.2 CT AND SPCCT SYSTEMS.....	34
2.3.3 SPCCT PHANTOM IMAGING AND IMAGE ANALYSIS	35
2.3.4 MATERIAL DECOMPOSITION AND IMAGE RECONSTRUCTION METHOD	37
2.3.5 TANTALUM OXIDE NANOPARTICLE SYNTHESIS.....	38
2.3.6 NANOPARTICLE CHARACTERIZATION	39
2.3.7 <i>IN VITRO</i> CYTOTOXICITY EXPERIMENT	39
2.3.8 STATISTICAL ANALYSIS	40
2.4 RESULTS.....	40
2.4.1 PHANTOM IMAGING	40
2.4.2 ATTENUATION RATE	41
2.4.3 CONTRAST-TO-NOISE RATIO RATE AND NOISE	44
2.4.4 TANTALUM OXIDE NANOPARTICLE SYNTHESIS AND CHARACTERIZATION	47
2.4.5 <i>IN VITRO</i> CYTOTOXICITY OF TANTALUM OXIDE NANOPARTICLES	48
2.4.6 SPCCT PHANTOM IMAGING OF TANTALUM OXIDE NANOPARTICLES.....	49
2.5 DISCUSSION	50
2.6 CONCLUSION	55
2.7 REFERENCES	57

CHAPTER 3: DEVELOPMENT OF POLYMER-ENCAPSULATED “POLYMETAL” NANOPARTICLES FOR CT IMAGING.....	68
3.1 ABSTRACT.....	68
3.2 INTRODUCTION.....	69
3.3 MATERIALS AND METHODS.....	72
3.3.1 MATERIALS.....	72
3.3.2 GOLD NANOPARTICLE SYNTHESIS.....	73
3.3.3 TANTALUM OXIDE NANOPARTICLE SYNTHESIS.....	74
3.3.4 CERIUM OXIDE NANOPARTICLE SYNTHESIS.....	74
3.3.5 POLYMETAL NANOPARTICLE SYNTHESIS.....	75
3.3.6 NANOPARTICLE CHARACTERIZATION.....	76
3.3.7 EDS ELEMENTAL MAPPING.....	77
3.3.8 <i>IN VITRO</i> POLYMETAL NANOPARTICLE DEGRADATION STUDY.....	77
3.3.9 <i>IN VITRO</i> CYTOTOXICITY ASSESSMENT.....	78
3.3.10 <i>IN VITRO</i> PHANTOM CT IMAGING.....	78
3.3.11 SIMULATION OF PAYLOAD ELEMENT CONTRIBUTION TO CT ATTENUATION.....	80
3.3.12 <i>IN VIVO</i> MICE IMAGING.....	80
3.3.13 STATISTICAL ANALYSIS.....	81
3.4 RESULTS.....	81
3.4.1 CORE NANOPARTICLES SYNTHESIS AND CHARACTERIZATION.....	81
3.4.2 <i>IN VITRO</i> CYTOTOXICITY OF CORE NANOPARTICLES.....	82
3.4.3 ENCAPSULATION OF CORE NANOPARTICLES FOR POLYMETAL NANOPARTICLE SYNTHESIS.....	83
3.4.4 SPATIAL DISTRIBUTION OF CORE NANOPARTICLES IN POLYMETAL NANOPARTICLES.....	87
3.4.5 SIZE CONTROL OF POLYMETAL NANOPARTICLES.....	88
3.4.6 <i>IN VITRO</i> BIODEGRADABILITY.....	88
3.4.7 <i>IN VITRO</i> CYTOTOXICITY OF POLYMETAL NANOPARTICLES.....	89
3.4.8 <i>IN VITRO</i> CT CONTRAST GENERATION.....	90
3.4.9 RELATIVE CONTRIBUTION TO CT ATTENUATION.....	94
3.4.10 <i>IN VIVO</i> CONTRAST GENERATION.....	95
3.5 DISCUSSION.....	96
3.6 CONCLUSION.....	100
3.7 REFERENCES.....	101
CHAPTER 4: CITRIC ACID COATED CERIUM OXIDE NANOPARTICLES FOR DETECTION AND TREATMENT OF INFLAMMATORY DISEASES.....	109
4.1 ABSTRACT.....	109
4.2 INTRODUCTION.....	110
4.3 MATERIALS AND METHODS.....	113
4.3.1 MATERIALS.....	113
4.3.2 SYNTHESIS OF CITRIC ACID COATED CEONP.....	113
4.3.3 NANOPARTICLE CHARACTERIZATION.....	114
4.3.4 <i>IN VITRO</i> PHANTOM CT IMAGING.....	114
4.3.5 <i>IN VITRO</i> CYTOTOXICITY.....	115
4.3.6 SUPEROXIDE DISMUTASE AND CATALASE MIMETIC ACTIVITY ASSAYS.....	116
4.3.7 INTRACELLULAR ROS AND RNS (REACTIVE NITROGEN SPECIES) PRODUCTION LEVEL.....	116
4.3.8 PRO- AND ANTI-INFLAMMATORY MRNA EXPRESSION.....	117
4.3.9 MACROPHAGE CELLULAR UPTAKE ASSAY.....	118

4.3.10 WESTERN BLOTTING ANALYSIS	118
4.3.10 <i>IN VIVO</i> STUDIES	119
4.3.10.1 PERIPHERAL INFLAMMATION MODEL INDUCTION AND PAW EDEMA THICKNESS	119
4.3.10.2 BEHAVIORAL TESTING: THERMAL PAIN HYPERSENSITIVITY	120
4.3.10.3 BIODISTRIBUTION	120
4.3.11 EX VIVO STUDIES	121
4.3.11.1 RENAL CLEARANCE OF CEONP	121
4.3.11.2 <i>IN VIVO</i> TOXICITY	121
4.3.11.3 <i>IN VIVO</i> IMMUNOMODULATORY EFFECT OF CEONP	121
4.3.12 STATISTICAL ANALYSIS	121
4.4 RESULTS.....	122
4.4.1 SYNTHESIS AND CHARACTERIZATION OF CITRIC ACID COATED CEONP	122
4.4.2 <i>IN VITRO</i> CYTOCOMPATIBILITY	123
4.4.3 <i>IN VITRO</i> CONTRAST GENERATION	125
4.4.4 ENZYME-MIMETIC ANTIOXIDATIVE ACTIVITIES	126
4.4.5 <i>IN VITRO</i> ROS AND RNS SCAVENGING ACTIVITIES	127
4.4.6 <i>IN VITRO</i> ANTI-INFLAMMATORY EFFECT	129
4.4.7 <i>IN VIVO</i> IMMUNOMODULATORY EFFECT	131
4.4.8 BIODISTRIBUTION AND RENAL CLEARANCE	139
4.4.9 <i>IN VIVO</i> TOXICITY	141
4.5 DISCUSSION	142
4.6 CONCLUSION	146
4.7 REFERENCES	147
CHAPTER 5: LABELING SOLID TUMOR TARGETING CAR-T CELLS FOR CT AND SPCCT CELL TRACKING IN CANCER IMMUNOTHERAPY.....	156
5.1 ABSTRACT.....	156
5.2 INTRODUCTION	157
5.3 MATERIALS AND METHODS	158
5.3.1 MATERIALS.....	158
5.3.2 GOLD NANOPARTICLE TRANSFECTION AGENT SYNTHESIS	159
5.3.3 NANOPARTICLE CHARACTERIZATION	159
5.3.4 CAR-T CELL CULTURE AND LABELING	159
5.3.5 CELLULAR UPTAKE	160
5.3.6 <i>IN VITRO</i> VIABILITY AND CAR-T CELL FUNCTION ASSAYS	160
5.3.7 CT AND SPCCT PHANTOM IMAGING OF LABELED CAR-T CELLS.....	160
5.4 RESULTS.....	161
5.4.1 CAR-T CELL TRANSFECTING GOLD NANOPARTICLE SYNTHESIS AND CHARACTERIZATION	161
5.4.2 SELECTION OF CAR-T CELL LABELING CONDITIONS	161
5.4.3 <i>IN VITRO</i> CELLULAR FUNCTIONS.....	164
5.4.4 <i>IN VITRO</i> CT AND SPCCT PHANTOM IMAGING OF LABELED CAR-T CELLS.....	165
5.5 DISCUSSION	166
5.6 CONCLUSION	167
5.7 REFERENCES	168
CHAPTER 6: OVERALL DISCUSSION AND FUTURE DIRECTIONS	171
6.1 OVERALL DISCUSSION	171
6.1.1 OVERVIEW.....	171

6.1.2 ROAD TO CLINICAL TRANSLATION FOR NANOPARTICLE-BASED CT AND SPCCT CONTRAST AGENTS	173
6.1.3 EXPANDING CT APPLICATIONS: TARGETED CT AND SPCCT IMAGING	175
6.1.4 EXPANDING CT APPLICATIONS: CELL TRACKING.....	177
6.2 FUTURE DIRECTIONS	179
6.2.1 OVERVIEW.....	179
6.2.2 RENALLY CLEARABLE CEONP AS SPCCT CONTRAST AGENTS	179
6.2.3 <i>IN VIVO</i> CAR-T CELL TRACKING IN CANCER IMMUNOTHERAPY	180
6.3 CONCLUDING REMARKS	181
6.4 REFERENCES	182
LIST OF PUBLICATIONS	187

LIST OF TABLES

Table 1.1 Summary of the properties and the potential for SPCCT contrast agent development of candidate heavy metal elements.	17
Table 2.1 R^2 value of AR in all six elements in the phantom study.....	42
Table 2.2 T-values of every possible pair of elements in two sample T-test for AR.....	42
Table 2.3 R^2 value of CNRR in all six elements in the phantom study.	45
Table 2.4 T-values of every possible pairs of elements in two sample T-test for CNRR in element specific images of SPCCT.	46

LIST OF FIGURES

Figure 1.1 Sources of X-ray generation.	4
Figure 1.2 Sources of X-ray attenuation.	5
Figure 1.3 K-edge energies of various elements.....	6
Figure 1.4 CT image reconstruction techniques.....	7
Figure 1.5 Material differentiation in SPCCT imaging.	9
Figure 1.6 Schematic depiction of an SPCCT system.....	11
Figure 2.1 Candidate heavy metal elements for SPCCT contrast agent development. ...	32
Figure 2.2 Specifications and photograph of the prototype SPCCT scanner used in this study.	34
Figure 2.3 SPCCT phantom design and images.....	36
Figure 2.4 Attenuation rates of candidate elements from SPCCT system.....	41
Figure 2.5 Comparison in AR between CT and SPCCT systems.....	43
Figure 2.6 CNR rates of candidate elements from SPCCT system.	44
Figure 2.7 Noise level of candidate elements.	47
Figure 2.8 Synthesis and physiochemical characteristics of TaONP.....	48
Figure 2.9 Effect of TaONP on cell <i>viability</i> after 8 hr of incubation.	49
Figure 2.10 SPCCT imaging of TaONP.	50
Figure 3.1 Contrast generating materials and structure of PMNP.	71
Figure 3.2 Schematic depiction of small glutathione-coated AuNP synthesis.....	73
Figure 3.3 Schematic depiction of poly(acrylic acid)-coated CeONP synthesis.....	75
Figure 3.4 Schematic illustration of PMNP synthesis using a microfluidic chip mixer.	76
Figure 3.5 Characterization of small core metal nanoparticles of PMNP.....	82
Figure 3.6 <i>In vitro</i> cell <i>viability</i> of small nanoparticles.....	83

Figure 3.7 TEM of SMNP and PMNP.....	86
Figure 3.8 Payload-dependent increase of diameters.....	86
Figure 3.9 Encapsulation of small core nanoparticles in PMNP.	87
Figure 3.10 Relationship between size of PMNP and amount of PEG-PLL during synthesis.	88
Figure 3.11 Release of small core nanoparticles from PMNP <i>in vitro</i>	89
Figure 3.12 Cell <i>viability</i> after SMNP and PMNP treatment.	90
Figure 3.13 <i>In vitro</i> contrast generation of PMNP and SMNP in μ CT imaging.	91
Figure 3.14 <i>In vitro</i> contrast generation of PMNP and SMNP in clinical CT imaging.	92
Figure 3.15 CT contrast properties of PCPP formulations.....	94
Figure 3.16 Relative attenuation contribution of gold, tantalum, and cerium to PMNP. ...	95
Figure 3.17 <i>In vivo</i> images and contrast generation analysis.....	96
Figure 4.1 Characterization of citric acid coated CeONP.	123
Figure 4.2 <i>In vitro</i> cytotoxicity of citric acid coated CeONP.	124
Figure 4.3 <i>In vitro</i> contrast generation of CeONP in clinical CT imaging.	125
Figure 4.4 ROS scavenging activities of CeONP.	126
Figure 4.5 Reactive species scavenging activity of CeONP in macrophages.....	128
Figure 4.6 <i>In vitro</i> anti-inflammatory effect of CeONP in LPS-stimulated macrophage cells.	130
Figure 4.7 IL-10 expression of LPS-stimulated RAW 264.7 cells.	131
Figure 4.8 Images of inflamed paws of vehicle injected and CeONP treated mice over 24 h period.	132
Figure 4.9 <i>In vivo</i> edema reduction and suppression of proinflammatory cytokines and macrophage recruitment in acute hind paw inflammation.	133
Figure 4.10 Off-site effect of CeONP treatment.	134
Figure 4.11 <i>In vivo</i> IL-10 expression in mice.....	135

Figure 4.12 Immunofluorescence analysis of pro-inflammatory cytokines and a macrophage marker.	138
Figure 4.13 Immunofluorescence analysis of IL-10 and a macrophage marker.	138
Figure 4.14 Thermal pain hypersensitivity in the hind paw acute inflammation.	139
Figure 4.15 Biodistribution and renal clearance of CeONP.	141
Figure 4.16 <i>In vivo</i> safety of citric acid coated CeONP.	142
Figure 5.1 Morphologies of small AuNP and lipofectamine-encapsulated AuNP.....	161
Figure 5.2 Labeling of AuNP and its effect in CAR-T cell <i>viability</i>	163
Figure 5.3 Cellular functions of labeled CAR-T cells.....	164
Figure 5.4 <i>In vitro</i> phantom images of labeled CAR-T cells.	165

CHAPTER 1: INTRODUCTION TO APPLICATIONS OF NANOPARTICLE-BASED CONTRAST AGENTS FOR CT IMAGING AND OTHER BIOMEDICAL APPLICATIONS

1.1 Introduction

Advances in nanotechnology have allowed us to synthesize particle structures that are nanometers in size, called nanoparticles. It is also feasible to precisely control their physical and chemical properties and to make them stable and biocompatible for use in a range of biomedical applications. These applications include, but are not limited to, delivery of drug and genetic materials, sensitizers for photothermal and radiotherapy, contrast agents for medical imaging, and substitutes for traditional enzymes.

One field of wide interest for nanoparticle application is in development of contrast agents for X-ray computed tomography (CT), which is one of the most commonly used clinical imaging modalities. Its advantages of high spatial resolution and capabilities in quantitative analyses motivated the emergence of new CT techniques, such as photon-counting CT (SPCCT) that can allow material differentiation, and use of CT imaging for numerous imaging applications, such as cell tracking. Combined with the advances in nanoparticle sciences, CT imaging applications are also being expanded to the field of targeted and molecular imaging.

Herein, we propose and develop nanoparticles that are specifically designed for various CT and SPCCT imaging-based applications, ranging from contrast agents, cell tracking probes for cancer immunotherapy, and a theranostic agent for inflammatory diseases. These nanoparticles are made of various heavy metals and are coated with different types of polymers, lipids, and small molecules. The materials as well as the physiochemical properties (i.e., size and surface potential) of the nanoparticles were selected and designed to be suitable for their respective applications. In development of

SPCCT contrast agents, we screened several candidate elements, considered their safety, cost, K-edge energies and others, and developed an ultrasmall nanoparticle formulation made of tantalum that showed high contrast generation in both CT and SPCCT imaging (Chapter 2). We also synthesized a polymer-based large nanoparticle formulation that encapsulates ultrasmall nanoparticles made of three different elements. This nanoparticle design will allow prolonged blood circulation, followed by eventual renal clearance as the polymer degrades to release the small nanoparticles. Inclusion of three different elements whose K-edge energies are spread out in the photon energy spectra used in clinical settings also led to high CT contrast generation in numerous CT scanning parameters used in clinical imaging (Chapter 3).

Instead of using nanoparticles as contrast agents for whole-body or tissue-specific imaging applications, we investigated a method to use the nanoparticles to label specific cells in cell-based therapy. For this, we developed gold nanoparticles that are encapsulated by lipid-based transfection reagents to promote *ex vivo* labeling of CAR-T cells, and thus allowing CAR-T cell tracking in cancer immunotherapy (Chapter 4). Some nanoparticle formulations, such as cerium oxide nanoparticles, are also known to have catalytic properties that can be exploited for therapeutic benefits. Therefore, we examined cerium oxide nanoparticles' potential use for both CT imaging and immunomodulation in acute inflammation (Chapter 5).

1.2 Background

1.2.1 X-ray computed tomography

CT is an X-ray based medical imaging technique that was first brought into clinical use in the 1970s.¹ CT imaging is now being widely used for diagnosis and monitoring of

numerous medical conditions such as trauma, cancer, cardiovascular diseases, and gastrointestinal disorders. Its quick image acquisition time and wide clinical availability also allowed it to be extensively used in emergency medicine. CT is currently undergoing a period of rapid innovation. More powerful algorithms such as iterative reconstruction and model-based iterative reconstruction have been developed for improved image quality.²⁻⁵ The speed of image acquisition is being further improved, and new innovations such as dual energy CT systems that can provide spectral information in the image have also become available.

1.2.1.1 CT principles

A typical CT scanner has an X-ray source that emits a beam of photons toward the opposite side of the scanner where an array of detector modules is positioned to absorb transmitted X-ray photons that are not absorbed or scattered by the subject. CT images are typically acquired by placing the subject placed on a bed that moves into the scanner as the source and the detector rotate around the subject to collect 360° data sets.

X-rays are generated in the source when electrons accelerated from a cathode collide with a metal anode, resulting in Bremsstrahlung and characteristic radiation. For Bremsstrahlung radiation, the accelerated electrons interact with the nuclei of the anode and lose some of their kinetic energy *via* X-ray photon emission (Figure 1.1A). In characteristic radiation, the incident electron collides and ejects an inner electron of the anode atom. Subsequently, an electron from an outer orbital fills the vacancy while emitting some of its energy as an X-ray photon (Figure 1.1B). Due to the fixed energy difference between the outer orbitals and the inner orbital, this results in sharp peaks in the X-ray spectrum (Figure 1.1C).

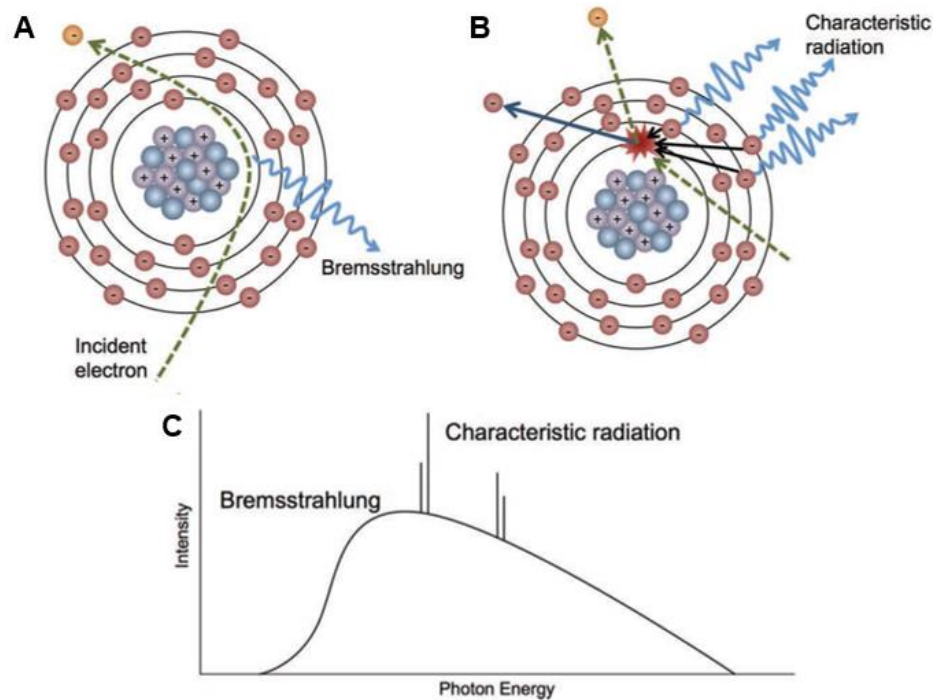


Figure 1.1 Sources of X-ray generation.

Schematic depictions of (A) Bremsstrahlung radiation and (B) characteristic radiation. (C) Typical photon energy spectrum emitted from a CT scanner. Reproduced with permission from Lee *et al.*⁶

The X-rays emitted from the tube are directed at the subject where some of the beam is absorbed and scattered, while the remainder continues toward the detector. The loss of X-ray intensity from absorption and scattering by the patient is referred to as X-ray attenuation. X-rays are attenuated by three types of interactions, namely, Compton scattering, the photoelectric effect, and coherent scattering. At the typical energy levels used in CT scans (~25 to 150 keV), the photoelectric effect and Compton scattering are the two main forms of interactions that cause attenuation.^{6, 7} The photoelectric effect occurs when incident X-rays collide and transfer their energies to inner shell electrons (K-

shell or L-shell) of atoms that constitute the subject, ejecting them from the atom as a result (Figure 1.2A).

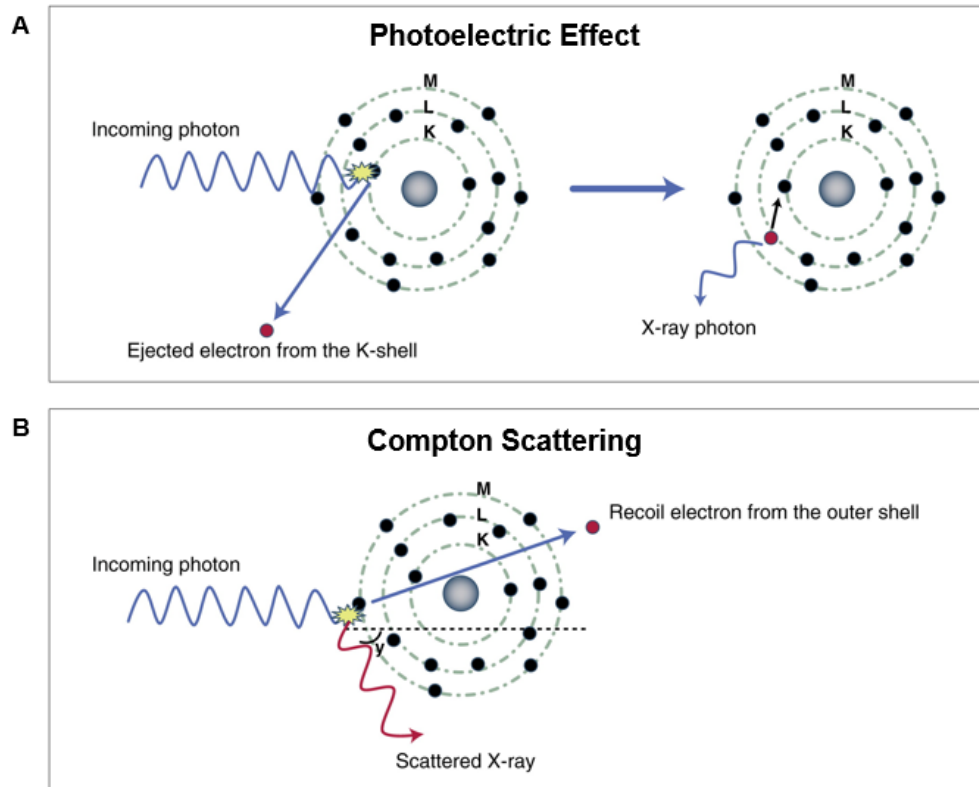


Figure 1.2 Sources of X-ray attenuation.

Schematic depictions of (A) the photoelectric effect and (B) Compton scattering. Reproduced with permission from Danad *et al.*⁸

An electron from the outer electron shell then fills the vacancy and releases a photon, whose energy is characteristic to the atom. The probability of the occurrence of photoelectric effect is generally proportional to Z^3 (Z = atomic number), explaining the considerable research interest in developing CT contrast agents based on high- Z elements. Note that the photoelectric effect can only occur above the binding energy of the K-shell electrons. In addition, the probability of such an event is maximal at the energy

of the K-shell and declines as the energy increases beyond the K-shell, creating features in element X-ray attenuation spectra known as K-edge (Figure 1.3). In Compton scattering, incident X-ray photons interact with weakly bound electrons in the outer shell, lose some of their energy, and are deflected from their original path with reduced energy (Figure 1.2B). The deflection from their original path, as well as the need for collimation at the detectors, mean that Compton scattering is a cause of attenuation. Since Compton scattering occurs between photons and outer electrons, it is primarily affected by the electron density of the atom.⁶

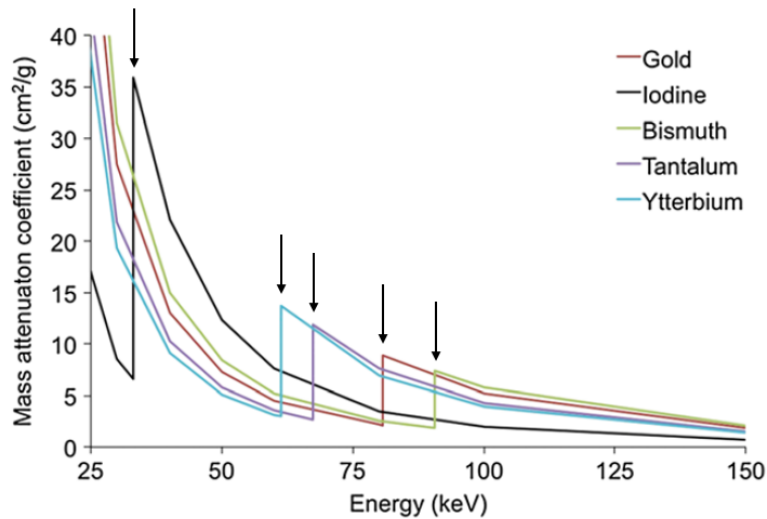


Figure 1.3 K-edge energies of various elements.

Mass attenuation coefficients of various elements where the K-edges are clearly apparent (spikes in the attenuation coefficient curves at certain energies indicated by down arrows).

Figure reproduced with permission from Cormode *et al.*⁷

CT attenuation is given in Hounsfield units (HU). For a given material X, $HU = 1000(\mu_X - \mu_{water})/(\mu_{air} - \mu_{water})$ where μ is the attenuation coefficient. Air therefore has a CT attenuation of -1000 HU and the attenuation of water is 0 HU. The attenuation of bone

ranges from 400 to 1000 HU, and most soft tissues have attenuation of about 40 to 80 HU.⁷ The energies and number of X-ray photons in the beam mainly depend on the maximum tube voltage and electric current used. The maximum photon energy is equivalent to the maximum tube voltage, and the number of photons is inversely proportional to the energy (except at the characteristic energies of the anode material). However, low-energy X-ray photons are easily absorbed in the anode and filters, eliminating X-rays in the 0–25 keV range and reducing the number of X-rays in the 25–50 keV range (Figure 1.1C). In addition, absorption of lower energy photons within the patient can occur, creating an effect known as beam hardening. Once the X-ray beam reaches the detectors, most of the scattered X-ray photons are absorbed in the collimator in front of the detector and X-ray radiation of diagnostic value is absorbed and converted to light in scintillator. The converted light energy in each pixel of the scintillator is then converted into electronic current, which is transmitted as digital output data. From the transmitted data, CT images are reconstructed using computer algorithms. Filtered back-projection algorithms have traditionally been used for reconstruction. However, with recent advancements in computing power, iterative reconstruction methods have been applied, which result in noise reduction and hence improvement in sensitivity (Figure 1.4).^{9, 10}

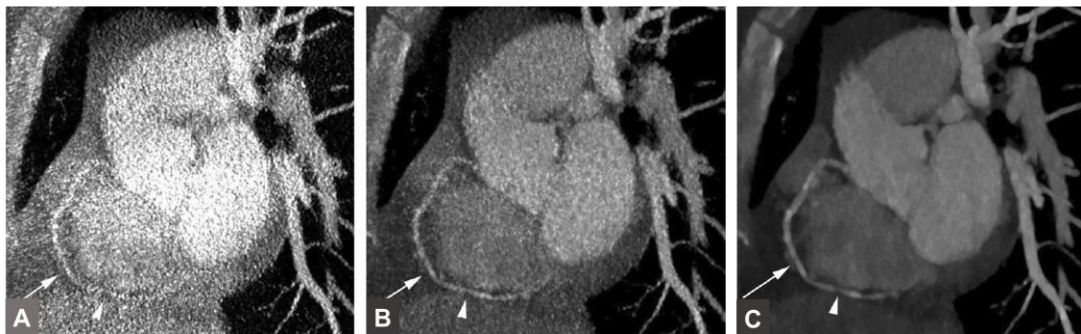


Figure 1.4 CT image reconstruction techniques.

Images of coronary computed tomography angiography of the right coronary artery reconstructed with (A) filtered back projection, (B) hybrid iterative reconstruction (iDose4), and (C) iterative model-based reconstruction. The white arrow points at the right coronary artery, and the white arrowhead points at a noncalcified plaque. The images demonstrate noise reduction of iterative reconstruction when compared to filtered back projection. Figure reproduced with permission from Halpern *et al.*⁹

Post-processing parameters including windowing, slice thickness, and field of view can be adjusted to give optimal image appearance and spatial resolution.¹¹ Recent improvements in detector rows, gantry rotation speed, reconstruction methods, and 3D rendering image processing make CT a powerful tool for diagnostic purposes. Furthermore, recently developed CT systems that use photon-counting detectors can provide energy resolution of the transmitted photons, which allows differentiation of multiple tissues and exogenous contrast agents (Figure 1.5).¹²⁻¹⁴ In order to provide more information in CT imaging, contrast agents are often used. With the photoelectric effect and K-edge attenuation taken into consideration, elements with high atomic numbers and appropriate K-edge energies (i.e., K-edges where there are high numbers of photons in the energy distribution in Figure 1.1C) have good potential to be used as CT contrast agents.

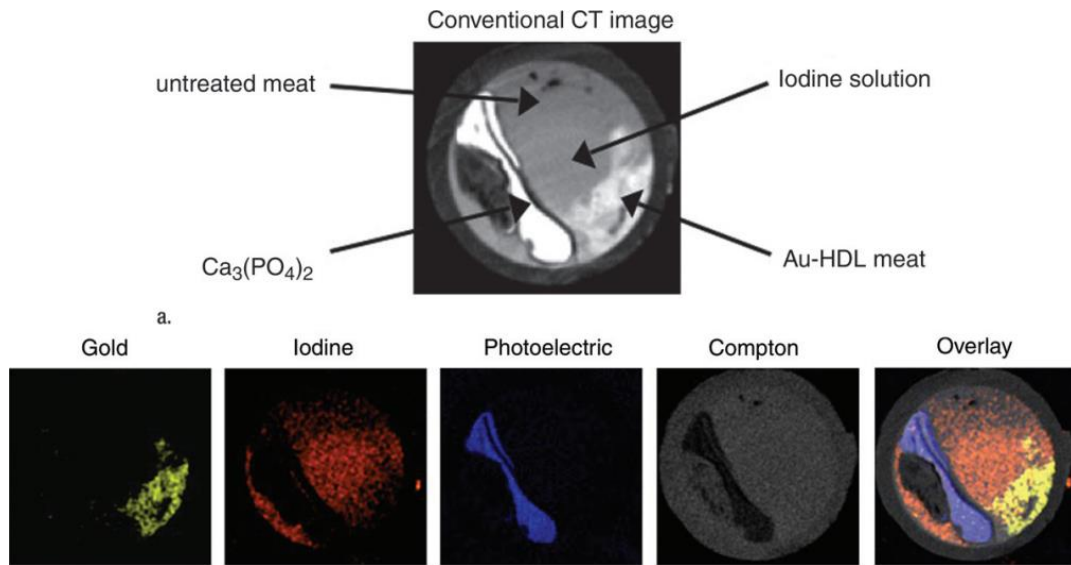


Figure 1.5 Material differentiation in SPCCT imaging.

(A) Conventional CT image of an artery phantom. (B) Gold, iodine, photoelectric, and Compton images of the phantom and an overlay of all four images acquired by spectral CT imaging. Figure reproduced with permission from Cormode *et al.*¹²

1.2.1.2 Spectral photon counting CT technology

The detectors in conventional CT scanner are known as energy-integrating detectors (EIDs), in which all of the energy deposited in each pixel is summed and is transmitted as a single signal. This leads to omission of any energy-dependent information of individual X-ray photons and heavier weighting of higher energy photons, which carry less information on soft tissue contrast. Since CT attenuation is dependent on the mass density and atomic number of the material, materials of different elemental compositions and varying concentrations can produce identical CT attenuation values in EIDs, making differentiation of such materials extremely difficult.

One example of a clinical scenario that could benefit from material differentiation is separation of calcified plaques from the lumen of iodine-filled blood vessels. Calcium deposits within vulnerable atherosclerotic plaques and bones near plaque sites not only obscure the lumen anatomy, but can also generate similar CT attenuation as iodine-filled blood vessels to hinder clear visualization of the plaques, increasing the chance of misdiagnoses. Material differentiation imaging methods that can resolve such issues are highly attractive. One method that allows material differentiation is dual energy CT (DECT) imaging. The principle of DECT is to acquire two sets of CT data using two different energy spectra. This idea was first introduced and demonstrated in the 1970s, although the speed of image acquisition at that time was not sufficient for clinical implementation. Since then, multiple approaches have been developed for clinical use, such as slow kVp switching, rapid kVp switching, and using multilayer detectors or dual X-ray sources.¹⁵ DECT techniques are FDA approved, and clinical CT scanners with two energy spectra are commercially available.¹⁶ Many clinical applications of DECT also have been studied, including virtual monoenergetic imaging for optimal contrast-to-noise ratio (CNR) of iodine, bone removal in CT angiography, and virtual non-contrast enhanced images.^{15, 17}

However, DECT techniques still have several limitations including susceptibility to motion, high overlap of energy spectra, and high noise levels in low-energy data. All of these restraints can cause degradation in image quality and inaccurate material differentiation. Moreover, in some forms of DECT, there is increased radiation dose to the patient, since two X-ray tubes are used to scan. A rapidly emerging CT technology, called spectral photon counting CT (SPCCT), that can overcome the limitations of DECT systems is currently under extensive investigation for its clinical feasibility. Since its first evaluation in preclinical CT systems about a decade ago, the latest prototypes of SPCCT scanners

have evolved to be based on modified clinical CT systems.¹⁸ SPCCT uses a standard polychromatic X-ray source and photon-counting detectors (PCDs) that can potentially provide more accurate material decomposition (Figure 1.6). PCDs are composed of semiconductor materials such as cadmium zinc telluride or silicon. When an X-ray photon is absorbed by these detectors, electron hole pairs are formed, resulting in a charge cloud and current pulse whose magnitude is proportional to the photon energy. The magnitude of each current pulse is measured by the electronics and each X-ray photon event is recorded in one of several energy bins. The number of bins and their energy thresholds can be adjusted for user-specific applications (e.g., near the K-edge of the specific material of interest) (Figure 1.6).¹⁹

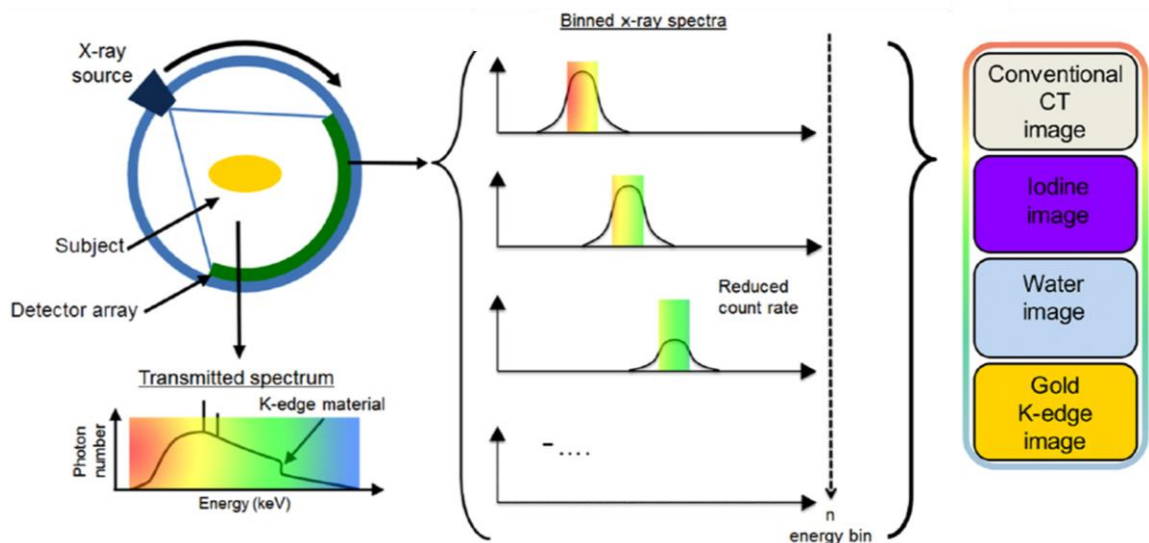


Figure 1.6 Schematic depiction of an SPCCT system.

The binned data may be used to generate different types of image sets such as those listed (i.e., synthesized conventional CT images and iodine, water, and gold material

specific images) or other sets of images. Figure adapted with permission from Cormode *et al.*²⁰

These data sets are then processed together to provide a set of images, which typically include a conventional image and material-specific images (e.g., water, iodine, and gold) (Figure 1.6). SPCCT systems have several benefits, such as lower noise levels, improved CNR and spectral separation, higher spatial resolution, fewer image artifacts, and increased geometric and dose efficiency.^{14, 21, 22} Another benefit of SPCCT imaging is that they can provide absolute quantification of exogeneous contrast agents *in vivo*, which can be utilized in targeted or molecular imaging.¹⁸ Recent studies have demonstrated the feasibility of differentiating multiple materials in both small and large animals.^{12, 23, 24} In addition, the clinical emergence of SPCCT technology has been embraced by multiple studies demonstrating comparable image quality between conventional CT and SPCCT scanners in terms of noise levels and CNR.²⁵⁻²⁸

1.2.2 Nanoparticle contrast agents for CT and SPCCT imaging

1.2.2.1 Iodinated contrast agents

The most commonly used CT contrast agent in contrast-enhanced CT imaging are small molecule-based iodinated contrast agents, such as iopamidol or iodixanol.²⁹ However, they are numerous drawbacks, such as short blood half-lives, non-specificity, and low CT contrast generation at high tube potential imaging. Moreover, these contrast agents are known to cause further reduction in kidney function in patients with renal insufficiency through contrast-induced nephropathy (CIN).^{16, 30, 31} Contrast-induced abnormalities result in morbidity, mortality, and cost. The numbers of populations with

cardiovascular diseases and renal insufficiency are both growing and are expected to grow continuously.³² Thus, there is a compelling need to develop novel CT contrast agents.

1.2.2.2 Nanoparticle-based CT contrast agents

Despite the disadvantages of iodinated contrast agents, there has not been a new CT contrast agent clinically approved for over 20 years. The development of nanoparticle contrast agents can effectively overcome the issues of iodinated small molecules. Nanoparticles of 3 nm, for example, could contain hundreds of contrast generating atoms, which would place a lower burden on the kidneys since far fewer excretion events would be needed. Alternatively, nanoparticles can be designed to erode slowly, resulting in gradual release of their payload for excretion, minimizing the concentration at the kidneys at any given time.^{33, 34} Nanoparticles made of dense, heavy metals with high payloads have been the focus of novel nanoparticle CT contrast agent development to overcome the low sensitivity of CT. These nanoparticles are often designed to be less than 6 nm in hydrodynamic diameter to lower the body retention and thus to increase their potential for clinical translation. Most reported nanoparticles are approximately spherical, but they can have many other shapes, such as rods,³⁵ cages,³⁶ or stars.³⁷ The shape of a nanoparticle can strongly influence its properties; for example, the shape of a gold nanoparticle can determine its suitability for applications such as optical imaging or surface enhanced Raman spectroscopy,^{35, 38, 39} although shape should not affect CT contrast generation.

Nanoparticle CT contrast agents typically consist of a core loaded with contrast generating atoms, which is coated with polymers, lipids, proteins, silica, or other compounds that can provide the desired circulation times, biodistribution, stability and

solubility in biological media, and biocompatibility. The coating layers can also be easily modified to incorporate other functionalities, such as target specificity with antibodies, therapeutic effects *via* drugs or genetic materials, or multimodal imaging capacity with other contrast generating moieties.^{40, 41} Nanoparticles may therefore also be synthesized to possess desired properties and to provide versatility and multifunctionality.⁴² Lipid-based structures (liposomes, emulsions, micelles, or lipoproteins) and solid core nanoparticles (metal, metal alloy, or metal salt) or combinations of the two are the most frequently studied formations for CT applications.^{43, 44} For metal core-based agents, gold nanoparticles have been the most extensively studied as CT contrast agents, due to gold's high atomic number of 79 and K-edge at 80.7 keV, its excellent biocompatibility, bioinertness, synthetic control over size and shape, as well as ease of surface modification.^{45, 46} Other heavy metal elements, such as bismuth, tantalum, platinum, ytterbium, yttrium, gadolinium, and tungsten, have also been studied.^{7, 47, 48}

Nanoparticles are widely studied for vascular imaging as blood pool CT contrast agents since they can be engineered to have long circulation times.^{43, 48} They have also garnered significant research interest for cancer imaging *via* both passive and active targeting. By conjugating various targeting moieties to nanoparticles, targeted imaging of lymph nodes and cardiovascular diseases have been previously demonstrated.⁴⁹ Nanoparticle CT contrast agents can also be used for concurrent diagnosis and therapy by loading therapeutic cargoes or by exploitation of inherent therapeutic properties, such as photothermal ablation using gold nanorods and reduction of oxidative stress using cerium oxide nanoparticles.^{50, 51}

1.2.2.3 Nanoparticle-based SPCCT contrast agents

Nanoparticle-based contrast agents also have high potential to be developed as contrast agents for SPCCT imaging, which is an area in SPCCT imaging that can significantly contribute to the improvement of diagnostic quality of SPCCT images. While iodine-based contrast agents provide sufficient contrast in both single energy CT and DECT imaging, they suffer from low contrast generation at higher X-ray tube potentials that are needed for large adults (e.g., 140 kVp). Moreover, they do not take full advantage of the robust material decomposition capabilities of SPCCT imaging because of iodine's low K-edge energy (33.2 keV). Most photons whose energy levels are lower than or near the K-edge energy of iodine are absorbed by the filter and the patient. For this reason, there are not enough photons in transmitted X-ray spectra below iodine's K-edge energy for accurate K-edge imaging. Novel SPCCT contrast agents will need to be specifically designed for the imaging technique in order to overcome the limitations of iodinated contrast agents.

In the development of a novel SPCCT contrast agent, several important factors need to be considered. These considerations include safety, manufacturing cost and availability, and the K-edge of the element. A majority of the studies that have investigated SPCCT-specific contrast agent development have focused on gadolinium, ytterbium, tantalum, tungsten, gold, and bismuth, which are some of the elements that satisfy the aforementioned considerations.^{12, 20, 52-55} Other elements that have also been explored include hafnium for its appropriate K-edge energy in the clinical X-ray energy spectra, despite its largely unknown safety profile.^{56, 57} Recent studies have demonstrated that these heavy metal elements perform well not only in conventional CT imaging, but also in K-edge imaging with SPCCT, supporting the feasibility of these elements for possible use

in SPCCT imaging.^{18, 20, 53, 54, 57, 58} These nanoparticles can be designed to have variable circulation times, target specificity and to deliver high payloads to regions of interest to complement the material differentiation capability of SPCCT imaging. They are also less likely to extravasate when compared to small molecule-based contrast agents, improving target to background ratios in blood vessel imaging. Table 1.1 briefly summarizes the properties (e.g., atomic number, K-edge, density) and the potential for SPCCT contrast agent development (e.g., pro/con, development status, and degree of studies for CT and SPCCT contrast agent) of the elements that have been most widely studied for SPCCT imaging.

Element	Atomic number	K-edge (keV)	Density (g/cm ³)	Element price (\$/g) Source: Sigma-Aldrich	Pro/con	Development status	Degree of studies for CT contrast agent
Iodine	53	33.17	4.9	8.40	Pro: Clinically approved for contrast-enhanced CT imaging; excellent safety profile Con: Concern over renal damage and allergic reactions; low K-edge for photon-counting CT imaging; sharp decrease in attenuation generation in higher tube potentials	Iodinated contrast agents are clinically available	Well-studied in human subjects; commonly used as a control for contrast enhanced CT imaging
Gadolinium	64	50.24	7.9	10.40	Pro: K-edge close to mean photon energy in clinical X-ray spectra; chelates are FDA approved for clinical MRI imaging. Con: Toxicity concern over nephrogenic systemic fibrosis and accumulation in the bones, brain and kidneys	Gadolinium chelates are clinically available for MRI imaging; are under clinical trial for CT imaging with low dose	Well-studied for MRI imaging; studies in CT imaging and SPCCT imaging.
Ytterbium	70	61.33	6.9	23.00	Pro: K-edge close to mean photon energy in clinical X-ray spectra Con: Unknown safety profile and efficacy in <i>in vivo</i> CT imaging	Preclinical CT and SPCCT imaging with small animals	Several studies in CT imaging and SPCCT imaging in preclinical stage
Hafnium	72	65.35	13.3	4.50	Pro: K-edge close to mean photon energy in clinical X-ray spectra Con: Unknown safety profile and yet unexplored for bioapplication	Preclinical SPCCT imaging with small animals	One experimental study in SPCCT imaging
Tantalum	73	67.42	16.4	6.20	Pro: K-edge close to mean photon energy in clinical X-ray spectra; well-studied for CT imaging; chemically inert; biocompatible; high elemental density Con: Unknown toxicity and safety profile in human patients	Preclinical CT and SPCCT imaging with small animals	Several studies for CT imaging and SPCCT imaging in preclinical stage
Gold	79	80.72	19.3	298.00	Pro: K-edge close to mean photon energy in high clinical X-ray spectra; high density; high biocompatible; highly bioinert; easy synthesis and size and shape control; very well-studied in the field of nanomedicine Con: Expensive	Preclinical CT and SPCCT imaging with small animals	Most well-studied and characterized for CT and SPCCT contrast agent at experimental and preclinical stage
Bismuth	83	90.53	9.8	0.48	Pro: Fairly biocompatible (currently used in gastrointestinal treatments); cheap; effective attenuation generation at higher tube potentials Con: low density compared to other high Z metals	Preclinical CT and SPCCT imaging with small animals	Numerous studies for CT and SPCCT imaging in preclinical stage

Table 1.1 Summary of the properties and the potential for SPCCT contrast agent development of candidate heavy metal elements.

1.2.3. Other biomedical applications of metal-based nanoparticles

1.2.3.1 CT cell tracking

CT has recently emerged as an imaging modality for cell tracking applications due to its appealing characteristics for such applications. CT has no depth penetration limit, has fast temporal resolution, is relatively low cost, and provides quantitative information on contrast agents *in vivo*. CT cell tracking also has substantial clinical potential as CT scanners are widely available in hospitals and research facilities. Recent developments in CT detectors,⁵⁹ reconstruction algorithms,¹⁰ and contrast agents⁷ have also improved the sensitivity of CT, which has been an issue for using CT for cell tracking. The development of cell tracking for CT is a recent technological development for the cell tracking field; however, numerous studies have demonstrated the feasibility of tracking microencapsulated cells, tumor cells, stem cells, and immune cells from CT imaging. SPCCT has also been utilized for cell tracking applications as well, exploiting its unique capability to accurately quantify exogenous contrast agent *in vivo*.⁶⁰

1.2.3.2 ROS scavenger for immunomodulation

Nanoparticles made of certain elements, such as cerium, copper,⁶¹ manganese,⁶² have catalytic activities to effectively scavenge reactive oxygen species and other free radicals. Since excessive free radicals and oxidative stress are key factors in progression of inflammation and tissue injury, these catalytic nanoparticles have been studied to modulate immune responses. Among the elements that can form metal oxide

nanoparticles, cerium has the highest atomic number ($Z = 58$) and K-edge energy that is much higher than that of iodine (40.4 keV vs. 33.2 keV). Cerium's K-edge energy is also located in the region of high photon generation in clinical CT spectra, hinting at its potential use in both CT and SPCCT imaging.

1.3 Conclusion

Recent advancements in both CT techniques and nanotechnology open an opportunity to develop nanoparticle-based CT contrast agents that can overcome current limitations of iodinated small molecule contrast agents and conventional CT systems and improve the diagnostic qualities of CT imaging. Additional benefits from the emergence of SPCCT, such as absolute quantification of exogenous contrast agents, and the ability to control the physiochemical properties of nanoparticles can further broaden the CT imaging applications beyond patient diagnoses. In the following chapters, we present the development of various nanoparticle designs for SPCCT-specific imaging, high contrast generation in various scanning conditions in conventional CT imaging, cell tracking and immunomodulation.

1.4 References

1. Hounsfield, G. N., Computerized transverse axial scanning (tomography). 1. Description of system. *Br J Radiol* **1973**, *46* (552), 1016-1022.
2. Noël, P. B.; Renger, B.; Fiebich, M.; Münzel, D.; Fingerle, A. A.; Rummeny, E. J.; Dobritz, M., Does iterative reconstruction lower CT radiation dose: evaluation of 15,000 examinations. *PLoS One* **2013**, *8* (11), e81141.
3. Bernstein, A. L.; Dhanantwari, A.; Jurcova, M.; Cheheltani, R.; Naha, P. C.; Ivanc, T.; Shefer, E.; Cormode, D. P., Improved sensitivity of computed tomography towards iodine and gold nanoparticle contrast agents *via* iterative reconstruction methods. *Sci Rep* **2016**, *6* (1), 26177.
4. Willemink, M. J.; de Jong, P. A.; Leiner, T.; de Heer, L. M.; Nievelstein, R. A.; Budde, R. P.; Schilham, A. M., Iterative reconstruction techniques for computed tomography Part 1: technical principles. *Eur Radiol* **2013**, *23* (6), 1623-1631.
5. Marin, D.; Nelson, R. C.; Schindera, S. T.; Richard, S.; Youngblood, R. S.; Yoshizumi, T. T.; Samei, E., Low-tube-voltage, high-tube-current multidetector abdominal CT: improved image quality and decreased radiation dose with adaptive statistical iterative reconstruction algorithm--initial clinical experience. *Radiology* **2010**, *254* (1), 145-153.
6. Lee, N.; Choi, S. H.; Hyeon, T., Nano-sized CT contrast agents. *Adv Mater* **2013**, *25* (19), 2641-2660.
7. Cormode, D. P.; Naha, P. C.; Fayad, Z. A., Nanoparticle contrast agents for computed tomography: a focus on micelles. *Contrast Media Mol Imaging* **2014**, *9* (1), 37-52.

8. Danad, I.; Fayad, Z. A.; Willeminck, M. J.; Min, J. K., New applications of cardiac computed tomography: dual-energy, spectral, and molecular CT imaging. *JACC. Cardiovasc imaging* **2015**, *8* (6), 710-723.
9. Halpern, E. J.; Gingold, E. L.; White, H.; Read, K., Evaluation of coronary artery image quality with knowledge-based iterative model reconstruction. *Acad Radiol* **2014**, *21* (6), 805-811.
10. Bernstein, A. L.; Dhanantwari, A.; Jurcova, M.; Cheheltani, R.; Naha, P. C.; Ivanc, T.; Shefer, E.; Cormode, D. P., Improved sensitivity of computed tomography towards iodine and gold nanoparticle contrast agents *via* iterative reconstruction methods. *Sci Rep* **2016**, *6*, 26177.
11. Bardo, D. M.; Brown, P., Cardiac multidetector computed tomography: basic physics of image acquisition and clinical applications. *Curr Cardiol Rev* **2008**, *4* (3), 231-243.
12. Cormode, D. P.; Roessl, E.; Thran, A.; Skajaa, T.; Gordon, R. E.; Schlomka, J. P.; Fuster, V.; Fisher, E. A.; Mulder, W. J.; Proksa, R.; Fayad, Z. A., Atherosclerotic plaque composition: analysis with multicolor CT and targeted gold nanoparticles. *Radiology* **2010**, *256* (3), 774-82.
13. Kalluri, K. S.; Mahd, M.; Glick, S. J., Investigation of energy weighting using an energy discriminating photon counting detector for breast CT. *Med Phys* **2013**, *40* (8), 081923.
14. Bussel, L.; Coulon, P.; Thran, A.; Roessl, E.; Martens, G.; Sigovan, M.; Douek, P., Photon counting spectral CT component analysis of coronary artery atherosclerotic plaque samples. *Br J Radiol* **2014**, *87* (1040), 20130798.

15. McCollough, C. H.; Leng, S.; Yu, L.; Fletcher, J. G., Dual- and multi-Energy CT: principles, technical approaches, and clinical applications. *Radiology* **2015**, *276* (3), 637-653.
16. Yeh, B. M.; FitzGerald, P. F.; Edic, P. M.; Lambert, J. W.; Colborn, R. E.; Marino, M. E.; Evans, P. M.; Roberts, J. C.; Wang, Z. J.; Wong, M. J.; Bonitatibus, P. J., Jr., Opportunities for new CT contrast agents to maximize the diagnostic potential of emerging spectral CT technologies. *Adv Drug Deliv Rev* **2017**, *113*, 201-222.
17. Leithner, D.; Wichmann, J. L.; Vogl, T. J.; Trommer, J.; Martin, S. S.; Scholtz, J. E.; Bodelle, B.; De Cecco, C. N.; Duguay, T.; Nance, J. W., Jr.; Schoepf, U. J.; Albrecht, M. H., Virtual monoenergetic imaging and iodine perfusion maps improve diagnostic accuracy of dual-energy computed tomography pulmonary angiography with suboptimal contrast attenuation. *Invest Radiol* **2017**, *52* (11), 659-665.
18. Si-Mohamed, S.; Bar-Ness, D.; Sigovan, M.; Cormode, D. P.; Coulon, P.; Coche, E.; Vlassenbroek, A.; Normand, G.; Bousset, L.; Douek, P., Review of an initial experience with an experimental spectral photon-counting computed tomography system. *Nucl Instrum Methods Phys Res A* **2017**, *873*, 27-35.
19. Roessl, E.; Herrmann, C., Cramér-Rao lower bound of basis image noise in multiple-energy x-ray imaging. *Phys Med Biol* **2009**, *54* (5), 1307-1318.
20. Cormode, D. P.; Si-Mohamed, S.; Bar-Ness, D.; Sigovan, M.; Naha, P. C.; Balegamire, J.; Lavenne, F.; Coulon, P.; Roessl, E.; Bartels, M.; Rokni, M.; Blevis, I.; Bousset, L.; Douek, P., Multicolor spectral photon-counting computed tomography: *in vivo* dual contrast imaging with a high count rate scanner. *Sci Rep* **2017**, *7* (1), 4784.
21. Leng, S.; Yu, Z.; Halawish, A.; Kappler, S.; Hahn, K.; Henning, A.; Li, Z.; Lane, J.; Levin, D. L.; Jorgensen, S.; Ritman, E.; McCollough, C., Dose-efficient

ultrahigh-resolution scan mode using a photon counting detector computed tomography system. *J Med Imaging* **2016**, 3 (4), 043504.

22. Taguchi, K.; Iwanczyk, J. S., Vision 20/20: Single photon counting x-ray detectors in medical imaging. *Med Phys* **2013**, 40 (10), 100901.

23. Symons, R.; Cork, T. E.; Lakshmanan, M. N.; Evers, R.; Davies-Venn, C.; Rice, K. A.; Thomas, M. L.; Liu, C. Y.; Kappler, S.; Ulzheimer, S.; Sandfort, V.; Bluemke, D. A.; Pourmorteza, A., Dual-contrast agent photon-counting computed tomography of the heart: initial experience. *Int J Cardiovasc Imaging* **2017**, 33 (8), 1253-1261.

24. Symons, R.; Krauss, B.; Sahbaee, P.; Cork, T. E.; Lakshmanan, M. N.; Bluemke, D. A.; Pourmorteza, A., Photon-counting CT for simultaneous imaging of multiple contrast agents in the abdomen: An *in vivo* study. *Med Phys* **2017**, 44 (10), 5120-5127.

25. Gutjahr, R.; Halaweish, A. F.; Yu, Z.; Leng, S.; Yu, L.; Li, Z.; Jorgensen, S. M.; Ritman, E. L.; Kappler, S.; McCollough, C. H., Human imaging with photon counting-based computed tomography at clinical dose levels: contrast-to-noise ratio and cadaver studies. *Invest Radiol* **2016**, 51 (7), 421-429.

26. Pourmorteza, A.; Symons, R.; Reich, D. S.; Bagheri, M.; Cork, T. E.; Kappler, S.; Ulzheimer, S.; Bluemke, D. A., Photon-counting CT of the brain: *in vivo* human results and image-quality assessment. *AJNR Am J Neuroradiol* **2017**, 38 (12), 2257-2263.

27. Pourmorteza, A.; Symons, R.; Sandfort, V.; Mallek, M.; Fuld, M. K.; Henderson, G.; Jones, E. C.; Malayeri, A. A.; Folio, L. R.; Bluemke, D. A., Abdominal imaging with contrast-enhanced photon-counting CT: first human experience. *Radiology* **2016**, 279 (1), 239-245.

28. Symons, R.; Reich, D. S.; Bagheri, M.; Cork, T. E.; Krauss, B.; Ulzheimer, S.; Kappler, S.; Bluemke, D. A.; Pourmorteza, A., Photon-counting computed tomography for

vascular imaging of the head and neck: first *in vivo* human results. *Invest Radiol* **2018**, *53* (3), 135-142.

29. Yu, S. B.; Watson, A. D., Metal-based X-ray contrast media. *Chem Rev* **1999**, *99* (9), 2353-2378.

30. Solomon, R.; Dumouchel, W., Contrast media and nephropathy: findings from systematic analysis and Food and Drug Administration reports of adverse effects. *Invest Radiol* **2006**, *41* (8), 651-660.

31. Tepel, M.; Aspelin, P.; Lameire, N., Contrast-induced nephropathy: a clinical and evidence-based approach. *Circulation* **2006**, *113* (14), 1799-1806.

32. Ritz, E.; Orth, S. R., Nephropathy in patients with type 2 diabetes mellitus. *N Engl J Med* **1999**, *341* (15), 1127-1133.

33. Chakravarty, S.; Unold, J.; Shuboni-Mulligan, D. D.; Blanco-Fernandez, B.; Shapiro, E. M., Surface engineering of bismuth nanocrystals to counter dissolution. *Nanoscale* **2016**, *8* (27), 13217-13222.

34. Cheheltani, R.; Ezzibdeh, R. M.; Chhour, P.; Pulaparathi, K.; Kim, J.; Jurcova, M.; Hsu, J. C.; Blundell, C.; Litt, H. I.; Ferrari, V. A.; Allcock, H. R.; Sehgal, C. M.; Cormode, D. P., Tunable, biodegradable gold nanoparticles as contrast agents for computed tomography and photoacoustic imaging. *Biomaterials* **2016**, *102*, 87-97.

35. Abadeer, N. S.; Fülöp, G.; Chen, S.; Käll, M.; Murphy, C. J., Interactions of bacterial lipopolysaccharides with gold nanorod surfaces investigated by refractometric sensing. *ACS Appl Mater Interfaces* **2015**, *7* (44), 24915-24925.

36. Khan, S. A.; Kanchanapally, R.; Fan, Z.; Beqa, L.; Singh, A. K.; Senapati, D.; Ray, P. C., A gold nanocage–CNT hybrid for targeted imaging and photothermal destruction of cancer cells. *Chem Commun* **2012**, *48* (53), 6711-6713.

37. Li, M.; Li, L.; Zhan, C.; Kohane, D. S., Core-shell nanostars for multimodal therapy and imaging. *Theranostics* **2016**, *6* (13), 2306-2313.
38. Kim, W.; Kim, N.; Park, J. W.; Kim, Z. H., Nanostar probes for tip-enhanced spectroscopy. *Nanoscale* **2016**, *8* (2), 987-994.
39. Liu, X.-L.; Liang, S.; Nan, F.; Yang, Z.-J.; Yu, X.-F.; Zhou, L.; Hao, Z.-H.; Wang, Q.-Q., Solution-dispersible Au nanocube dimers with greatly enhanced two-photon luminescence and SERS. *Nanoscale* **2013**, *5* (12), 5368-5374.
40. Jia, F.; Liu, X.; Li, L.; Mallapragada, S.; Narasimhan, B.; Wang, Q., Multifunctional nanoparticles for targeted delivery of immune activating and cancer therapeutic agents. *J Control Release* **2013**, *172* (3), 1020-1034.
41. Lee, D. E.; Koo, H.; Sun, I. C.; Ryu, J. H.; Kim, K.; Kwon, I. C., Multifunctional nanoparticles for multimodal imaging and theragnosis. *Chem Soc Rev* **2012**, *41* (7), 2656-2672.
42. Xu, C.; Mu, L.; Roes, I.; Miranda-Nieves, D.; Nahrendorf, M.; Ankrum, J. A.; Zhao, W.; Karp, J. M., Nanoparticle-based monitoring of cell therapy. *Nanotechnology* **2011**, *22* (49), 494001-494001.
43. Cormode, D. P.; Skajaa, T.; van Schooneveld, M. M.; Koole, R.; Jarzyna, P.; Lobatto, M. E.; Calcagno, C.; Barazza, A.; Gordon, R. E.; Zanzonico, P.; Fisher, E. A.; Fayad, Z. A.; Mulder, W. J. M., Nanocrystal core high-density lipoproteins: a multimodality contrast agent platform. *Nano Lett* **2008**, *8* (11), 3715-3723.
44. Naha, P. C.; Lau, K. C.; Hsu, J. C.; Hajfathalian, M.; Mian, S.; Chhour, P.; Uppuluri, L.; McDonald, E. S.; Maidment, A. D.; Cormode, D. P., Gold silver alloy nanoparticles (GSAN): an imaging probe for breast cancer screening with dual-energy mammography or computed tomography. *Nanoscale* **2016**, *8* (28), 13740-13754.

45. Mieszawska, A. J.; Mulder, W. J. M.; Fayad, Z. A.; Cormode, D. P., Multifunctional gold nanoparticles for diagnosis and therapy of disease. *Mol Pharm* **2013**, *10* (3), 831-847.
46. Thakor, A. S.; Jokerst, J.; Zavaleta, C.; Massoud, T. F.; Gambhir, S. S., Gold nanoparticles: a revival in precious metal administration to patients. *Nano Lett* **2011**, *11* (10), 4029-4036.
47. Ashton, J. R.; West, J. L.; Badea, C. T., *In vivo* small animal micro-CT using nanoparticle contrast agents. *Front Pharmacol* **2015**, *6*, 256.
48. Naha, P. C.; Zaki, A. A.; Hecht, E.; Chorny, M.; Chhour, P.; Blankemeyer, E.; Yates, D. M.; Witschey, W. R.; Litt, H. I.; Tsourkas, A.; Cormode, D. P., Dextran coated bismuth-iron oxide nanohybrid contrast agents for computed tomography and magnetic resonance imaging. *J Mater Chem B* **2014**, *2* (46), 8239-8248.
49. Eck, W.; Nicholson, A. I.; Zentgraf, H.; Semmler, W.; Bartling, S., Anti-CD4-targeted gold nanoparticles induce specific contrast enhancement of peripheral lymph nodes in X-ray computed tomography of live mice. *Nano Lett* **2010**, *10* (7), 2318-2322.
50. Kwon, H. J.; Cha, M.-Y.; Kim, D.; Kim, D. K.; Soh, M.; Shin, K.; Hyeon, T.; Mook-Jung, I., Mitochondria-targeting ceria nanoparticles as antioxidants for alzheimer's disease. *ACS Nano* **2016**, *10* (2), 2860-2870.
51. von Maltzahn, G.; Park, J. H.; Agrawal, A.; Bandaru, N. K.; Das, S. K.; Sailor, M. J.; Bhatia, S. N., Computationally guided photothermal tumor therapy using long-circulating gold nanorod antennas. *Cancer Res* **2009**, *69* (9), 3892-3900.
52. Kim, J.; Bar-Ness, D.; Si-Mohamed, S.; Coulon, P.; Blevis, I.; Douek, P.; Cormode, D. P., Assessment of candidate elements for development of spectral photon-counting CT specific contrast agents. *Sci Rep* **2018**, *8* (1), 12119.

53. Pan, D.; Roessler, E.; Schlomka, J. P.; Caruthers, S. D.; Senpan, A.; Scott, M. J.; Allen, J. S.; Zhang, H.; Hu, G.; Gaffney, P. J.; Choi, E. T.; Rasche, V.; Wickline, S. A.; Proksa, R.; Lanza, G. M., Computed tomography in color: NanoK-enhanced spectral CT molecular imaging. *Angew Chem Int Ed Engl* **2010**, *49* (50), 9635-9639.
54. Pan, D.; Schirra, C. O.; Senpan, A.; Schmieder, A. H.; Stacy, A. J.; Roessler, E.; Thran, A.; Wickline, S. A.; Proksa, R.; Lanza, G. M., An early investigation of ytterbium nanocolloids for selective and quantitative "multicolor" spectral CT imaging. *ACS Nano* **2012**, *6* (4), 3364-3370.
55. Si-Mohamed, S.; Thivolet, A.; Bonnot, P. E.; Bar-Ness, D.; Képénékian, V.; Cormode, D. P.; Douek, P.; Rousset, P., Improved peritoneal cavity and abdominal organ imaging using a biphasic contrast agent protocol and spectral photon counting computed tomography K-edge imaging. *Invest Radiol* **2018**, *53* (10), 629-639.
56. de Vries, A.; Roessler, E.; Kneepkens, E.; Thran, A.; Brendel, B.; Martens, G.; Proksa, R.; Nicolay, K.; Grull, H., Quantitative spectral K-edge imaging in preclinical photon-counting X-ray computed tomography. *Invest Radiol* **2015**, *50* (4), 297-304.
57. McGinnity, T. L.; Dominguez, O.; Curtis, T. E.; Nallathamby, P. D.; Hoffman, A. J.; Roeder, R. K., Hafnia (HfO₂) nanoparticles as an X-ray contrast agent and mid-infrared biosensor. *Nanoscale* **2016**, *8* (28), 13627-13637.
58. Schirra, C. O.; Senpan, A.; Roessler, E.; Thran, A.; Stacy, A. J.; Wu, L.; Proksa, R.; Pan, D., Second generation gold nanobeacons for robust K-edge imaging with multi-energy CT. *J Mater Chem* **2012**, *22* (43), 23071-23077.
59. Pelc, N. J., Recent and future directions in CT imaging. *Annu Rev Biomed Eng* **2014**, *42* (2), 260-268.

60. Cuccione, E.; Chhour, P.; Si-Mohamed, S.; Dumot, C.; Kim, J.; Hubert, V.; Da Silva, C. C.; Vandamme, M.; Chereul, E.; Balegamire, J.; Chevalier, Y.; Berthezène, Y.; Bousset, L.; Douek, P.; Cormode, D. P.; Wiart, M., Multicolor spectral photon counting CT monitors and quantifies therapeutic cells and their encapsulating scaffold in a model of brain damage. *Nanotheranostics* **2020**, *4* (3), 129-141.
61. Liu, T.; Xiao, B.; Xiang, F.; Tan, J.; Chen, Z.; Zhang, X.; Wu, C.; Mao, Z.; Luo, G.; Chen, X.; Deng, J., Ultrasmall copper-based nanoparticles for reactive oxygen species scavenging and alleviation of inflammation related diseases. *Nat Commun* **2020**, *11* (1), 2788.
62. Singh, N.; Savanur, M. A.; Srivastava, S.; D'Silva, P.; Mugesh, G., A manganese oxide nanozyme prevents the oxidative damage of biomolecules without affecting the endogenous antioxidant system. *Nanoscale* **2019**, *11* (9), 3855-3863.

CHAPTER 2: ASSESSMENT OF CANDIDATE ELEMENTS FOR DEVELOPMENT OF ULTRASMALL NANOPARTICLE-BASED PHOTON-COUNTING CT CONTRAST AGENTS

2.1 Abstract

Spectral photon-counting computed tomography (SPCCT) is a rapidly emerging imaging modality that provides energy-dependent information of individual x-ray photons, allowing material decomposition and simultaneous quantification of multiple contrast generating materials. Development of SPCCT-specific contrast agents is needed to overcome the issues with currently used iodinated contrast agents, such as difficulty in differentiation from calcified structures, and to yield SPCCT's full promise. In this study, the contrast generation of several candidate elements is investigated using a prototype SPCCT scanner based on a modified clinical CT system and suitable elements for novel contrast agent development for SPCCT imaging are identified. Furthermore, nanoparticles were synthesized from tantalum as a proof of concept spectral photon-counting CT agent. *In vitro* cytotoxicity and contrast generation of tantalum oxide nanoparticles are tested to provide insight into the feasibility of nanoparticle-based contrast agent development from these elements. We found that gadolinium, ytterbium and tantalum generate high contrast in spectral photon-counting CT imaging and may be the most suitable elements for contrast agent development for this modality. Our proof-of-concept study results with tantalum oxide nanoparticles underscore this conclusion due to their detectability with spectral photon-counting CT and their biocompatibility.

2.2 Introduction

X-ray computed tomography (CT) is one of the most widely used imaging modalities in medicine due to its broad availability, low cost, high spatial resolution and fast image acquisition time.¹ Although it is already well-established, CT is undergoing a period of rapid innovation. Under extensive investigation for clinical feasibility is spectral photon-counting CT (SPCCT), an emerging form of CT that uses a standard polychromatic x-ray source and photon-counting detectors (PCDs).²⁻⁷ Prototypes of SPCCT scanners that have been modified from clinical CT systems are currently available for both pre-clinical and clinical research.^{2,4,5} PCDs are capable of measuring the energy levels of individual x-ray photons unlike the energy integrating detectors (EIDs) used in conventional CT scanners. EIDs discard the energy information of incident x-ray photons since they sum all the energy deposited in each pixel, resulting in photons with higher energy being weighted more heavily than photons with lower energy.^{8,9} PCDs achieve the energy-resolving measurement of x-ray photons by converting x-rays into currents, inferring their energies *via* pulse height analysis, and separating them into several data bins with adjustable energy thresholds. Since different materials have differing x-ray attenuation profiles, characterizing the energy distribution of the transmitted beam allows specific detection of substances such as exogenous contrast agents.^{4,10}

SPCCT systems have multiple benefits, such as improved contrast-to-noise ratios (CNR), lower noise, higher spatial resolution and fewer image artifacts (e.g., blooming and beam hardening).^{11,12} These benefits can lead to acquisition of higher quality images at lower radiation doses than with conventional CT systems. Preclinical and clinical studies so far have demonstrated the advantages of SPCCT imaging in several animal models, as well as in human subjects.^{2,3,5,13,14} Besides the image quality and the patient dose

advantages of SPCCT, these systems can specifically distinguish multiple contrast generating materials in a single scan *via* material decomposition by assigning an appropriate number of energy bins and their thresholds.¹⁵⁻²⁰ This feature allows differentiation of exogenous contrast agents from soft tissues and calcified structures (e.g. bones and calcified atherosclerotic plaques), which can be especially beneficial in coronary CT angiography. Simultaneous material decomposition also eliminates the need for comparison of pre- and post-administration images, further reducing patient radiation exposure. As demonstrated by Si-Mohamed *et al.*,⁴ SPCCT systems are also capable of providing absolute quantification of exogenous contrast agents *in vivo* to allow biodistribution assessment without the need for *ex vivo* analysis.

To date, iodine-based small molecules are the most commonly used intravenous contrast agents for CT imaging. While contrast generation of iodinated contrast agents in SPCCT systems is as effective as contrast generation in conventional and dual energy CT systems, they do not take full advantage of the capability of K-edge imaging in SPCCT. This is because there are too few photons in CT X-ray beams below iodine's low K-edge energy (33.2 keV) for accurate material decomposition to be completed. Iodine-based contrast agents are also known to cause allergic reactions, and there are concerns over kidney function reduction in patients with renal insufficiency through contrast-induced nephropathy (CIN) or contrast-induced acute kidney injury.^{21,22} CIN does not develop into chronic renal failure in most cases; however, it may still result in complete renal failure in the patients with poor renal function, increasing the risk of morbidity and mortality.²³ Thus, developing novel contrast agents specifically designed for SPCCT systems can be valuable to allow full utilization of its capabilities and broaden its applications. Substantial work has been done over the past decade using nanoparticles made of heavy metal

elements, such as gold,²⁴⁻²⁸ bismuth,^{29,30} tantalum^{31,32} and others³³⁻³⁷, as contrast agents for EID-based CT. These nanoparticle-based CT contrast agents can be synthesized to have similar or different pharmacokinetics and biodistributions to iodine. They have been studied for various applications, such as vascular imaging,^{25,38} theranostics in drug delivery³⁹ and radiotherapy,⁴⁰ as well as cell tracking.^{41,42} For effective imaging, contrast agents for SPCCT imaging need to be based on elements that have K-edge energies within a region where there are a reasonable number of photons both above and below their K-edge energy (roughly 40–100 keV in a 120 kVp beam) (Figure 2.1). There have been a number of reports that focus on the use of contrast agents made of heavy metal elements (e.g., gold, bismuth or gadolinium) for SPCCT imaging.^{10,17,18,43} However, there is a lack of systematic studies that examine contrast generation from different elements in SPCCT imaging.

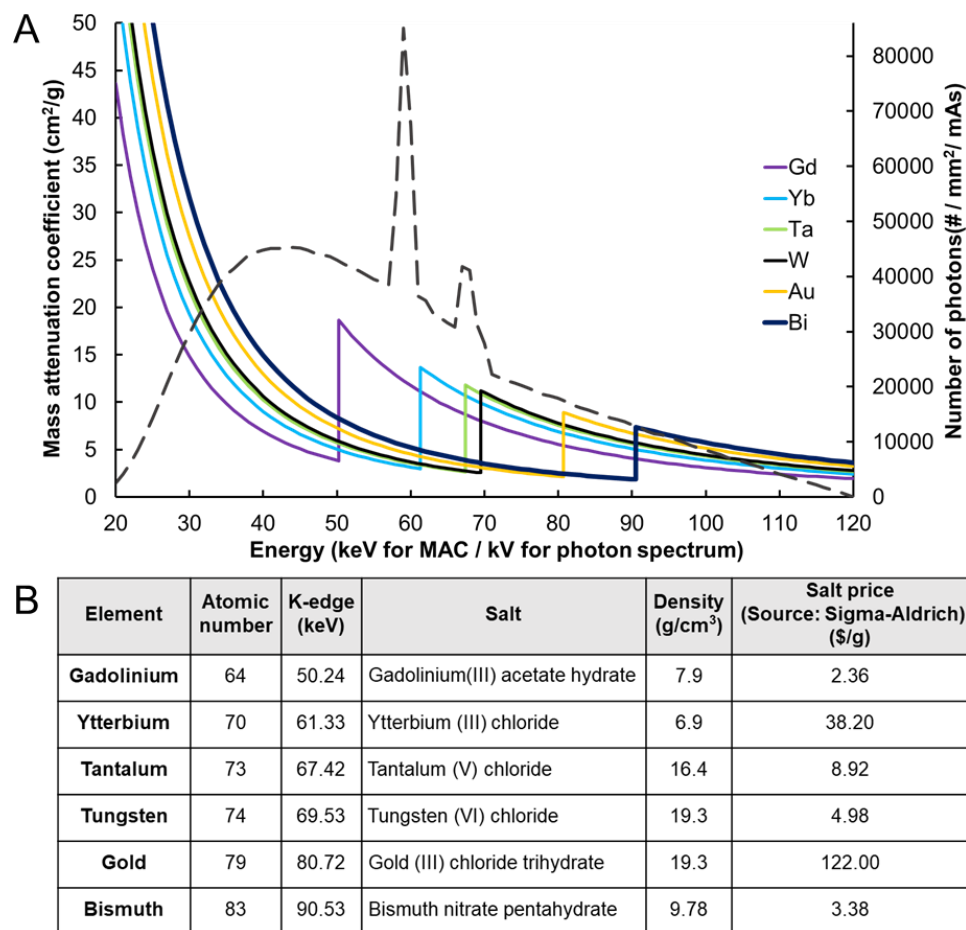


Figure 2.1 Candidate heavy metal elements for SPCCT contrast agent development.

(A) Mass attenuation coefficients of various heavy metal elements and X-ray photon intensities at a tube voltage of 120 kV. The X-ray photon intensity spectrum (dotted line) was generated by using Spektr 3.0 (x-ray spectrum modeling software). (B) Characteristics of the six heavy elements used in this study. The salt prices of these elements were obtained from Sigma-Aldrich.

We therefore decided to survey various heavy metal elements for candidates for novel SPCCT contrast agents. From elements whose K-edge fell into the range of 40–100 keV, we first eliminated those that are highly toxic or radioactive, such as thulium and

radium.¹² Then we considered economically *viable* elements that have been previously studied as experimental contrast agents or for nanoparticle synthesis. Taking these criteria into consideration, we selected gadolinium, ytterbium, tantalum, tungsten, gold and bismuth as the most suitable elements for contrast agent development (Figure 2.1B). Gold has been most extensively studied as a contrast generating material for SPCCT,^{4,17,44} therefore we included it in this panel despite its relatively high material cost. We herein report the contrast production of these elements using a prototype SPCCT system with a high-count rate that can cope with photon fluxes needed for medical imaging.

Nanoparticle-based contrast agents from a lead element can allow successful material differentiation from calcified structures to broaden the applications of SPCCT imaging.⁴⁵ These nanoparticles can also be synthesized to have favorable pharmacokinetics and biodistribution and to act as a platform for targeted imaging, further expanding the potential role of SPCCT imaging. Therefore, we formed nanoparticles with a lead element and performed a series of proof-of-concept experiments to provide insight into the feasibility of SPCCT contrast agent development from these candidate elements. By identifying elements that produce high CNR in a prototype SPCCT scanner, this study provides guidance for the future development of novel SPCCT-specific contrast agents.

2.3 Materials and methods

2.3.1 Materials

Gadolinium(III) acetate hydrate (99.9% trace metals basis), ytterbium(III) chloride hexahydrate (99.9%), tantalum(V) chloride (99.8%), tungsten(VI) chloride (99.9%), gold(III) chloride trihydrate (99.9%), bismuth(III) nitrate pentahydrate (98.0%), tantalum(V) ethoxide (99.98%), cyclohexane (99%), IGEPAL CO-520, ammonium hydroxide solution

(28.0–30.0% NH₃ basis) and calcium phosphate (96.0%) were purchased from Sigma-Aldrich (St. Louis, MO). 2-(carbomethoxy)ethyltrimethoxysilane and 3-(trimethoxysilyl)propyl-N,N,N-trimethylammonium chloride were obtained from Gelest, Inc (Morrisville, PA). Iomeron 400 mg/ml was purchased from Bracco (Milan, Italy). The cell lines used for *in vitro* experiments (i.e., HepG2, Renca, SVEC4-10EHR1) were provided by ATCC (Manassas, VA). LIVE/DEAD assay kits were purchased from Life Technologies Invitrogen (Grand Island, NY).

2.3.2 CT and SPCCT systems

A prototype SPCCT scanner (Philips Healthcare, Haifa, Israel) modified from a clinical CT system, located at the University of Lyon, was used to acquire phantom images. As previously described,⁴ the scanner has field-of-view (FOV) of 168 mm in-plane, z-coverage of 2 mm, gantry rotation time of 0.75 seconds (2400 projection per rotation), focal spot of 0.7 × 0.7 mm, isotropic pixel size of 250 μm, and in-plane resolutions of 11.4 lp/cm (line pair per cm) at 50% modulation transfer function (MTF) and 22.4 lp/cm at 10% MTF.¹⁶ The scanner is equipped with a PCD made of high band gap semiconductor cadmium zinc telluride with a pixel pitch of 500 × 500 μm (Figure 2.2).⁴⁶

Parameter	Specification
Platform	Philips iCT
Field of view (FOV)	168 mm in-plane
Z-coverage in iso-center	2 mm
Gantry rotation	0.75 second
Projections per rotation	2400
Focal spot	0.7 mm x 0.7 mm
Pixel pitch	500 μm x 500 μm



Figure 2.2 Specifications and photograph of the prototype SPCCT scanner used in this study.

The energy-resolving detector has 5 configurable energy thresholds. The phantoms were scanned using 5 energy bins whose thresholds were set specifically for each candidate element in this study to allow K-edge imaging (e.g. 30, 51, 78, 83 and 98 keV for gold). For each element, two energy bin thresholds were set just below and above its K-edge for optimal signal-to-noise ratio and higher accuracy in quantitative information of the element, as described by Roessl *et al.*^{47,48} Five axial scans were performed using a conventional x-ray tube with a peak voltage of 120 kVp and current of 100 mA. A Philips Ingenuity CT (Philips Healthcare, Cleveland, US), a conventional clinical CT located at the University of Lyon, was also used to acquire phantom images for CT attenuation analysis. The images were acquired using FOV of 500 mm, 160 mm reconstruction diameter, slice thickness of 1 mm, pixel spacing of 0.3125 mm and gantry rotation time of 0.4 seconds in full 360° scans. The same scan parameters (i.e. tube voltage of 120 kVp and current of 100 mA) were used to acquire the phantom images with both scanners, which are of the same geometry.

2.3.3 SPCCT phantom imaging and image analysis

A polyoxymethylene cylindrical phantom body that is 13 cm in diameter and with twelve holes for tube insertions was used as the phantom (Figure 2.3). A range of concentrations of each element (i.e. 0, 0.5, 1, 2, 4, 6, 8, and 12 mg/ml) in either ethylene glycol for bismuth nitrate or in deionized water for all other precursor salts (i.e., gadolinium acetate, ytterbium chloride, tungsten chloride and gold chloride) were placed in the outer eight holes. Ethylene glycol was used to dissolve bismuth nitrate since it is poorly soluble in water.⁴⁹ Two *vials* containing either 2 mg/ml or 5 mg/ml of iodinated media (Iomeron), one *vial* containing a bone simulant (calcium phosphate solution) and one empty *vial* (for

air measurement) were placed in the inner four holes. All solutions were prepared in 1.5 ml polypropylene centrifuge tubes (Eppendorf, Hauppauge, NY).

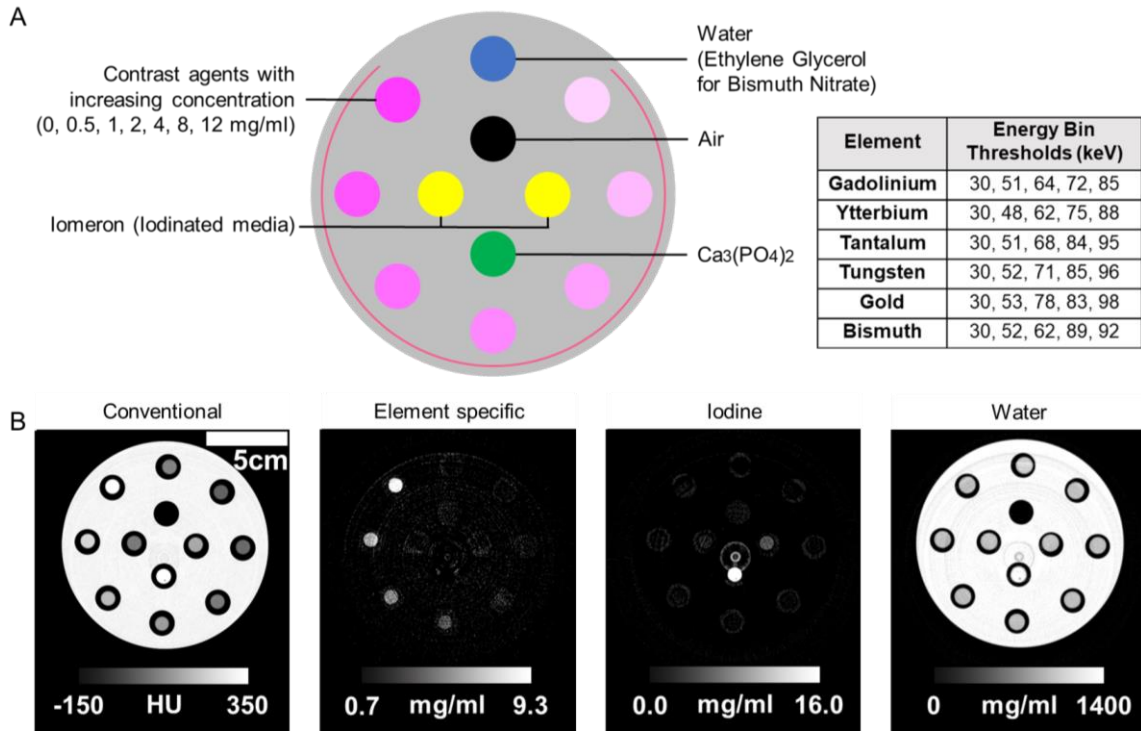


Figure 2.3 SPCCT phantom design and images.

(A) Schematic depiction of sample tube locations on the phantom and the energy bin thresholds used for each element. (B) Four images generated from SPCCT imaging. Images of gadolinium are shown as an example.

For image analysis, we assessed attenuation rate (AR) and CNR rate (CNRR). AR was defined as attenuation divided by the concentration of the elements in mg/ml. CNRR was defined as CNR divided by the concentration of the element. CNR was calculated by subtracting the signal in water from the signal from a sample, then dividing the resulting number by the noise. Noise from the images for each element was determined by measuring the standard deviation in water tube using OsiriX v.3.7.1 64-bit software

(Pixmeo SARL, Bernex, Switzerland). Circular regions of interest (diameter 6.5 mm, area 33.18 mm²) were drawn in the middle of each sample tube, and the output from each ROI was recorded. Conventional CT equivalent images were used to calculate AR and element specific K-edge images were used for CNRR. To measure AR, the attenuation values from conventional CT equivalent images (as attenuation on y axis) were graphed against mass concentration of the elements (mg/ml on x axis), and the slope of the linear line of best fit was calculated.²⁶ Similarly, the CNR values from element-specific K-edge images were compared against element concentrations to determine the CNRR. Every ROI measurement was performed on slice thickness of 2 mm.

2.3.4 Material decomposition and image reconstruction method

Each slice was reconstructed into conventional CT equivalent images, element specific images, water images, and iodine images (see Figure 2.3B for example). Using the energy information of the transmitted photons in all five energy bins, conventional CT-equivalent images were synthesized, in which the data is displayed in Hounsfield units. Specifically, these images are generated by best fit of the measured count rates in all five energy bins to calibration data, based on the phantom with various path lengths. A maximum-likelihood material decomposition based on literature data on the CT attenuations of the target materials was applied to derive three material sinograms – element-specific, iodine and water – from the distribution of photon counts across the five energy bins.

2.3.5 Tantalum oxide nanoparticle synthesis

Sub 5-nm tantalum oxide nanoparticles (TaONP) were synthesized by modifying the microemulsion method described by Oh *et al.*³¹ Microemulsions were prepared by adding 250 μ L of 75 mM NaOH solution to 20 mL of cyclohexane containing 2.7 g of IGEPAL CO-520. 50 μ L of 0.3 mM tantalum(V) ethoxide solution (78.3 mg), as provided by the supplier, was added to this emulsion. The resulting mixture was incubated for 15 min while stirring. To make TaONP water-soluble, 70 μ L of 2-(carbomethoxy)ethyltrimethoxysilane and 200 μ L of 3-(trimethoxysilyl)propyl-N,N,N-trimethylammonium chloride in 1 ml of ethanol were added to the nanoparticle solution. After 24 hr of stirring at room temperature, a white sediment had formed at the bottom of the flask. The colorless supernatant was removed *via* careful aspiration, and the white sediment was dissolved in 5 mL of 5 M ammonium hydroxide solution and allowed to stir for 30 min. At which point, 25 ml of ultrapure water was added, and the resulting solution was centrifuged at 2500 g for 15 min. This centrifugation step resulted in separation of the aqueous phase from remaining cyclohexane and aggregates, which formed a pellet. The clear aqueous solution was collected by careful pipetting, leaving behind the aggregates and cyclohexane. The resulting nanoparticle solution was further purified and concentrated by centrifugation and washing in deionized water three times using 10 kDa MWCO centrifugation tubes (GE Healthcare Life Sciences, Marlborough, MA). Each batch of solution was then redispersed in 4 ml of PBS, centrifuged at 5000 g for 10 minutes in 1.5 mL centrifuge *vials*, and was filtered through 0.22 μ m syringe filter. The final nanoparticle solution was stable in both deionized water and PBS.

2.3.6 Nanoparticle characterization

Transmission electron microscopy (TEM) was used to evaluate the morphology and core size of TaONP. The microscope used was a JEOL 1010 (JEOL USA Inc., Peabody, MA). ImageJ was used to determine the average diameter of nanoparticle cores from the electron micrographs. The hydrodynamic diameter and ζ -potential of TaONP were determined using a Nano ZS-90 Zetasizer (Malvern Instruments, Worcestershire, UK). The concentration of TaONP was determined *via* inductively coupled plasma atomic emission spectroscopy (ICP-OES). To prepare ICP samples, 5–10 μ L of nanoparticle solution was dissolved in 1 mL of aqua regia (one part nitric acid to three parts hydrochloric acid) for 3 hr before adding ultrapure water to make the final volume to 5 mL. The resulting solutions were analyzed with a Spectro-Genesis ICP (Spectro Analytical Instruments GmbH, Kleve, Germany) for tantalum concentration.

2.3.7 *In vitro* cytotoxicity experiment

The LIVE/DEAD assay (Life Technologies, Frederick, MD) was used to study the effect of TaONP on the *viability* of Renca (epithelial kidney cells), SVEC4-10EHR1 (endothelial cells), and HepG2 (hepatocytes). The cells were cultured in 20 mm glass bottom dishes at a seeding density of 1.0×10^5 per dish for 24 hr at 37 °C and 5% CO₂. The cell growth medium recommended by ATCC for each cell line was used. Next, the media was removed and replaced with fresh media containing various concentrations (0.025 mg/ml to 1 mg Ta/ml) of TaONP. After 8 hr incubation with TaONP, cells were washed twice with DPBS and treated with 400 μ L of LIVE-DEAD cocktail (2 μ L of ethidium homodimer-1, 1 μ L calcein AM, and 3 μ L of 3.2 mM Hoechst 33342 in 2 mL DPBS) for 20 min. The cells were then imaged with a Nikon Eclipse Ti-U fluorescence microscope to

visualize cell nuclei, living cells and dead cells. Images from four different fields of view in each dish were acquired. The images were analyzed by a custom-made MATLAB code to count the number of cells. The cell *viability* percent was calculated by dividing the live cell count by total number of cells. These experiments were repeated three times for each cell line.

2.3.8 Statistical analysis

The LINEST function of Excel was used to determine the slope (m_x) and standard error of fit (e_x) of both AR and CNRR. Following the calculation of m_x and e_x , the following equation was used to calculate t-values:

$$t_{1-2} = (m_1 - m_2) / \sqrt{(e_1^2 + e_2^2)}$$

The t-values were then compared with the 5% reference t-value at degrees of freedom of 12 (7 concentration points from 1st element (n_1) + 7 concentration points from 2nd element (n_2) - 2), which is 2.18. Comparisons were made between every possible pair of the six elements used in this study. Linear regression and Bland-Altman analyses were performed to assess correlation between AR obtained from the conventional CT and the SPCCT system. One-way analysis of variance (ANOVA) and Tukey-Kramer HSD (honestly significant difference) posthoc test was used for *in vitro* cytotoxicity experiment.

2.4 Results

2.4.1 Phantom imaging

Conventional CT equivalent, element specific, iodine, and water images were successfully generated from scanning the phantom (Figure 2.3B). An increase in

attenuation can be observed as element concentration increases in the conventional CT equivalent image. Element-specific images demonstrated that each K-edge element could be successfully differentiated from other materials in the field of view, including calcium phosphate, iodine and the phantom body.

2.4.2 Attenuation rate

There was an excellent linear correlation between the attenuation observed in conventional CT equivalent images and element concentration, as is typically the case.^{4,17,26} The data for gadolinium is displayed in Figure 2.4A as an example. All six elements had an R^2 value very close to unity (Table 2.1). We found that gadolinium had the highest value of AR, followed by tantalum, ytterbium, gold, tungsten and bismuth (Figure 2.4B). We also observed that there was a noticeable decrease in AR value between atomic number 73 (tantalum) and 74 (tungsten). The differences between most of the pairs of elements were statistically significant, except for gadolinium and tantalum, tungsten and bismuth, tungsten and gold, and gold and bismuth (Table 2.2A). It appears that within the section of the periodic table studied and this scanner, high Z-elements whose atomic number is equal to or less than 73 generate about 20% more attenuation compared to elements whose atomic number is higher than 73, on average.

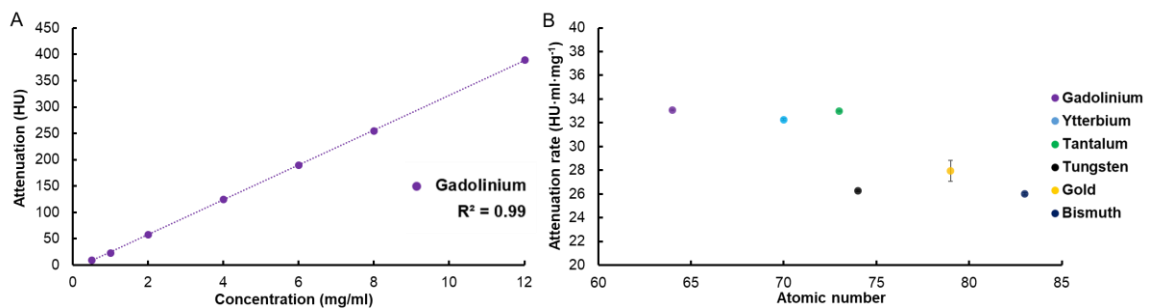


Figure 2.4 Attenuation rates of candidate elements from SPCCT system.

(A) Attenuation of gadolinium at a range of concentrations. (B) Attenuation rates of different elements studied. Error bars represent the standard error of the regression. For data points where the error bars are not visible, this is because the error value is very low and is obscured by the data point.

Element	R ² value of AR
Gadolinium	0.9999
Ytterbium	0.9999
Tantalum	0.9999
Tungsten	0.9999
Gold	0.9806
Bismuth	0.9996

Table 2.1 R² value of AR in all six elements in the phantom study.

A Attenuation rate in SPCCT							B Attenuation rate in conventional CT						
vs.	Gadolinium	Ytterbium	Tantalum	Tungsten	Gold	Bismuth	vs.	Gadolinium	Ytterbium	Tantalum	Tungsten	Gold	Bismuth
Gadolinium		-3.81	-0.55	-37.26	-2.91	-25.94	Gadolinium		13.95	1.63	-0.29	0.88	-9.27
Ytterbium	3.81		3.62	-28.61	-2.45	-21.55	Ytterbium	-13.95		-1.63	-13.96	-0.84	-17.03
Tantalum	0.55	-3.62		-40.72	-2.86	-26.71	Tantalum	-1.63	1.63		-1.67	0.02	-4.32
Tungsten	37.26	28.61	40.72		0.89	-1.35	Tungsten	0.29	13.96	1.67		0.90	-9.07
Gold	2.91	2.45	2.86	-0.89		-1.09	Gold	-0.88	0.84	-0.02	-0.90		-2.35
Bismuth	25.94	21.55	26.71	1.35	1.09		Bismuth	9.27	17.03	4.32	9.07	2.35	

Critical t-value	2.18
------------------	------

Table 2.2 T-values of every possible pair of elements in two sample T-test for AR.

A) conventional CT equivalent images from SPCCT and B) images from conventional CT. The pairs that did not have statistically significant differences in AR are highlighted in gray.

To examine whether this observed trend from a SPCCT system was also present in data acquired from EID-based CT images, the phantom was also imaged with a conventional CT scanner with the same tube current and voltage. As can be seen in Figure 2.5A, the AR values of the elements from conventional CT images were fairly similar to that of the elements from SPCCT images, ranging from 25.2 to 33.0 HU·ml·mg⁻¹ (as opposed to 26.0 to 33.1 HU·ml·mg⁻¹ in CT equivalent images from SPCCT). The differences in AR between the elements were less noticeable in conventional CT images, and the decrease in AR between tantalum and tungsten was less apparent. In fact, there was no statistical differences between gold and four different elements (gadolinium, ytterbium, tantalum, tungsten), tantalum and two elements (gadolinium and ytterbium), and tungsten and two elements (gadolinium and tantalum) (Table 2.2B).

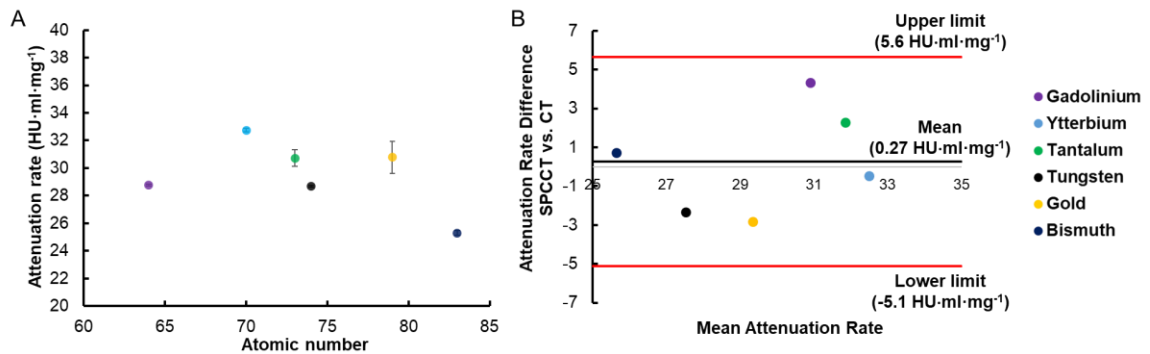


Figure 2.5 Comparison in AR between CT and SPCCT systems.

(A) The attenuation rates of different elements studied in conventional CT. (B) Bland-Altman analysis of attenuation rate from CT and SPCCT systems. The same key for the elements is used in both A and B.

Bland-Altman analysis was also used to demonstrate the agreement of two AR values between SPCCT and CT. As seen in Figure 2.5B, the mean of differences, as

known as bias, was $0.27 \text{ HU}\cdot\text{ml}\cdot\text{mg}^{-1}$ with limits of agreement at $-5.1 \text{ HU}\cdot\text{ml}\cdot\text{mg}^{-1}$ and $5.6 \text{ HU}\cdot\text{ml}\cdot\text{mg}^{-1}$. The differences in AR values for all elements in the study were below the limit of agreement and were distributed in a small range near the bias with the highest difference observed in gadolinium (difference of $4.3 \text{ HU}\cdot\text{ml}\cdot\text{mg}^{-1}$). This shows that AR values derived from SPCCT images are comparable to those from conventional CT images.

2.4.3 Contrast-to-noise ratio rate and noise

As can be seen in Figure 2.6A, the CNR values from element-specific images were linearly correlated with element concentration. Similar to AR, CNRR of all six elements had R^2 values very close to unity (Table 2.3), demonstrating the capability of this SPCCT system to accurately quantify the concentrations of the elements, similar to results found for gold in previous studies.^{4,17}

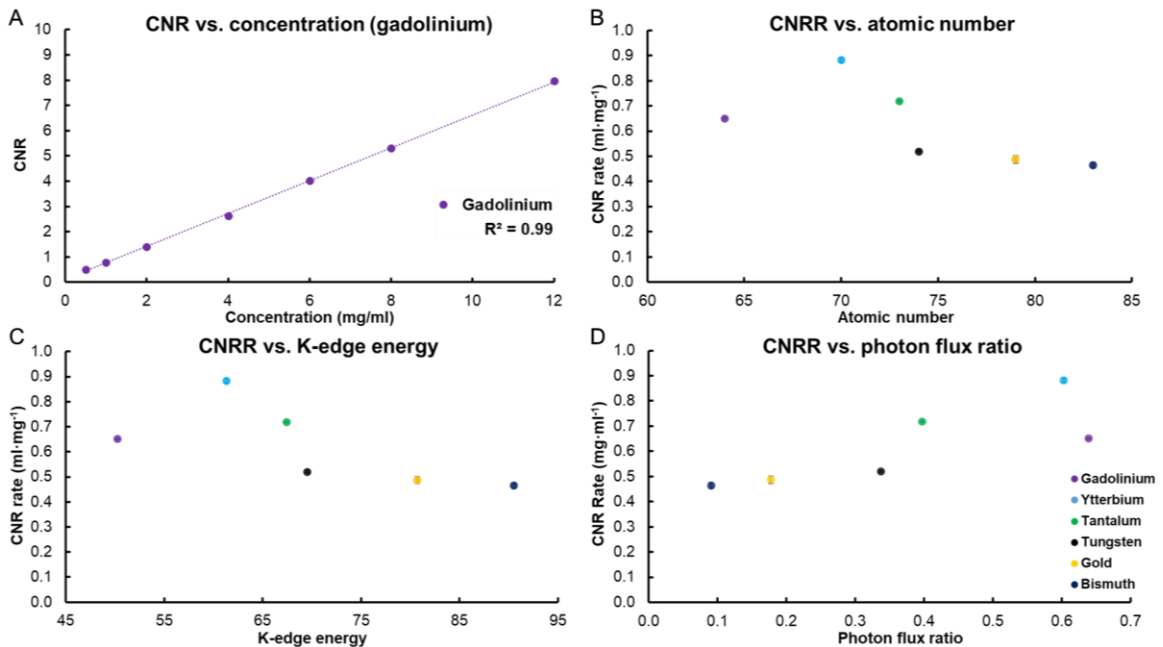


Figure 2.6 CNR rates of candidate elements from SPCCT system.

(A) CNR of gadolinium at a range of concentrations. (B) CNRR of the different elements studied. (C) CNRR of the different elements compared with their K-edge energies. (D) CNRR of the elements compared to the ratio of number of photons above and below their K-edge energies (based on the photon spectrum in the air shown in Figure 2.1A). The same key is used for B-D. CNR and CNRR were calculated from the element specific images.

Element	R ² value of CNRR
Gadolinium	0.9997
Ytterbium	0.9977
Tantalum	0.9996
Tungsten	0.9991
Gold	0.9819
Bismuth	0.9879

Table 2.3 R² value of CNRR in all six elements in the phantom study.

vs.	Gadolinium	Ytterbium	Tantalum	Tungsten	Gold	Bismuth
Gadolinium		11.86	8.21	-14.80	-5.45	-7.88
Ytterbium	-11.86		-8.28	-18.06	-11.29	-14.08
Tantalum	-8.21	8.28		-21.18	-7.66	-10.66
Tungsten	14.80	18.06	21.18		-1.10	-2.33
Gold	5.45	11.29	7.66	1.10		-0.60
Bismuth	7.88	14.08	10.66	2.33	0.60	

Critical t- value	2.18
--------------------------	------

Table 2.4 T-values of every possible pairs of elements in two sample T-test for CNRR in element specific images of SPCCT. The pairs that did not have statistically significant differences in CNRR are highlighted in gray.

CNRR values were the highest for ytterbium, followed by tantalum, gadolinium, tungsten, gold and bismuth (Figure 2.6B). There were no statistically significant differences in CNRR values between gold and bismuth as well as gold and tungsten, but the CNRR values were found to be statistically significantly different between all other possible pairs of elements (Table 2.4). The differences were also substantial, with the CNRR for ytterbium being 62% and 58% higher than those for bismuth and gold, respectively. Similar to AR, CNRR was lower for elements whose atomic number was 74 or above, compared with elements 73 or lower. This created two groups of elements, one that has high CNRR (gadolinium, ytterbium, tantalum) and the other with low CNRR (tungsten, gold, bismuth). In an effort to understand the variation in CNRR, we examined its relationships with other parameters, such as the K-edge energy of the elements and the ratio of number of photons above and below the K-edge energy. As can be seen in Figure 2.6C, the elements whose K-edge energies are at 67.4 keV (tantalum) or below have higher CNRR than the elements whose K-edge energies are at 69.5 keV (tungsten) or above. Since having sufficient numbers of photons both below and above the K-edge energy is considered to be an important factor in ideal reconstruction of element specific images, we also analyzed CNRR in terms of the photon flux ratio above and below the K-edge energies. We observed that higher photon flux ratios closer to one resulted in higher CNRR values (Figure 2.6D). Last, we examined the noise in the element specific images (Figure 2.7). Noise was the main determinant of CNRR in SPCCT imaging. Low noise was

observed for the elements whose atomic numbers are less than or equal to 73, while higher noise was observed in elements whose atomic numbers are higher than 73 (Figure 2.7A). We also observed that noise level generally decreases with increasing photon flux ratio above and below the K-edge energies (Figure 2.7B).

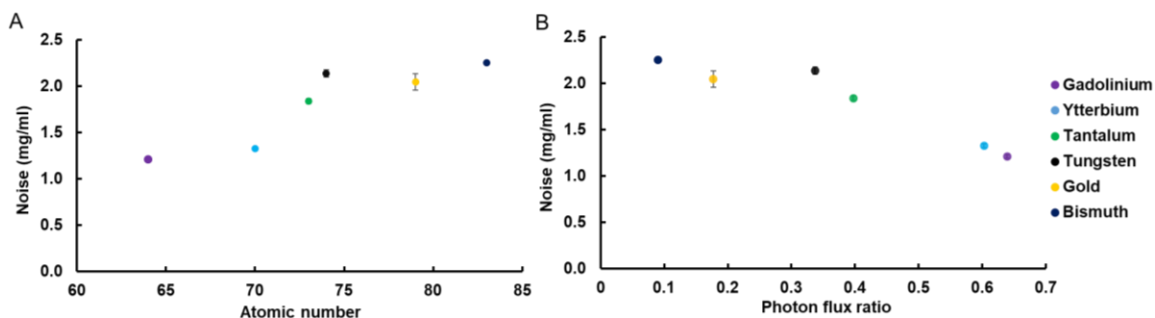


Figure 2.7 Noise level of candidate elements.

(A) Noise levels of the element specific images. (B) Noise level from the element specific images compared to the ratio of numbers of photons above and below the K-edge energy for each element.

2.4.4 Tantalum oxide nanoparticle synthesis and characterization

As demonstrated in the phantom imaging, tantalum had one of the highest AR values along with gadolinium and the second highest CNRR value after that of ytterbium. Moreover, its high elemental density ($d = 16.4 \text{ g/cm}^3$), affordability (approximately 13-fold cheaper than gold and 4-fold cheaper than ytterbium) and suitable K-edge energy (67.4 keV) that can lead to material differentiation from calcified structures in SPCCT make tantalum an appealing element for further development into a SPCCT contrast agent. To test the potential use of tantalum-based contrast agents in SPCCT imaging, water-soluble, sub-5 nm TaONP were synthesized. TaONP were synthesized using a microemulsion

method and were given a zwitterionic small molecule coating to provide solubility and stability in biological media (Figure 2.8A).⁵⁰ The size and surface potential of TaONP were characterized by TEM and DLS (Figure 2.8B). The mean core diameter measured from TEM images was 4.9 nm. The mean hydrodynamic diameter of 12.5 nm was slightly larger than the core diameter as expected, due to the molecules attached to the nanoparticle surface. The surface potential of TaONP was found to be slightly negative (-11.1 ± 2.1 mV).

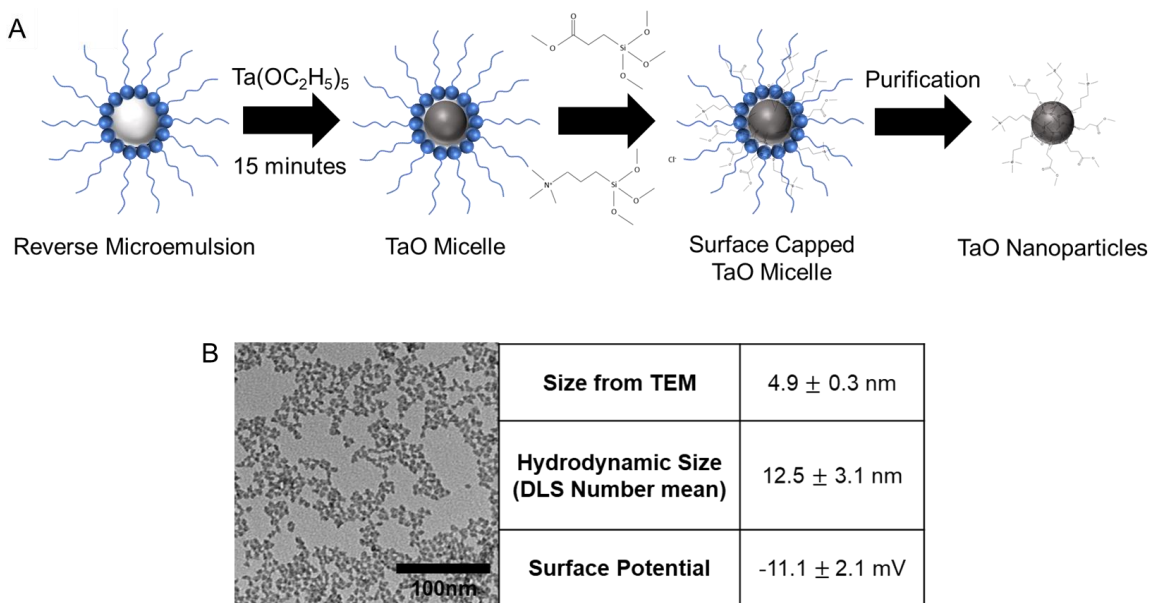


Figure 2.8 Synthesis and physicochemical characteristics of TaONP.

(A) Schematic depiction of the TaONP synthesis process. (B) TEM of TaONP, size and surface potential of TaONP measured from TEM and DLS.

2.4.5 *In vitro* cytocompatibility of tantalum oxide nanoparticles

To study the safety of TaONP, they were incubated with cell types that are expected to have high exposure upon administration, i.e. hepatocytes, endothelial cells

and epithelial kidney cells (Figure 2.9). There was no statistically significant effect on cell viability from TaONP treatment for any cell type or treatment concentration, which indicates the safety and potential use of TaONP for biomedical applications.

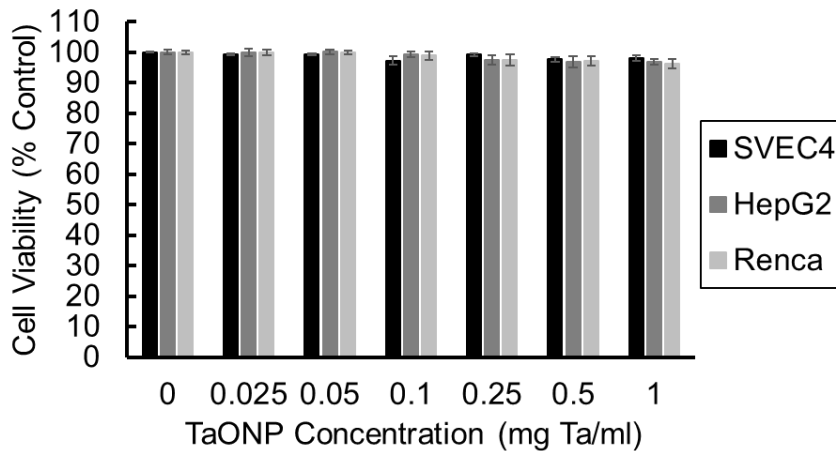


Figure 2.9 Effect of TaONP on cell viability after 8 hr of incubation.

2.4.6 SPCCT phantom imaging of tantalum oxide nanoparticles

To study the capabilities of the SPCCT system in differentiating TaONP from other elements (i.e. iodine) and the detection limit of TaONP, phantom images of TaONP were acquired. As seen in Figure 2.10, the scanner could accurately determine the location of TaONP in the field of view. Iodine and calcium phosphate were clearly distinguished from TaONP. TaONP-specific images indicate that concentration as low as 1 mg/ml of TaONP can be detected in the SPCCT scanner, which is comparable to the detection limit of gold at 1 mg/ml in conventional CT scanner.²⁶

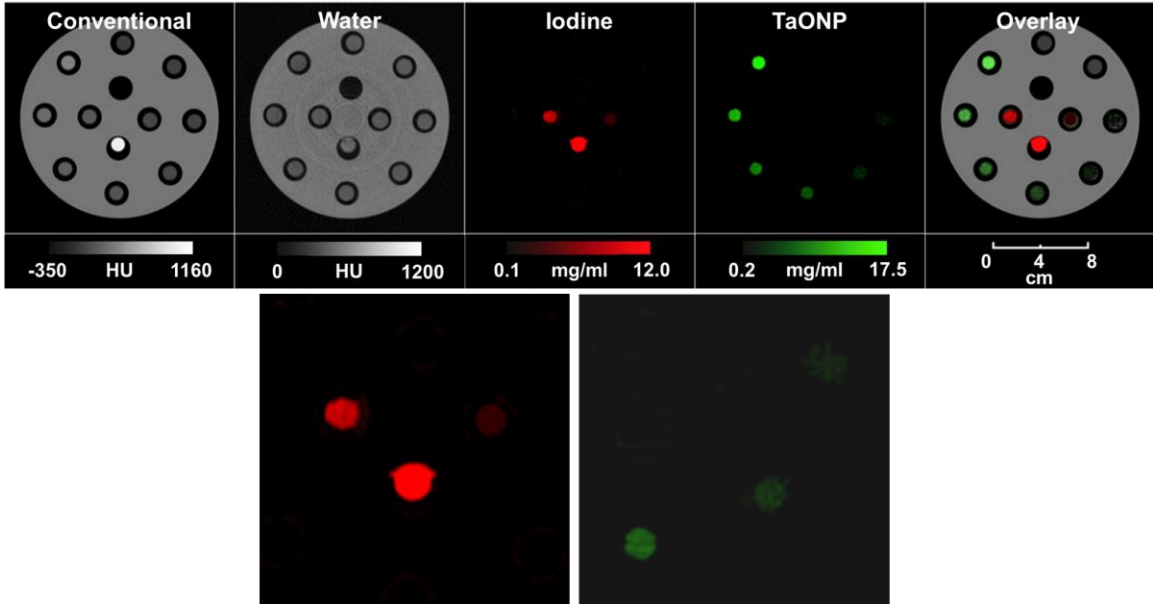


Figure 2.10 SPCCT imaging of TaONP.

SPCCT images of the phantom showing differentiation of TaONP ranging from 0 to 12 mg Ta/ml from an iodine-based contrast agent (2 and 5 mg/ml). Two images on the bottom row are the enlarged iodine and TaONP images centered at tubes with lower element concentrations.

2.5 Discussion

We have demonstrated that gadolinium, ytterbium and tantalum provide higher CT signal generation and better element-specific CNR over tungsten, gold and bismuth in the current prototype SPCCT system used in this study. These results suggest that the elements in the range of atomic numbers between 64 to 73 can be suitable candidates for future development into high-performing contrast agents for SPCCT imaging. Despite the similarity in atomic number, tungsten ($Z=74$) had significantly lower attenuation. This is possibly due to the fact that tungsten is the material of the x-ray tube anode, which causes K-edge absorption within the tube at the K-edge energy of tungsten. Besides gadolinium,

ytterbium, and tantalum, other elements whose atomic numbers are close to them (e.g. cerium, europium, terbium, hafnium) can also potentially generate the most contrast in SPCCT. Cerium and hafnium could particularly be interesting to study their feasibility as SPCCT contrast agents since their nanoparticle forms have been well-studied for other biomedical applications.⁵¹⁻⁵³

High attenuation and CNR observed from gadolinium, ytterbium and tantalum can be explained by the fact that their K-edge energies are located where there are high photon numbers both above and below the energies in a 120 kVp beam. This helps to acquire better data statistics for more accurate material decomposition and hence lower image noise. These findings in our study were demonstrated at a scanning condition of 120 kVp peak tube voltage. It is important to note that gold and bismuth – two elements that generated less contrast in this study – will likely produce stronger contrast at 140 kVp since more photons will be generated near (especially above) their K-edge energies. Several studies have examined nanoparticle development and small animal imaging with ytterbium⁵⁴⁻⁵⁶ and tantalum,^{31,32,57} indicating the potential of these two elements for further development for SPCCT contrast agents. However, more research is needed to evaluate nanoparticle behaviors, such as long-term *in vivo* cytotoxicity, biodistribution and optimal dosage before we can start clinical translation. Ease of size control and surface coating can make tantalum a more desirable element for nanoparticle-based contrast agent development than ytterbium.

For phantom images provided in Figure 2.3, iodine and water images were constructed in a similar manner as dual energy CT images in which all materials are mapped; therefore, materials other than water and iodine are also seen in these images. Since the element samples were dissolved in water or a water-like solvent (i.e. ethylene

glycol in the case of bismuth), there is some signal from these samples in the water image as well (Figure 2.3B). Similarly, the plastic of the phantom also appears on the water images due to the fact that it is composed of elements similar to the atomic numbers of hydrogen and oxygen. This also explains the slightly larger appearance of the samples in water images since the plastic tubes containing the samples also appear. In all cases, signal from calcium phosphate is seen in both iodine and water images with higher attenuation than other elements since the material decomposition algorithm classifies the attenuation pattern of calcium to be in between that of iodine and water. This agrees with observations made in previous studies using SPCCT.^{4,17}

Optimization of energy windows is an important issue for K-edge imaging since the energy thresholds of each energy bin greatly affect the material decomposition as well as CNR of the materials in SPCCT imaging. The selection of energy bins determines the spectral separation and the count rate of each energy bin as well; thus, they have to be optimized for given set of materials. For K-edge of an element to be detected, the energy bins must properly capture the K-edge. This is typically done by assigning the energy thresholds of a bin just below and above the K-edge energy. Before our study, energy thresholds for all five energy bins were optimized for each element used in this study, based on the methods described by Roessl *et al.* The optimization focused on minimizing the noise in material decomposition and improving the signal-to-noise ratio in material-specific images of each element.^{47,48} For example, energy thresholds of 30, 51, 78, 83, and 98 keV were used for gold whose K-edge energy is 80.7 keV.

Besides the energy bin thresholds, different types of material decomposition algorithms can also lead to different degrees of signal-to-noise ratio degradation and variances in noise. In this study, we performed projection space-based material

decomposition. However, decomposition can be performed on reconstructed images, which can yield different noise levels.⁵⁸ Recently, one-step inversion algorithms called statistical iterative reconstruction techniques that can improve image quality has been investigated by Mechlem *et al.*⁵⁹ The continued improvement in material decomposition techniques can lead to decreased noise levels in material-specific images of all six elements in this study.

The proof-of-concept experiments with tantalum-based nanoparticles confirmed that, as others have found, biocompatible nanoparticles can be made with this element.^{31,60} In addition, we showed for the first time that these nanoparticles can be successfully differentiated from calcium phosphate and iodine with SPCCT. The detection limit of TaONP was also comparable to that of gold in conventional CT systems (approximately 1 mg/ml). By using improved image reconstruction methods, reconstruction kernels and post-image processing (i.e. removal of ring artifacts and Gaussian blurring), it is expected that the detection limit of TaONP, as well as other elements, will continue to be improved.⁶¹ Along with other nanoparticle-based contrast agents, TaONP have further advantages over iodinated contrast agents as blood pool agents in SPCCT imaging, since their biodistribution and pharmacokinetics can be controlled by adjusting the size and surface chemistry to lessen renal damage and optimize the imaging window.⁶²

As demonstrated in this study, gadolinium, ytterbium, and tantalum can be particularly valuable elements for further developments into SPCCT contrast agents, considering their low toxicity, cost, availability, and previous uses in nanoparticle synthesis and developmental contrast agents. We also showed that these elements could work well in conventional CT scanners, which can provide additional utility of the contrast agents

made of these elements. Gadolinium-based contrast agents are commercially available and are widely used for clinical uses in MR imaging.⁶³ However, due to lower sensitivity in CT scanners, higher doses of gadolinium will likely be needed for SPCCT imaging, which may result in toxicity issues. Indeed, there is considerable concern over brain retention of gadolinium-based agents.⁶⁴ While the concern may hinder immediate use of gadolinium for SPCCT imaging, the possibility of eventual usage remains high. A recent study demonstrated the feasibility of acquiring images of diagnostic quality with gadolinium-based contrast agents at clinical MRI routine doses of 0.2 mmol/kg in human patients *via* spectral CT imaging.⁶⁵ The required doses of gadolinium-based contrast agents for *in vivo* imaging are expected to be reduced with improving sensitivity of SPCCT technology.⁶¹ Nevertheless, further work is needed to fully understand the potential use of the currently available gadolinium-based agents for SPCCT imaging.

Although contrast generation is a valuable assessment of an element's potential SPCCT imaging performance, it is one of several factors that need to be considered for CT imaging applications. For instance, in the case of cell tracking, there is a need for high contrast agent density to allow cells to take up high payloads while having good biocompatibility and stability. To date, gold nanoparticles have almost exclusively been used for cell tracking with CT¹ since they meet all of the above criteria. Therefore, gold nanoparticles may remain the platform of choice for cell tracking with SPCCT, despite the sub-optimal CNR. Inferior CNR of gold found in this study is likely due to the fact that we were using tube voltage of 120 kVp. As mentioned earlier in the discussion, gold is likely to provide better contrast at 140 kVp.²⁶ Furthermore, gold nanoparticles have been frequently used as experimental CT contrast agents in general due in part to the ability to synthesize them in a wide variety of sizes and shapes, as well as the ability to conjugate

them with targeting ligands. These are much easier to accomplish than other elements such as tantalum.⁶⁶⁻⁶⁸ We may therefore continue to see reports of gold nanoparticle SPCCT agents.

Our study provides insight into potential elements that can be developed as contrast agents for SPCCT imaging, but it has limitations. Similar studies will need to be performed in other SPCCT systems to further validate the potential elements for SPCCT contrast agents as variations in system specifications may result in different trends in CT attenuation and CNR. Moreover, the SPCCT system used in this study is a prototype of a clinical scanner under development. The final clinical scanner may have a different x-ray source, detector architecture and may use different scanning conditions, which could result in some differences with the values reported herein. Scanning in a larger FOV for larger subjects, such as human patients, may affect CNR production *via* the beam hardening effect, causing fewer photons below the K-edge energies of these elements to reach the detector. In this case, elements with higher atomic numbers will therefore produce higher CNR than for smaller subjects. This might lead to, for example, the contrast generation of tantalum being higher than that of ytterbium. All of these limitations of the study can be addressed in the future in larger phantoms or animal models as the technology approaches the clinical stage of the development.

2.6 Conclusion

In summary, the results from this study suggest that gadolinium, ytterbium and tantalum can generate high attenuation and contrast-to-noise ratio in SPCCT, indicating that these elements may be superior candidates for further development into novel contrast agents for SPCCT imaging. Our data also suggests that these elements can

potentially be effective as contrast generating media for conventional CT scanners. Lastly, we have shown that tantalum can be developed into nanoparticles that are stable and biocompatible for biological applications. These nanoparticles could be differentiated from water, iodine and calcium phosphate in SPCCT, providing potential applications in the field of cardiovascular and cancer imaging.

2.7 References

1. Kim, J.; Chhour, P.; Hsu, J.; Litt, H. I.; Ferrari, V. A.; Popovtzer, R.; Cormode, D. P., Use of nanoparticle contrast agents for cell tracking with computed tomography. *Bioconjug Chem* **2017**, *28* (6), 1581-1597.
2. Pourmorteza, A.; Symons, R.; Sandfort, V.; Mallek, M.; Fuld, M. K.; Henderson, G.; Jones, E. C.; Malayeri, A. A.; Folio, L. R.; Bluemke, D. A., Abdominal imaging with contrast-enhanced photon-counting CT: first human experience. *Radiology* **2016**, *279* (1), 239-245.
3. Cormode, D. P.; Roessler, E.; Thran, A.; Skajaa, T.; Gordon, R. E.; Schlomka, J. P.; Fuster, V.; Fisher, E. A.; Mulder, W. J.; Proksa, R.; Fayad, Z. A., Atherosclerotic plaque composition: analysis with multicolor CT and targeted gold nanoparticles. *Radiology* **2010**, *256* (3), 774-782.
4. Si-Mohamed, S.; Cormode, D. P.; Bar-Ness, D.; Sigovan, M.; Naha, P. C.; Langlois, J. B.; Chalabreysse, L.; Coulon, P.; Blevis, I.; Roessler, E.; Erhard, K.; Bussel, L.; Douek, P., Evaluation of spectral photon counting computed tomography K-edge imaging for determination of gold nanoparticle biodistribution *in vivo*. *Nanoscale* **2017**, *9* (46), 18246-18257.
5. Symons, R.; Reich, D. S.; Bagheri, M.; Cork, T. E.; Krauss, B.; Ulzheimer, S.; Kappler, S.; Bluemke, D. A.; Pourmorteza, A., Photon-counting computed tomography for vascular imaging of the head and neck: first *in vivo* human results. *Invest Radiol* **2018**, *53* (3), 135-142.
6. Willemink, M. J.; Persson, M.; Pourmorteza, A.; Pelc, N. J.; Fleischmann, D., Photon-counting CT: technical principles and clinical prospects. *Radiology* **2018**, *289* (2), 293-312.

7. Leng, S.; Zhou, W.; Yu, Z.; Halaweish, A.; Krauss, B.; Schmidt, B.; Yu, L.; Kappler, S.; McCollough, C., Spectral performance of a whole-body research photon counting detector CT: quantitative accuracy in derived image sets. *Phys Med Biol* **2017**, *62* (17), 7216-7232.
8. Yu, Z.; Leng, S.; Jorgensen, S. M.; Li, Z.; Gutjahr, R.; Chen, B.; Halaweish, A. F.; Kappler, S.; Yu, L.; Ritman, E. L.; McCollough, C. H., Evaluation of conventional imaging performance in a research whole-body CT system with a photon-counting detector array. *Phys Med Biol* **2016**, *61* (4), 1572-1595.
9. Symons, R.; Cork, T. E.; Sahbaee, P.; Fuld, M. K.; Kappler, S.; Folio, L. R.; Bluemke, D. A.; Pourmorteza, A., Low-dose lung cancer screening with photon-counting CT: a feasibility study. *Phys Med Biol* **2017**, *62* (1), 202-213.
10. Muenzel, D.; Bar-Ness, D.; Roessl, E.; Blevis, I.; Bartels, M.; Fingerle, A. A.; Ruschke, S.; Coulon, P.; Daerr, H.; Kopp, F. K.; Brendel, B.; Thran, A.; Rokni, M.; Herzen, J.; Bousset, L.; Pfeiffer, F.; Proksa, R.; Rummeny, E. J.; Douek, P.; Noel, P. B., Spectral photon-counting CT: initial experience with dual-contrast agent K-edge colonography. *Radiology* **2017**, *283* (3), 723-728.
11. Gutjahr, R.; Halaweish, A. F.; Yu, Z.; Leng, S.; Yu, L.; Li, Z.; Jorgensen, S. M.; Ritman, E. L.; Kappler, S.; McCollough, C. H., Human imaging with photon counting-based computed tomography at clinical dose levels: contrast-to-noise ratio and cadaver studies. *Invest Radiol* **2016**, *51* (7), 421-429.
12. Yeh, B. M.; FitzGerald, P. F.; Edic, P. M.; Lambert, J. W.; Colborn, R. E.; Marino, M. E.; Evans, P. M.; Roberts, J. C.; Wang, Z. J.; Wong, M. J.; Bonitatibus, P. J., Jr., Opportunities for new CT contrast agents to maximize the diagnostic potential of emerging spectral CT technologies. *Adv Drug Deliv Rev* **2017**, *113*, 201-222.

13. Jorgensen, S. M.; Korinek, M. J.; Vercnocke, A. J.; Anderson, J. L.; Halaweish, A.; Leng, S.; McCollough, C. H.; Ritman, E. L., Arterial wall perfusion measured with photon counting spectral X-ray CT. *Proc SPIE Int Soc Opt Eng* **2016**, 9967.
14. Symons, R.; Sandfort, V.; Mallek, M.; Ulzheimer, S.; Pourmorteza, A., Coronary artery calcium scoring with photon-counting CT: first *in vivo* human experience. *Int J Cardiovasc Imaging* **2019**, 35 (4), 733-739.
15. Dangelmaier, J.; Bar-Ness, D.; Daerr, H.; Muenzel, D.; Si-Mohamed, S.; Ehn, S.; Fingerle, A. A.; Kimm, M. A.; Kopp, F. K.; Bussel, L.; Roessler, E.; Pfeiffer, F.; Rummeny, E. J.; Proksa, R.; Douek, P.; Noel, P. B., Experimental feasibility of spectral photon-counting computed tomography with two contrast agents for the detection of endoleaks following endovascular aortic repair. *Eur Radiol* **2018**, 28 (8), 3318-3325.
16. Si-Mohamed, S.; Thivolet, A.; Bonnot, P. E.; Bar-Ness, D.; Kepenekian, V.; Cormode, D. P.; Douek, P.; Rousset, P., Improved peritoneal cavity and abdominal organ imaging using a biphasic contrast agent protocol and spectral photon counting computed tomography K-edge imaging. *Invest Radiol* **2018**, 53 (10), 629-639.
17. Cormode, D. P.; Si-Mohamed, S.; Bar-Ness, D.; Sigovan, M.; Naha, P. C.; Balegamire, J.; Lavenne, F.; Coulon, P.; Roessler, E.; Bartels, M.; Rokni, M.; Blevis, I.; Bussel, L.; Douek, P., Multicolor spectral photon-counting computed tomography: *in vivo* dual contrast imaging with a high count rate scanner. *Sci Rep* **2017**, 7 (1), 4784.
18. Symons, R.; Krauss, B.; Sahbaee, P.; Cork, T. E.; Lakshmanan, M. N.; Bluemke, D. A.; Pourmorteza, A., Photon-counting CT for simultaneous imaging of multiple contrast agents in the abdomen: An *in vivo* study. *Med Phys* **2017**, 44 (10), 5120-5127.

19. Lee, S.; Choi, Y. N.; Kim, H. J., Quantitative material decomposition using spectral computed tomography with an energy-resolved photon-counting detector. *Phys Med Biol* **2014**, *59* (18), 5457-5482.
20. Muenzel, D.; Daerr, H.; Proksa, R.; Fingerle, A. A.; Kopp, F. K.; Douek, P.; Herzen, J.; Pfeiffer, F.; Rummeny, E. J.; Noel, P. B., Simultaneous dual-contrast multi-phase liver imaging using spectral photon-counting computed tomography: a proof-of-concept study. *Eur Radiol Exp* **2017**, *1* (1), 25.
21. Solomon, R.; Dumouchel, W., Contrast media and nephropathy: findings from systematic analysis and Food and Drug Administration reports of adverse effects. *Invest Radiol* **2006**, *41* (8), 651-660.
22. Tepel, M.; Aspelin, P.; Lameire, N., Contrast-induced nephropathy: a clinical and evidence-based approach. *Circulation* **2006**, *113* (14), 1799-1806.
23. Gruberg, L.; Mintz, G. S.; Mehran, R.; Gangas, G.; Lansky, A. J.; Kent, K. M.; Pichard, A. D.; Satler, L. F.; Leon, M. B., The prognostic implications of further renal function deterioration within 48 h of interventional coronary procedures in patients with pre-existent chronic renal insufficiency. *J Am Coll Cardiol* **2000**, *36* (5), 1542-1548.
24. Al Zaki, A.; Hui, J. Z.; Higbee, E.; Tsourkas, A., Biodistribution, clearance, and toxicology of polymeric micelles loaded with 0.9 or 5 nm gold nanoparticles. *J Biomed Nanotechnol* **2015**, *11* (10), 1836-1846.
25. Cai, Q. Y.; Kim, S. H.; Choi, K. S.; Kim, S. Y.; Byun, S. J.; Kim, K. W.; Park, S. H.; Juhng, S. K.; Yoon, K. H., Colloidal gold nanoparticles as a blood-pool contrast agent for X-ray computed tomography in mice. *Invest Radiol* **2007**, *42* (12), 797-806.

26. Galper, M. W.; Saung, M. T.; Fuster, V.; Roessler, E.; Thran, A.; Proksa, R.; Fayad, Z. A.; Cormode, D. P., Effect of computed tomography scanning parameters on gold nanoparticle and iodine contrast. *Invest Radiol* **2012**, *47* (8), 475-481.
27. Betzer, O.; Perets, N.; Angel, A.; Motiei, M.; Sadan, T.; Yadid, G.; Offen, D.; Popovtzer, R., *In vivo* neuroimaging of exosomes using gold nanoparticles. *ACS Nano* **2017**, *11* (11), 10883-10893.
28. Zhang, Z.; Ross, R. D.; Roeder, R. K., Preparation of functionalized gold nanoparticles as a targeted X-ray contrast agent for damaged bone tissue. *Nanoscale* **2010**, *2* (4), 582-586.
29. Naha, P. C.; Zaki, A. A.; Hecht, E.; Chorny, M.; Chhour, P.; Blankemeyer, E.; Yates, D. M.; Witschey, W. R.; Litt, H. I.; Tsourkas, A.; Cormode, D. P., Dextran coated bismuth-iron oxide nanohybrid contrast agents for computed tomography and magnetic resonance imaging. *J Mater Chem B* **2014**, *2* (46), 8239-8248.
30. Swy, E. R.; Schwartz-Duval, A. S.; Shuboni, D. D.; Latourette, M. T.; Mallet, C. L.; Parys, M.; Cormode, D. P.; Shapiro, E. M., Dual-modality, fluorescent, PLGA encapsulated bismuth nanoparticles for molecular and cellular fluorescence imaging and computed tomography. *Nanoscale* **2014**, *6* (21), 13104-13112.
31. Oh, M. H.; Lee, N.; Kim, H.; Park, S. P.; Piao, Y.; Lee, J.; Jun, S. W.; Moon, W. K.; Choi, S. H.; Hyeon, T., Large-scale synthesis of bioinert tantalum oxide nanoparticles for X-ray computed tomography imaging and bimodal image-guided sentinel lymph node mapping. *J Am Chem Soc* **2011**, *133* (14), 5508-5515.
32. Bonitatibus, P. J., Jr.; Torres, A. S.; Kandapallil, B.; Lee, B. D.; Goddard, G. D.; Colborn, R. E.; Marino, M. E., Preclinical assessment of a zwitterionic tantalum oxide nanoparticle X-ray contrast agent. *ACS Nano* **2012**, *6* (8), 6650-6658.

33. McGinnity, T. L.; Dominguez, O.; Curtis, T. E.; Nallathamby, P. D.; Hoffman, A. J.; Roeder, R. K., Hafnia (HfO₂) nanoparticles as an X-ray contrast agent and mid-infrared biosensor. *Nanoscale* **2016**, *8* (28), 13627-13637.
34. Liu, Y.; Ai, K.; Liu, J.; Yuan, Q.; He, Y.; Lu, L., A high-performance ytterbium-based nanoparticulate contrast agent for *in vivo* X-ray computed tomography imaging. *Angew Chem Int Ed Engl* **2012**, *51* (6), 1437-1442.
35. Liu, Y.; Ai, K.; Liu, J.; Yuan, Q.; He, Y.; Lu, L., Hybrid BaYbF₅ nanoparticles: novel binary contrast agent for high-resolution *in vivo* X-ray computed tomography angiography. *Adv Healthc Mater* **2012**, *1* (4), 461-466.
36. Chou, S. W.; Shau, Y. H.; Wu, P. C.; Yang, Y. S.; Shieh, D. B.; Chen, C. C., *In vitro* and *in vivo* studies of FePt nanoparticles for dual modal CT/MRI molecular imaging. *J Am Chem Soc* **2010**, *132* (38), 13270-13278.
37. Remy-Jardin, M.; Dequiedt, P.; Ertzbischoff, O.; Tillie-Leblond, I.; Bruzzi, J.; Duhamel, A.; Remy, J., Safety and effectiveness of gadolinium-enhanced multi-detector row spiral CT angiography of the chest: preliminary results in 37 patients with contraindications to iodinated contrast agents. *Radiology* **2005**, *235* (3), 819-826.
38. Kim, J. Y.; Ryu, J. H.; Schellingerhout, D.; Sun, I. C.; Lee, S. K.; Jeon, S.; Kim, J.; Kwon, I. C.; Nahrendorf, M.; Ahn, C. H.; Kim, K.; Kim, D. E., Direct imaging of cerebral thromboemboli using computed tomography and fibrin-targeted gold nanoparticles. *Theranostics* **2015**, *5* (10), 1098-1114.
39. Sun, Y.; Hu, H.; Yu, B.; Xu, F. J., PGMA-based cationic nanoparticles with polyhydric iodine units for advanced gene vectors. *Bioconjug Chem* **2016**, *27* (11), 2744-2754.

40. Hainfeld, J. F.; Smilowitz, H. M.; O'Connor, M. J.; Dilmanian, F. A.; Slatkin, D. N., Gold nanoparticle imaging and radiotherapy of brain tumors in mice. *Nanomedicine (Lond)* **2013**, *8* (10), 1601-1609.
41. Betzer, O.; Shwartz, A.; Motiei, M.; Kazimirsky, G.; Gispan, I.; Damti, E.; Brodie, C.; Yadid, G.; Popovtzer, R., Nanoparticle-based CT imaging technique for longitudinal and quantitative stem cell tracking within the brain: application in neuropsychiatric disorders. *ACS Nano* **2014**, *8* (9), 9274-9285.
42. Chhour, P.; Naha, P. C.; O'Neill, S. M.; Litt, H. I.; Reilly, M. P.; Ferrari, V. A.; Cormode, D. P., Labeling monocytes with gold nanoparticles to track their recruitment in atherosclerosis with computed tomography. *Biomaterials* **2016**, *87*, 93-103.
43. Schlomka, J. P.; Roessl, E.; Dorscheid, R.; Dill, S.; Martens, G.; Istel, T.; Baumer, C.; Herrmann, C.; Steadman, R.; Zeitler, G.; Livne, A.; Proksa, R., Experimental feasibility of multi-energy photon-counting K-edge imaging in pre-clinical computed tomography. *Phys Med Biol* **2008**, *53* (15), 4031-4047.
44. Mullner, M.; Schlattl, H.; Hoeschen, C.; Dietrich, O., Feasibility of spectral CT imaging for the detection of liver lesions with gold-based contrast agents - A simulation study. *Phys Med* **2015**, *31* (8), 875-881.
45. Cormode, D. P.; Naha, P. C.; Fayad, Z. A., Nanoparticle contrast agents for computed tomography: a focus on micelles. *Contrast Media Mol Imaging* **2014**, *9* (1), 37-52.
46. Steadman, R.; Herrmann, C.; Livne, A., ChromAIX2: A large area, high count-rate energy-resolving photon counting ASIC for a spectral CT prototype. *Nucl Instrum Meth A* **2017**, *862*, 18-24.

47. Roessl, E.; Brendel, B.; Engel, K.; Schlomka, J.; Thran, A.; Proksa, R., Sensitivity of photon-counting based K-edge imaging in X-ray computed tomography. *IEEE Trans Med Imaging* **2011**, *30* (9), 1678-1690.
48. Roessl, E.; Herrmann, C., Cramer-Rao lower bound of basis image noise in multiple-energy x-ray imaging. *Phys Med Biol* **2009**, *54* (5), 1307-1318.
49. Brown, A. L.; Naha, P. C.; Benavides-Montes, V.; Litt, H. I.; Goforth, A. M.; Cormode, D. P., Synthesis, X-ray opacity, and biological compatibility of ultra-high payload elemental bismuth nanoparticle X-ray contrast agents. *Chem Mater* **2014**, *26* (7), 2266-2274.
50. García K. P.; Zarschler K.; Barbaro L.; Barreto J. A.; O'Malley W.; Spiccia L.; Stephan H.; Graham B., Zwitterionic-coated “stealth” nanoparticles for biomedical applications: recent advances in countering biomolecular corona formation and uptake by the mononuclear phagocyte system. *Small* **2014**, *10*, 2516–2529.
51. Bonvalot, S.; Rutkowski, P. L.; Thariat, J.; Carrere, S.; Ducassou, A.; Sunyach, M. P.; Agoston, P.; Hong, A.; Mervoyer, A.; Rastrelli, M.; Moreno, V., et al., NBTXR3, a first-in-class radioenhancer hafnium oxide nanoparticle, plus radiotherapy versus radiotherapy alone in patients with locally advanced soft-tissue sarcoma (Act.In.Sarc): a multicentre, phase 2-3, randomised, controlled trial. *Lancet Oncol* **2019**, *20* (8), 1148-1159.
52. Hirst, S. M.; Karakoti, A. S.; Tyler, R. D.; Sriranganathan, N.; Seal, S.; Reilly, C. M., Anti-inflammatory properties of cerium oxide nanoparticles. *Small* **2009**, *5* (24), 2848-2856.

53. Kwon, H. J.; Cha, M. Y.; Kim, D.; Kim, D. K.; Soh, M.; Shin, K.; Hyeon, T.; Mook-Jung, I., Mitochondria-targeting ceria nanoparticles as antioxidants for alzheimer's disease. *ACS Nano* **2016**, *10* (2), 2860-2870.
54. Liu, J.; Xin, R.; Li, Z.; Golamaully, R.; Zhang, Y.; Zhang, J.; Yuan, Q.; Liu, X., Large-scale and facile synthesis of biocompatible Yb-based nanoparticles as a contrast agent for *in vivo* X-ray computed tomography imaging. *Curr Top Med Chem* **2013**, *13* (4), 513-518.
55. Liu, Y.; Liu, J.; Ai, K.; Yuan, Q.; Lu, L., Recent advances in ytterbium-based contrast agents for *in vivo* X-ray computed tomography imaging: promises and prospects. *Contrast Media Mol Imaging* **2014**, *9* (1), 26-36.
56. Pan, D.; Schirra, C. O.; Senpan, A.; Schmieder, A. H.; Stacy, A. J.; Roessl, E.; Thran, A.; Wickline, S. A.; Proska, R.; Lanza, G. M., An early investigation of ytterbium nanocolloids for selective and quantitative "multicolor" spectral CT imaging. *ACS Nano* **2012**, *6* (4), 3364-3370.
57. Torres, A. S.; Bonitatibus, P. J., Jr.; Colborn, R. E.; Goddard, G. D.; FitzGerald, P. F.; Lee, B. D.; Marino, M. E., Biological performance of a size-fractionated core-shell tantalum oxide nanoparticle x-ray contrast agent. *Invest Radiol* **2012**, *47* (10), 578-587.
58. Niu, T.; Dong, X.; Petrongolo, M.; Zhu, L., Iterative image-domain decomposition for dual-energy CT. *Med Phys* **2014**, *41* (4), 041901.
59. Mechlem, K.; Ehn, S.; Sellerer, T.; Braig, E.; Munzel, D.; Pfeiffer, F.; Noel, P. B., Joint statistical iterative material image reconstruction for spectral computed tomography using a semi-empirical forward model. *IEEE Trans Med Imaging* **2018**, *37* (1), 68-80.

60. Bonitatibus, P. J., Jr.; Torres, A. S.; Goddard, G. D.; FitzGerald, P. F.; Kulkarni, A. M., Synthesis, characterization, and computed tomography imaging of a tantalum oxide nanoparticle imaging agent. *Chem Commun (Camb)* **2010**, 46 (47), 8956-8958.
61. Bernstein, A. L.; Dhanantwari, A.; Jurcova, M.; Cheheltani, R.; Naha, P. C.; Ivanc, T.; Shefer, E.; Cormode, D. P., Improved sensitivity of computed tomography towards iodine and gold nanoparticle contrast agents *via* iterative reconstruction methods. *Sci Rep* **2016**, 6, 26177.
62. FitzGerald, P. F.; Butts, M. D.; Roberts, J. C.; Colborn, R. E.; Torres, A. S.; Lee, B. D.; Yeh, B. M.; Bonitatibus, P. J., Jr., A proposed computed tomography contrast agent using carboxybetaine zwitterionic tantalum oxide nanoparticles: imaging, biological, and physicochemical performance. *Invest Radiol* **2016**, 51 (12), 786-796.
63. Guglielmo, F. F.; Mitchell, D. G.; Gupta, S., Gadolinium contrast agent selection and optimal use for body MR imaging. *Radiol Clin North Am* **2014**, 52 (4), 637-656.
64. McDonald, R. J.; McDonald, J. S.; Kallmes, D. F.; Jentoft, M. E.; Murray, D. L.; Thielen, K. R.; Williamson, E. E.; Eckel, L. J., Intracranial gadolinium deposition after contrast-enhanced MR imaging. *Radiology* **2015**, 275 (3), 772-782.
65. Nadjiri, J.; Pfeiffer, D.; Straeter, A. S.; Noel, P. B.; Fingerle, A.; Eckstein, H. H.; Laugwitz, K. L.; Rummeny, E. J.; Braren, R.; Rasper, M., Spectral computed tomography angiography with a gadolinium-based contrast agent: first clinical imaging results in cardiovascular applications. *J Thorac Imaging* **2018**, 33 (4), 246-253.
66. Almeida, J. P.; Figueroa, E. R.; Drezek, R. A., Gold nanoparticle mediated cancer immunotherapy. *Nanomedicine* **2014**, 10 (3), 503-514.

67. Chhour, P.; Kim, J.; Benardo, B.; Tovar, A.; Mian, S.; Litt, H. I.; Ferrari, V. A.; Cormode, D. P., Effect of gold nanoparticle size and coating on labeling monocytes for CT tracking. *Bioconjug Chem* **2017**, 28 (1), 260-269.
68. Curry, T.; Kopelman, R.; Shilo, M.; Popovtzer, R., Multifunctional theranostic gold nanoparticles for targeted CT imaging and photothermal therapy. *Contrast Media Mol Imaging* **2014**, 9 (1), 53-61.

CHAPTER 3: DEVELOPMENT OF POLYMER-ENCAPSULATED “POLYMETAL” NANOPARTICLES FOR CT IMAGING

3.1 Abstract

Numerous formulations of nanoparticle-based X-ray computed tomography (CT) contrast agents made of heavy metal elements are under investigation for their ability to provide improved CT imaging. Most of these experimental nanoparticle-based CT contrast agents have been developed with atoms of a single element thus far. However, inspired by the composites formed from multiple elements used in radioprotective garments, we hypothesized that contrast agents made of several elements whose K-edge energies are spaced out in the high photon flux region could achieve high, broadband X-ray attenuation for different energy spectra used in clinical setting. Herein, we synthesized sub-5 nm core inorganic nanoparticles made of gold, tantalum, and cerium, and encapsulated them in polymeric nanoparticles to form polymetal nanoparticles (PMNP). We found that PMNP with multiple payload elements generate higher and more stable CT contrast than contrast agents made from a single contrast generating material, demonstrating the potential benefits of incorporating multiple suitable elements as CT contrast payloads.

3.2 Introduction

As the field of nanomedicine has advanced, a myriad of nanoparticle formulations has been developed for imaging applications. Nanoparticle-based contrast agents for X-ray computed tomography (CT) imaging are no exception to this substantial research interest.¹⁻⁷ This interest stems from the numerous advantages of CT, such as high spatial and temporal resolution, fast acquisition time, no depth limit, and wide clinical availability. These inherent properties of CT have allowed it to become one of the most valuable instruments for cardiovascular imaging. However, current FDA-approved CT contrast agents for intravenous administration (i.e., iodinated small molecules) have several drawbacks. These drawbacks include injection of high doses, short imaging window and possibility of allergic reactions and renal toxicity, which are mostly caused by short blood circulation times of small molecules.⁸⁻¹⁰ The concern over contrast-induced nephropathy is particularly serious in patients with renal insufficiency. Since patients with vascular diseases (who undergo frequent CT imaging for diagnoses) often have comorbid renal diseases,¹¹ there is a need to develop alternative CT blood pool contrast agents.

Despite the need, no new CT contrast agent has been approved for clinical use in nearly three decades;¹² however, this might soon change as numerous sizes, shapes, and structures of experimental CT contrast agents have been recently reported, complementing the rapid progression of CT technology in detectors and image reconstruction methods.^{1,6,13} Most of these reports have focused on nanoparticles formed from dense, heavy metal elements, such as gadolinium, ytterbium, tantalum, gold, and bismuth.¹⁴⁻¹⁹ Among nanoparticles made of these elements, gold nanoparticles (AuNP) are by far the most well-studied CT contrast agents due to their favorable characteristics. These characteristics include high elemental density ($d = 19.3 \text{ g/cm}^3$), excellent

biocompatibility, and ease of control over its size, morphology, and surface chemistry.^{20,21} However, gold is a relatively expensive material whose use could potentially increase the cost of CT imaging. Another heavy metal element that has been studied is tantalum.^{4,16,22,23} Tantalum is also an appealing element for contrast agent development because of its high density ($d = 16.4 \text{ g/cm}^3$) and its K-edge energy (67.4 keV), which is located in a high photon flux region.²⁴ Moreover, a recent study from Kim et al. identified tantalum as one of the most *viable* elements for nanoparticle contrast agent development for CT imaging by demonstrating tantalum's high CT contrast production as compared to other candidate elements.²³ Many other candidate elements exist that may be suitable to be used as novel CT contrast agents. An element with high potential, but has rarely been investigated for CT imaging, is cerium. Cerium also has its K-edge energy (40.4 keV) located in a high X-ray photon flux region, and cerium-based nanoparticles have been well-studied for numerous biomedical applications using their antioxidant activities and ROS scavenging abilities.²⁵⁻²⁷

Radioprotective garments worn by interventional radiologists are commonly known as lead clothing; however, they frequently contain a minority of lead, or no lead at all. This is because it is more effective in X-ray attenuation and lighter in weight to use composites of elements, such as tungsten, tin, barium, antimony, and bismuth, whose K-edges are spread through the range of energies used in medical imaging.^{28,29} Inspired by such composites in radioprotective garments, we hypothesized that a contrast agent that incorporates multiple elements whose K-edges are spread over the diagnostic X-ray energy range might prove to have high contrast generation. The K-edge energies of the elements noted above (gold = 80.7 keV, tantalum = 67.4 keV, cerium = 40.4 keV) span the high photon flux regions of the X-ray spectra in the diagnostic range of tube voltage

settings for μ CT imaging (Figure 3.1A) and clinical CT imaging (Figure 3.1B). Moreover, tantalum and cerium are cheaper than some of the leading elements for CT contrast agent development, such as gold and platinum.²³ Thus, polymetal nanoparticles (PMNP) can potentially be lower in cost.

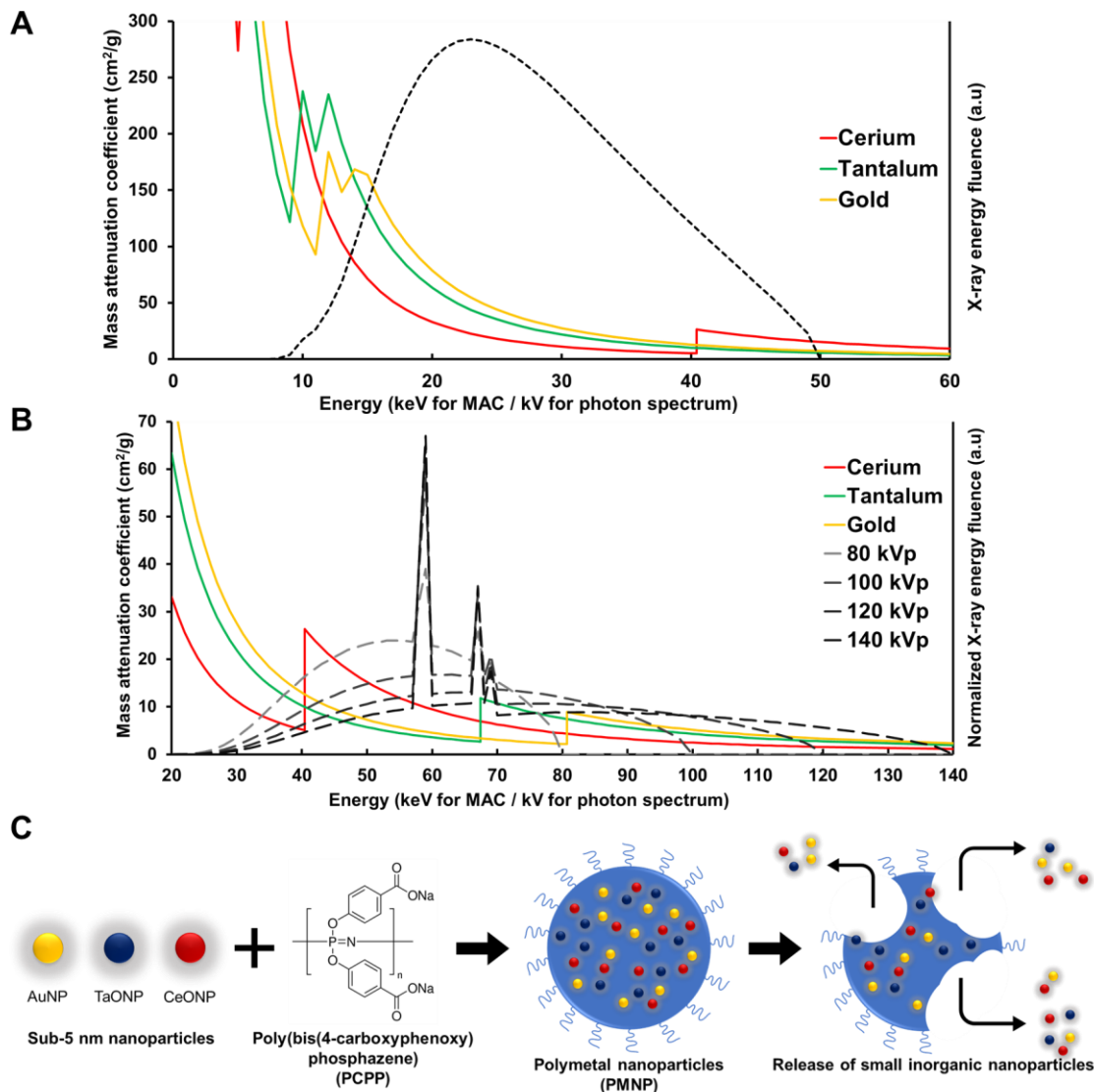


Figure 3.1 Contrast generating materials and structure of PMNP.

Mass attenuation coefficient of cerium, tantalum, and gold and estimated X-ray photon spectra of (A) a MILabs μ CT scanner at 50 kVp tube voltage and (B) a SOMATOM Force

clinical CT scanner at 80, 100, 120, and 140 kVp. (C) Schematic depiction of PMNP formation and breakdown.

Our PMNP formulation is designed to encapsulate small gold, tantalum, and cerium nanoparticles that are sub-5 nm in core diameter in a larger polymer-based nanoparticle made of biodegradable poly-di(carboxylatophenoxy)phosphazene (PCPP) (Figure 3.1C). PCPP belongs in a family of polymers known as polyphosphazenes, whose chemistry is defined by its phosphorus–nitrogen backbone. These polymers are well-studied for numerous biomedical applications, such as adjuvants for immunization and drug carriers, due to their excellent biocompatibility, tunability, and hydrophilicity.³⁰⁻³² These polymers are suitable for encapsulating small nanoparticles with hydrophilic coatings due to their hydrophilicity. They also slowly degrade into harmless hydrophilic byproducts, such as phosphate, tyrosine, ammonia, and 4-hydroxybenzoic acid, allowing PCPP-based nanoparticles to remain intact for several hours before degradation.³³ Our findings in this study suggest that our PMNP formulation can successfully encapsulate small sub-5 nm core inorganic nanoparticles made from gold, tantalum, and cerium. We have also shown that these PMNP are cytocompatible and biodegradable with robust CT contrast properties.

3.3 Materials and methods

3.3.1 Materials

Gold(III) chloride trihydrate (>99.9% trace metals basis), tantalum(V) ethoxide (99.98%), cerium(III) nitrate hexahydrate (99.99%), L-glutathione reduced, poly(acrylic acid), cyclohexane, IGEPAL CO-520, ammonium hydroxide solution (28.0–30.0%

NH₃ basis), sodium hydroxide concentration (0.1 N), poly(bis(4-carboxyphenoxy)phosphazene) disodium salt (PCPP, 1 MDa), sodium borohydride, spermine tetrahydrochloride, and calcium chloride dihydrate were purchased from Sigma-Aldrich (St. Louis, MO). Herringbone microfluidic chip mixers were obtained from Microfluidic ChipShop (Jena, Germany). 2-(Carbomethoxy)ethyltrimethoxysilane and 3-(trimethoxysilyl)propyl-*N,N,N*-trimethylammonium chloride were purchased from Gelest, Inc. (Morrisville, PA). Methoxy-poly(ethylene glycol)-*block*-poly(L-lysine hydrochloride) (PEG-PLL, PEG MW 5000, PLL MW 4900) was purchased from Alamanda Polymers (Huntsville, AL). HepG2, J774A.1, Renca, and SVEC4–10 cell lines were purchased from ATCC (Manassas, VA). LIVE/DEAD assay kits were acquired from Life Technologies Invitrogen (Grand Island, NY).

3.3.2 Gold nanoparticle synthesis

Sub-5 nm gold nanoparticles were synthesized *via* a modified Turkevich method (Figure 3.2). Briefly, gold(III) chloride salt in water was reduced by dropwise addition of sodium borohydride solution. After the mixture was stirred for 30 min, glutathione was added to the solution to cap the nanoparticle surface. The resulting solution was washed with deionized water three times in 10 kDa molecular cutoff centrifugation tubes and was dispersed in PBS.

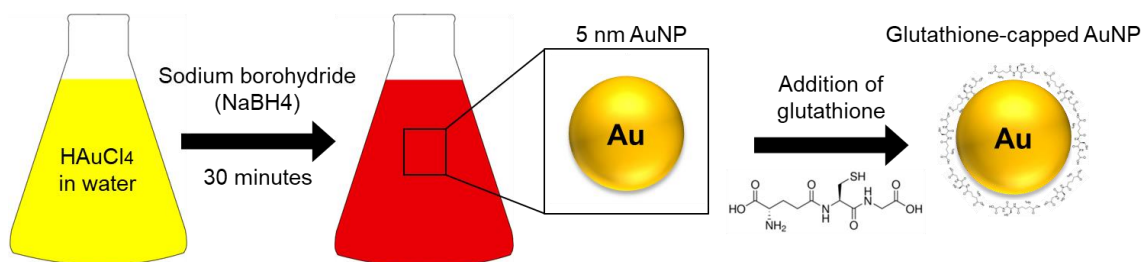


Figure 3.2 Schematic depiction of small glutathione-coated AuNP synthesis.

3.3.3 Tantalum oxide nanoparticle synthesis

Tantalum oxide nanoparticles (TaONP) were synthesized by a modified reverse microemulsion method described by Kim et al.²³ Tantalum(V) ethoxide solution was added to 20 mL of cyclohexane-based microemulsion solution that contains 3 g of IGEPAL CO-520 and 75 mM NaOH solution. After 15 min, 250 μ L of 2-(carbomethoxy)ethyltrimethoxysilane and 500 μ L of 3-(trimethoxy)silyl)propyl-*N,N,N*-trimethylammonium chloride were added to render the nanoparticle surfaces hydrophilic. A white sediment formed at the bottom of the flask after 24 h of stirring. After the colorless supernatant was carefully removed, the white sediment was dispersed in 5 mL of 5 M ammonium hydroxide solution and stirred for 30 min. Subsequently, 25 mL of ultrapure water was added and the resulting solution was allowed to stir at room temperature for 2 h. The resulting solution was then centrifuged at 2500g for 30 min. The clear solution in the supernatant was further purified by centrifugation, washed with deionized water three times at 2500g for 30 min in 10 kDa molecular cutoff centrifugation tubes, and dispersed in PBS.

3.3.4 Cerium oxide nanoparticle synthesis

Small cerium oxide nanoparticles (CeONP) were synthesized by modifying an alkaline-based precipitation method described by Perez et al (Figure 3.3).³⁴ 217 mg of cerium nitrate hexahydrate salt dissolved in 4 mL of deionized water was mixed with 50 mg of poly(acrylic acid) polymer dissolved in 2 mL of deionized water. The resulting mixture was then added to 95 mL of 0.4 M ammonium hydroxide solution. After being stirred for 24 h, the solution turned from turbid light brown to clear yellow. The resultant

nanoparticle solution was centrifuged at 2600g for 30 min, and the yellow supernatant was collected. The supernatant was then washed with deionized water 5 times in 10 kDa molecular cutoff centrifugation tubes and suspended in PBS.

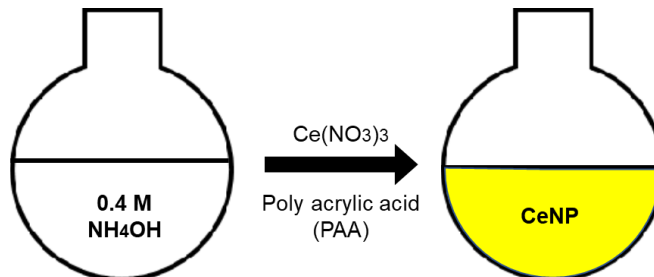


Figure 3.3 Schematic depiction of poly(acrylic acid)-coated CeONP synthesis.

3.3.5 Polymetal nanoparticle synthesis

PCPP-based nanoparticles were synthesized on the basis of a method previously reported by Cheheltani et al.³⁵ A herringbone mixer microfluidic chip was utilized to yield monodispersed and uniformly sized nanoparticles as shown in Figure 3.4. In this method, 2 mL of 0.1% (w/v) PCPP solution and 2 mL of 0.01% (w/v) spermine solution that also contains 1.45 μ L of 3.5% PEG-PLL (0.05 mg) were both prepared in PBS. The pH levels of these solutions were adjusted to 7.4 before loading each solution in a 10 mL syringe. Subsequently, both solutions were flowed through the mixer microfluidic chip at a flow rate of 6 mL/min. The resultant output solution was then quickly added to 100 mL of 8.8% (w/v) CaCl₂ solution. After being stirred for 20 min, the solution was purified by centrifugation at 550g for 7 min in DI water three times. To encapsulate small nanoparticles in PCPP, desired amounts of AuNP and CeONP were added to the PCPP solution, and TaONP were added to the spermine and PEG-PLL solution before loading them in the syringes.

The amounts of added PEG-PLL were varied from 0 to 0.2 mg to synthesize PMNP of varying sizes.

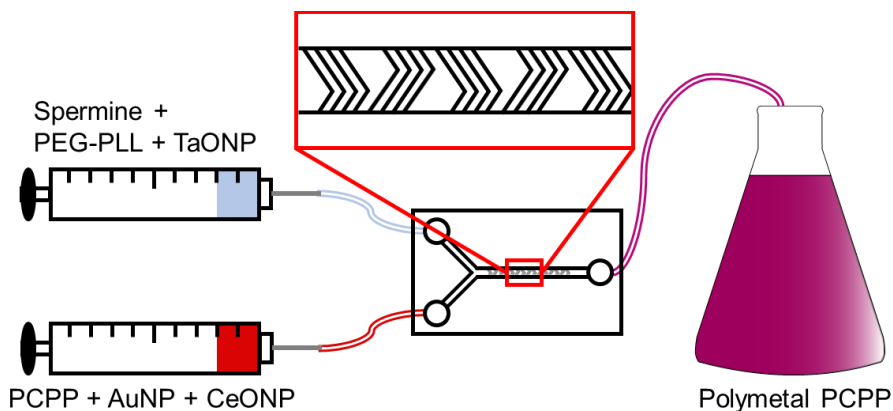


Figure 3.4 Schematic illustration of PMNP synthesis using a microfluidic chip mixer.

3.3.6 Nanoparticle characterization

Transmission electron microscopy (TEM) was used to determine the core sizes and morphologies of the small metal nanoparticles and PCPP nanoparticles. The images were acquired using a Tecnai T12 microscope (FEI, Hillsboro, OR) or a JEOL 1010 microscope (JEOL Ltd., Tokyo, Japan). Diameters of 500 individual nanoparticles of each formulation were manually measured on TEM images using ImageJ. The hydrodynamic diameter and zeta potential of the nanoparticles were assessed by using a Nano-ZS-90 Zetasizer (Malvern Instruments, Worcestershire, UK) by preparing the samples at 0.2 mg/mL in concentration. The concentrations of the elemental payloads in the nanoparticles were measured by using ICP-OES (Spectro Analytical Instruments GmbH, Kleve, Germany).

3.3.7 EDS elemental mapping

Energy-dispersive X-ray spectroscopy (EDS) imaging was used to confirm the encapsulation of metal nanoparticles of all three elements and to investigate their spatial distribution in an individual PMNP. A FEI Quanta 600 Environmental scanning electron microscope (FEI, Hillsboro, OR) equipped with a Bruker Quantax Silicon Drift Detector for EDS analysis was used. The samples were prepared on copper grids. M-edge energy mappings were used for the presence of gold and tantalum and L-edge energy mapping for the presence of cerium in the field of view. A mixed population of single metal PCPP nanoparticles (SMNP), each encapsulating either AuNP, TaONP, or CeONP, was used as a control to confirm the accuracy of elemental mapping.

3.3.8 *In vitro* polymetal nanoparticle degradation study

PMNP and SMNP (AuPCPP represents AuNP encapsulating PCPP nanoparticles, TaPCPP represents TaONP encapsulating PCPP nanoparticles, and CePCPP represents CeONP encapsulating PCPP nanoparticles) formulations at their maximum loading capacities were added to 2 mL of PBS containing 10% fetal bovine serum at a concentration of 0.15 mg/mL in payload elements (e.g., gold, tantalum, and cerium in PMNP and gold in AuPCPP). The solutions were continuously flowed through platinum cured silicon tubing that were 1.42 mm in internal diameter *via* a FH100M multichannel peristaltic pump (Fisher Scientific, Hampton, NH) at a volumetric flow rate of 5 mL/min. At days 1, 2, 4, and 7 of dynamic incubation, the solutions were collected and centrifuged at 500g for 5 min. The concentrations of gold, cerium, and tantalum in the supernatant and the pellet were analyzed *via* ICP-OES to evaluate the release of small metal nanoparticles at each time point. The amounts of released nanoparticles were calculated by dividing the

concentration measured in the supernatant by the concentrations measured in both the supernatant and the pellet. The samples were prepared in triplicates. TEM images of partially degraded PMNP were also acquired to confirm the release of core nanoparticles.

3.3.9 *In vitro* cytocompatibility assessment

The LIVE/DEAD assay was used to evaluate the safety and cytotoxicity of the core metal nanoparticles and the PCPP formulations with HepG2 (hepatocytes), Renca (epithelial kidney cells), and SVEC4-10EHR1 (endothelial cells). The cells were cultured in accordance with ATCC recommendations. 1.0×10^5 cells were seeded in each well of 24-well plates and were cultured for 24 h at 37 °C and 5% CO₂. After 24 h of culture, the medium was removed and replaced with fresh medium that contains the payload elements of a range of concentrations (i.e., 0.025 mg/mL to 1 mg/mL). The cells were incubated with the nanoparticle-treated media for 8 h before they were washed with DPBS and treated with LIVE/DEAD stain (4 uL of 3.2 mM Hoechst 33343, 1 uL of calcein AM, and 2 uL of ethidium homodimer-1 in 2 mL of DPBS) for 20 min. The stained cells were imaged with a Nikon Eclipse Ti-U fluorescence microscope. Images of cell nuclei, live cells, and dead cells were acquired at four different fields of view in each well. The numbers of live and dead cells were counted to calculate the cell *viability* in percentage (*viability* % = live cell count/total cell count). The experiment was repeated three times for each cell line for a total of 12 measurements per data point ($n = 3$, field of view = 4).

3.3.10 *In vitro* phantom CT imaging

Each PCPP formulation was suspended in 1% agar gel at concentrations of 0, 0.5, 1, 2, 4, 6, and 8 mg/mL ($n = 3$ per concentration). Each sample was prepared in a 0.2 mL

flat cap microcentrifuge tube. These samples were secured in a plastic rack along with a tube containing water and a tube containing no solution (or air) for μ CT imaging. μ CT imaging was performed using a MILabs μ CT scanner (MILabs, Utrecht, The Netherlands). The images were acquired using a standard protocol with 0.1 mm beryllium and 0.5 mm aluminum filtration, tube voltage of 50 kVp, tube current at 0.24 mA, step angle of 0.75°, and exposure time of 75 ms. The identical samples were loaded in a custom-made, acrylonitrile butadiene styrene tube holder that is designed to fit in the borehole of an anthropomorphic thorax phantom body (QRM GmbH, Mohrendorf, Germany) for imaging with a SOMATOM Force clinical CT scanner (Siemens Healthineers, Erlangen, Germany). The phantom body mimics human organs in the thorax in terms of density, CT attenuation, and size (200 × 300 × 200 mm). The CT images were acquired using a customized protocol adapted from Siemens original adult abdomen routine imaging protocol at 80, 100, 120, and 140 kVp. The following parameters were used: beam filtration of 0.3 mm titanium and 0.5 mm aluminum, anode angle of 8°, scan mode of helical acquisition, X-ray tube current of 360 mA, exposure time of 0.5 s, slice thickness of 0.5 cm, and field of view of 370 × 370 mm. For both μ CT and CT imaging, the images were analyzed by using OsiriX software (Pixmeo, Bernex, Switzerland). Circular ROIs were drawn on five different axial planes of each tube. The mean attenuation values were recorded and normalized to the values from our control tubes with 1% agar gel (i.e., 0 mg/mL solution). Attenuation rate was defined by the slope of the linear regression line that models the linear relationship between attenuation and elemental concentration in either mg/mL or mM.

3.3.11 Simulation of payload element contribution to CT attenuation

A custom-written Python code was used to estimate the relative contribution from each payload element to the CT attenuation of PMNP under imaging conditions used in this study (i.e., 50 kVp in μ CT imaging and 80, 100, 120, and 140 kVp in clinical CT imaging). In this model, CT attenuation of PMNP is calculated using elemental attenuation values of materials in PMNP (i.e., water, PCPP polymer, gold, tantalum, and cerium) from National Institute of Standards and Technology (NIST), density of payload elements (i.e., gold, tantalum, and cerium), and estimated X-ray source spectra (beam filtration of 0.1 mm beryllium + 0.5 mm aluminum for μ CT imaging and 0.3 mm titanium + 0.5 mm aluminum for clinical CT imaging).

3.3.12 *In vivo* mice imaging

All animal experiments were performed in accordance with the protocols approved by University Laboratory Animal Resources in conjunction with the Institutional Animal Care and Use Committee at the University of Pennsylvania. *In vivo* CT images were acquired from a MILabs μ CT scanner, using the same scanning parameters from the phantom imaging. After acquiring pre-injection images, C57BL/6J mice were injected with either 40 μ L of PMNP ($n = 3$) or AuPCPP ($n = 3$) containing 0.1 mg of the payload (i.e., gold in AuPCPP and gold, tantalum, and cerium combined for PMNP) and were scanned again immediately after post-injection. Both formulations were injected in the left thigh muscle of the mice. The acquired images were subsequently analyzed with Osirix. Using a 3D region growing segmentation function, 3D regions of interest (ROI) that enclosed the injection sites were isolated and highlighted. The total attenuation that was generated by either AuPCPP or PMNP was quantified by addition of the attenuation values (in

Hounsfield Unit) of each voxel within the 3D ROI and subtraction of the total attenuation generated by the soft tissue from the pre-injection scan from this number.

3.3.13 Statistical analysis

The slope (m_x) and the standard error of fit (e_x) of attenuation rates from μ CT and CT were calculated using the least-squares method of linear regression. One-way analysis of variance (ANOVA) was used to test if there is an overall difference between the groups in safety and cytotoxicity, payload loading ratio, biodegradability, and attenuation rates. In cases in which the p -value from the ANOVA test indicated that there is an overall significant difference between the groups ($p \leq 0.05$), Tukey–Kramer HSD (honestly significant difference) posthoc test was used to confirm which specific pairs of groups had significant differences. A two-sample t test was used to compare total attenuation generated by PMNP and AuPCPP from *in vivo* imaging. Error bars in the graphs represent one standard deviation unless indicated otherwise.

3.4 Results

3.4.1 Core nanoparticles syntheses and characterization

Small core nanoparticles, AuNP, TaONP, and CeONP, were synthesized and capped with ligands that provide hydrophilicity and stability in biological fluids. The core sizes of AuNP, TaONP, and CeONP were determined to be 3.7 ± 0.7 , 4.8 ± 0.7 , and 2.8 ± 0.6 nm, respectively, while their hydrodynamic diameters were slightly larger in each case (Figure 3.5 A,B). The zeta potentials of AuNP and TaONP that were both capped with ligands of zwitterionic charges were closer to neutral when compared to that of CeONP, which was capped with negatively charged poly(acrylic acid).

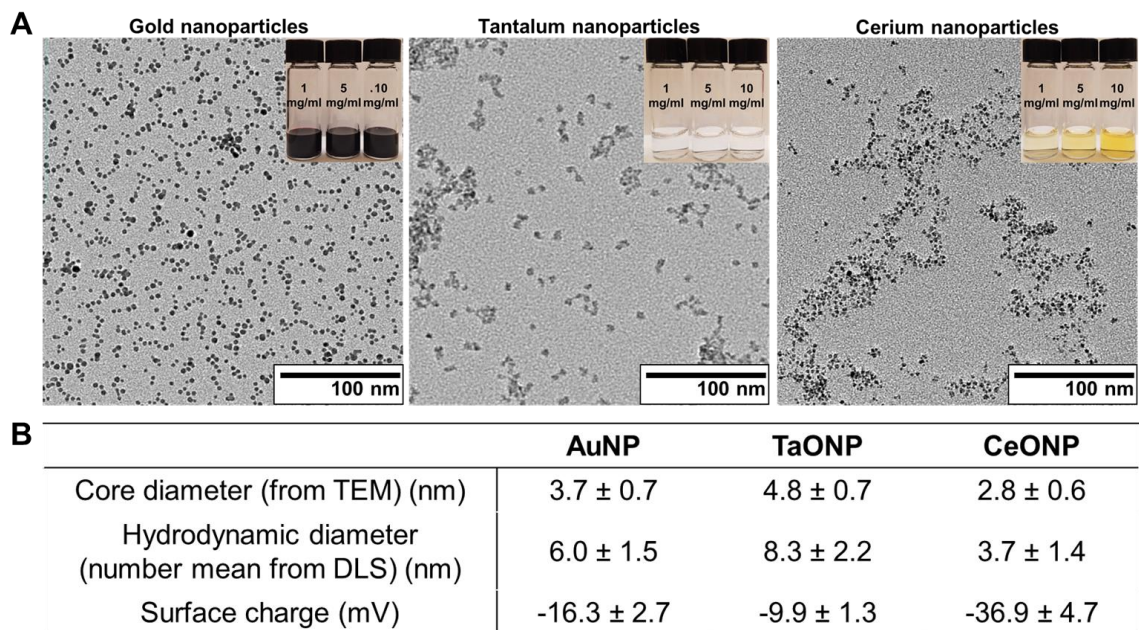


Figure 3.5 Characterization of small core metal nanoparticles of PMNP.

(A) TEM of small core metal nanoparticles and photos of the corresponding nanoparticles at concentrations of 1, 5, and 10 mg/mL (top right insets). (B) The core and hydrodynamic diameters and surface charge of the small core metal nanoparticles.

3.4.2 *In vitro* cytocompatibility of core nanoparticles

The safety and cytotoxicity of these small metal nanoparticles were assessed by incubating them with cell types that would likely have the highest exposure upon intravenous injection (i.e., endothelial cells (SVEC4-10EHR1), liver hepatocytes (HepG2), and kidney cells (Renca)) for 8 h. While there were statistically significant differences for some of the treatment concentrations for TaONP and CeONP for all cell types when compared to the control groups (0 mg/mL), the lowest cell viability observed was $96.2 \pm 3\%$ (for Renca cells incubated with TaONP at 1.0 mg Ta/mL), indicating that the reductions

were not substantial (Figure 3.6). These results justified the use of these nanoparticles in the next steps of this study.

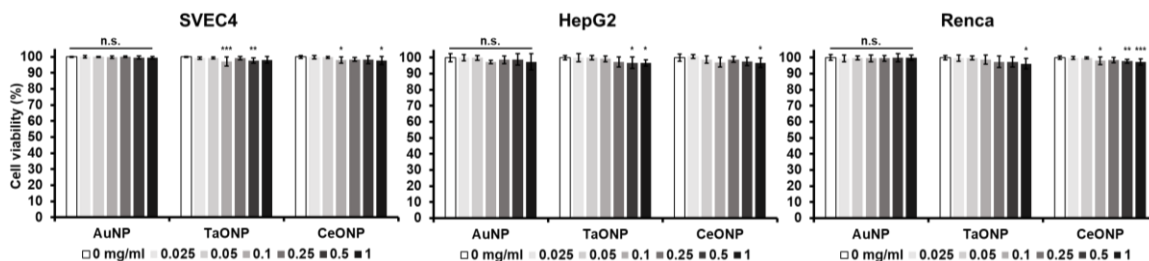


Figure 3.6 *In vitro* cell viability of small nanoparticles.

Normalized cell viability of SVEC4, HepG2, and Renca after 8 h of incubation with AuNP, TaONP, and CeONP (n.s. = not significant or $p > 0.05$, * = $p \leq 0.05$, ** = $p \leq 0.01$, *** = $p \leq 0.001$ as compared to the control group (0 mg/mL)).

3.4.3 Encapsulation of core nanoparticles for polymetal nanoparticle synthesis

The aforementioned AuNP, TaONP, and CeONP formulations were successfully incorporated into PCPP nanoparticles either individually to form SMNP or jointly to form PMNP. We assessed the loading capacity of both SMNP and PMNP that are synthesized with addition of 25 μg PEG-PLL/mg PCPP (which results in unloaded PCPP nanoparticles with an average diameter of 102.4 nm). In the case of AuPCPP, more than 5 mg of gold payload could be encapsulated per mg of PCPP polymer used during the synthesis without deviation from spherical morphology (Figure 3.7A). Similarly, up to 1.25 mg of tantalum and 0.375 mg of cerium per mg of PCPP could be loaded in their corresponding SMNP formulations (Figure 3.7B,C). Less tantalum and cerium incorporation can be explained by their lower elemental densities ($d_{\text{Ta}} = 16.6 \text{ g/cm}^3$, $d_{\text{Ce}} = 6.8 \text{ g/cm}^3$) when compared to the density of gold ($d_{\text{Au}} = 19.3 \text{ g/cm}^3$) and the presence of other constituents in the core of TaONP and CeONP (i.e., oxygen atoms). When AuNP, TaONP, and CeONP

at equal concentrations were encapsulated collectively to form PMNP, a maximum of 1 mg of total payload (gold + tantalum + cerium) per mg of PCPP polymer could be loaded without disrupting the morphology (Figure 3.7D,E). At the maximum loading capacity, the mean diameter of PMNP increased by 35% when compared to that of non-loaded PCPP nanoparticles (Figure 3.8). As seen in both SMNP and PMNP, incorporation of higher payloads increased the diameter of PCPP nanoparticles.

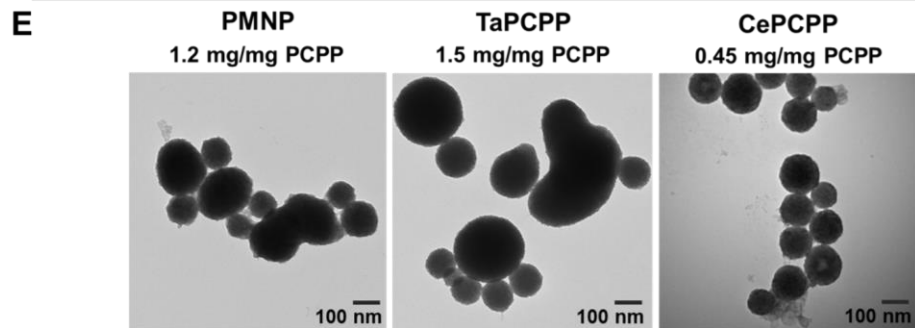
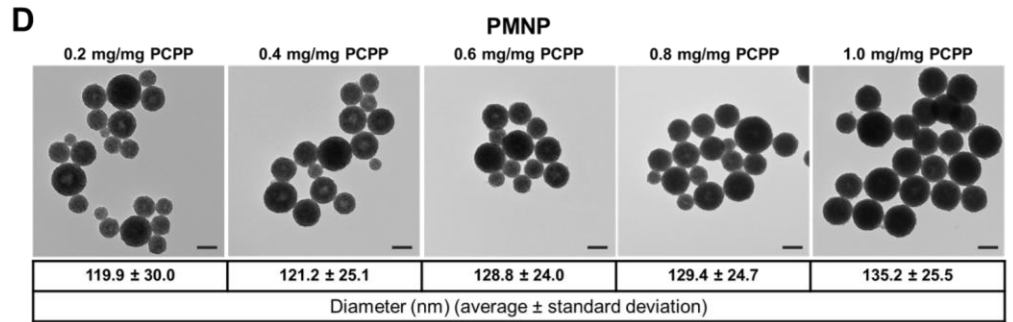
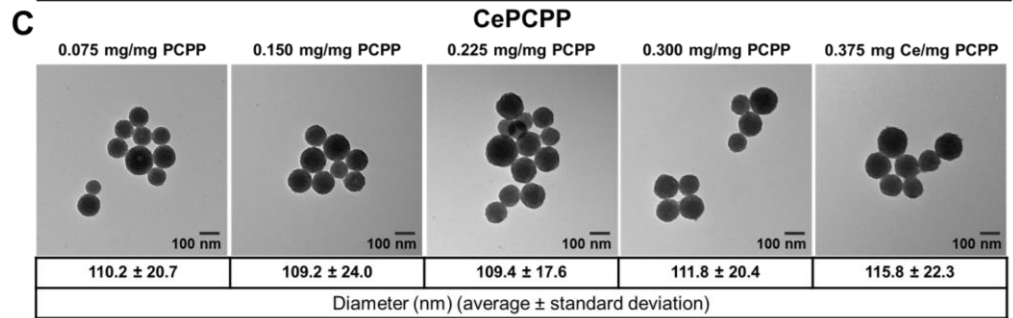
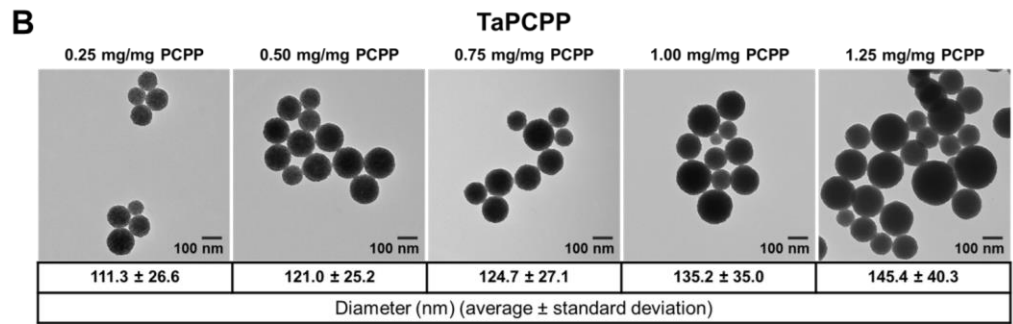
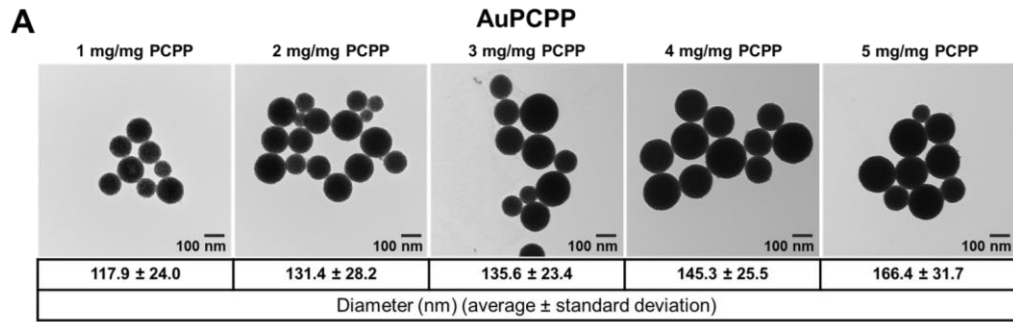


Figure 3.7 TEM of SMNP and PMNP.

TEM of A) AuPCPP, B) TaPCPP, C) CePCPP, and D) PMNP with various loadings of core nanoparticles. E) TEM of overloaded PMNP, TaPCPP, and CePCPP formulations. Scale bar = 100 nm.

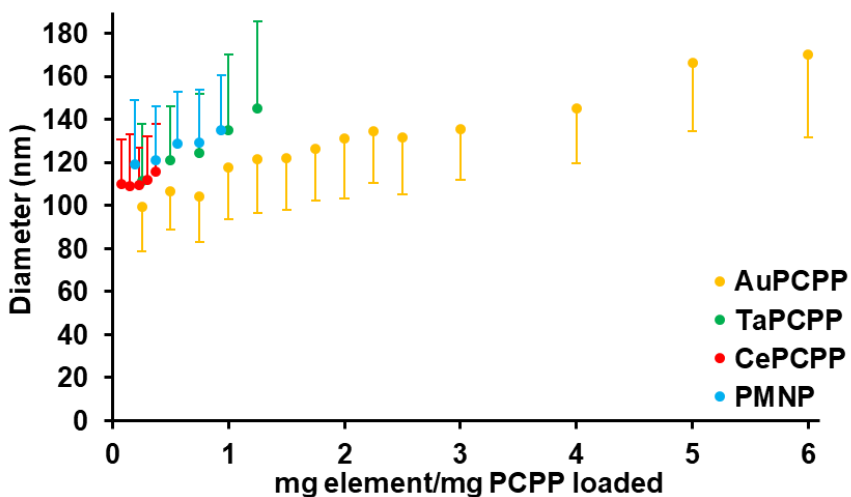


Figure 3.8 Payload-dependent increase of diameters.

Payload dependent increase of SMNP and PMNP in diameter. The one-side error bar represents a standard deviation of the corresponding diameter.

Although the ratio of incorporated payloads of different elements can be freely adjusted, the PMNP formulations reported herein were synthesized with 1:1:1 mass ratios of gold:tantalum:cerium payloads. To assess the relative ratios of these elements encapsulated in PMNP, their concentrations were analyzed by ICP-OES. As shown in Figure 3.9A, the ratios of elements loaded in PMNP were similar to the input ratios.

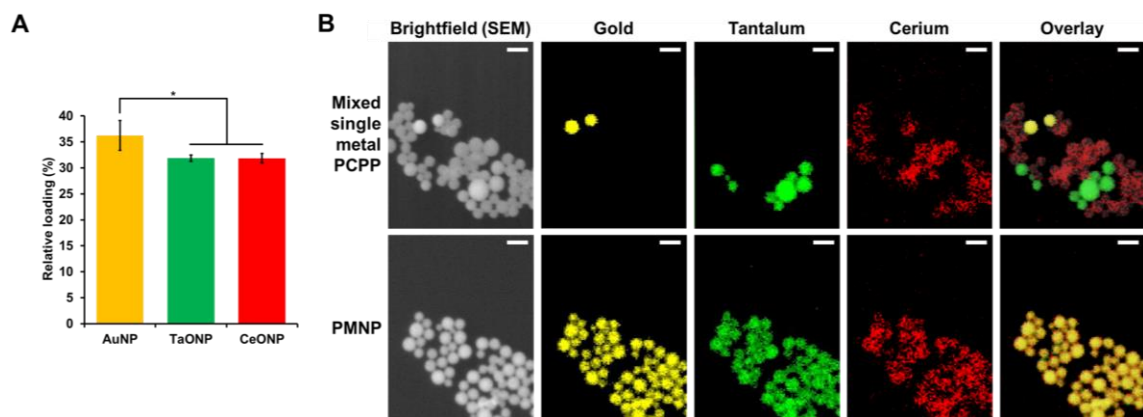


Figure 3.9 Encapsulation of small core nanoparticles in PMNP.

(A) Relative percentages of each payload at maximum loading in PMNP (1 mg Au,Ta,Ce/mg PCPP) ($* = p \leq 0.05$). (B) SEM brightfield images, EDS mappings of gold, tantalum, and cerium, and overlay images. Scale bar = 200 nm.

3.4.4 Spatial distribution of core nanoparticles in polymetal nanoparticles

PMNP was analyzed with EDS mapping to further investigate the encapsulation of all three elements and to examine the spatial distribution of these elements in individual PMNP. To ensure the accuracy of elemental mapping, we used a mixed population of SMNP as a control. As seen in Figure 3.9B, SMNP loaded with either gold, tantalum, or cerium could be successfully differentiated from one another in our control group. Each element was located in its corresponding SMNP formulation without any overlap, allowing us to identify the loading element in each SMNP accurately. On the other hand, for PMNP, all three elements were detected in every PCPP nanoparticle. The elemental maps were colocalized to the location of PCPP nanoparticles in the brightfield image in both groups as well. These data suggest successful co-encapsulation of all three small core nanoparticles into each individual PMNP.

3.4.5 Size control of polymetal nanoparticles

As demonstrated in Figure 3.10, the size of PMNP (0.5 mg Au,Ta,Ce/mg PCPP) could be controlled in the range of 50–450 nm by varying the amount of PEG-PLL used during the synthesis from 0 to 0.2 mg per mg of PCPP. The average diameter of PMNP decreased with increasing amounts of PEG-PLL in a nonlinear manner. This is due to the fact that addition of PEG-PLL limits the growth of PCPP nanoparticles as reported in our previous study with non-loaded PCPP nanoparticles.³⁵

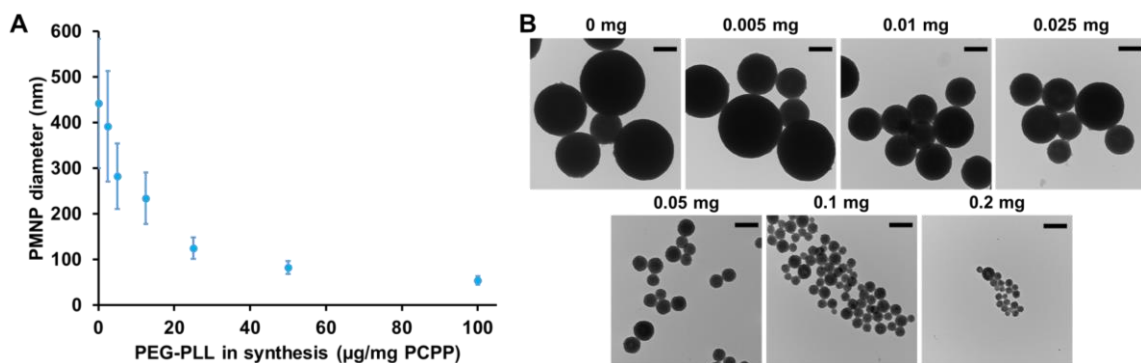


Figure 3.10 Relationship between size of PMNP and amount of PEG-PLL during synthesis.

(A) Effect of PEG-PLL on PMNP diameter. (B) TEM of PMNP of different sizes. Scale bar = 200 nm.

3.4.6 *In vitro* biodegradability

For eventual excretion of PMNP, the small core nanoparticles in PMNP would need to be released from their polymeric components effectively. We therefore evaluated the release rate of the core nanoparticles by incubating PMNP in 10% fetal bovine serum in PBS at 37 °C for 1, 2, 4, and 7 days. The PMNP solution was constantly flowed through a tubing during the incubation periods to mimic the dynamic nature of blood and interstitial

fluid. We observed that approximately 90% of AuNP, TaONP, and CeONP was released from PMNP in 7 days, demonstrating the degradability of PMNP and the effective release of its core nanoparticles (Figure 3.11A). Unlike SMNP formulations that showed clear differences in the release pattern of their core nanoparticles (Figure 3.11B), the release rates of the three core nanoparticle formulations in PMNP were comparable to each other, indicated by much smaller statistical differences throughout the study period. More rapid release of CeONP from CePCPP can be explained by the smaller hydrodynamic diameter of CeONP and possibly their strong negative surface charge. TEM of partially degraded PMNP confirmed the dissociation and the release of core nanoparticles from PMNP (Figure 3.11C).

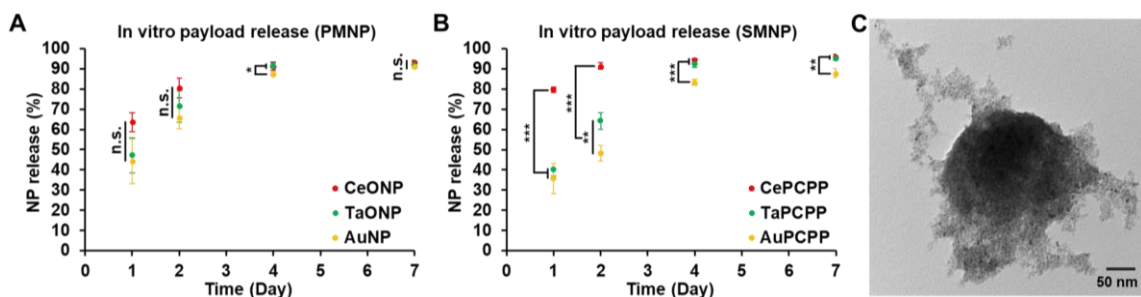


Figure 3.11 Release of small core nanoparticles from PMNP *in vitro*.

Payload release from (A) PMNP and (B) SMNP. (C) TEM of partially degraded PMNP after 4 days of dynamic incubation (n.s. = not significant or $p > 0.05$, * = $p \leq 0.05$, ** = $p \leq 0.01$, *** = $p \leq 0.001$).

3.4.7 *In vitro* cytocompatibility of polymetal nanoparticles

The safety and cytotoxicity of PMNP as well as of AuPCPP, TaPCPP, and CePCPP were evaluated using the same method used to assess the safety and cytotoxicity of the small core nanoparticles (Figure 3.12A,B). Once again, incubation of

the selected cell lines with PMNP and SMNP formulations for 8 h did not considerably affect cell *viability* when compared to the control groups (0 mg/mL). The lowest mean cell *viability* observed from PMNP incubation was $96 \pm 2\%$ in Renca cell line at a treatment concentration of 1 mg Au,Ta,Ce/mL. The results of high cell *viability* from both small core nanoparticles and PCPP formulations suggest that PCPP polymer and its byproducts do not have significant cytotoxicity, which agrees with the previous findings.³⁵⁻³⁷

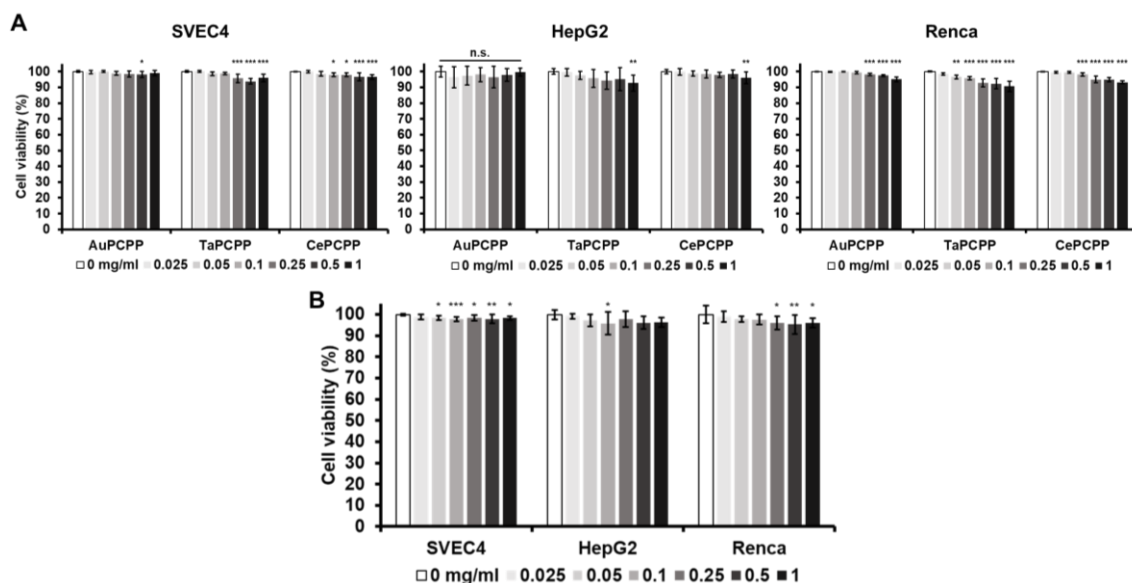


Figure 3.12 Cell *viability* after SMNP and PMNP treatment.

Effect of (A) SMNP and (B) PMNP on cell *viability* after 8 hrs of incubation (n.s. = not significant or $p > 0.05$, * = $p \leq 0.05$, ** = $p \leq 0.01$, *** = $p \leq 0.001$ as compared to the control group (0 mg/mL)).

3.4.8 *In vitro* CT contrast generation

We next assessed PMNP's CT contrast properties using both a μ CT scanner and a clinical CT scanner. A MILabs μ CT scanner with a tube voltage of 50 kVp was used to scan both SMNP and PMNP of increasing element concentration (e.g., gold in AuPCPP

and gold, cerium, and tantalum combined in PMNP) (Figure 3.13A,B). All of the formulations had linear correlations between the attenuation and the concentration with R^2 values >0.99 in each case (the data for PMNP are shown in as an example in Figure 3.13C). From the attenuation rate measurements, we found that PMNP and AuPCPP had the highest values, followed by TaPCPP and CePCPP. The attenuation rate of PMNP was not statistically significantly different from that of AuPCPP (Figure 3.13D).

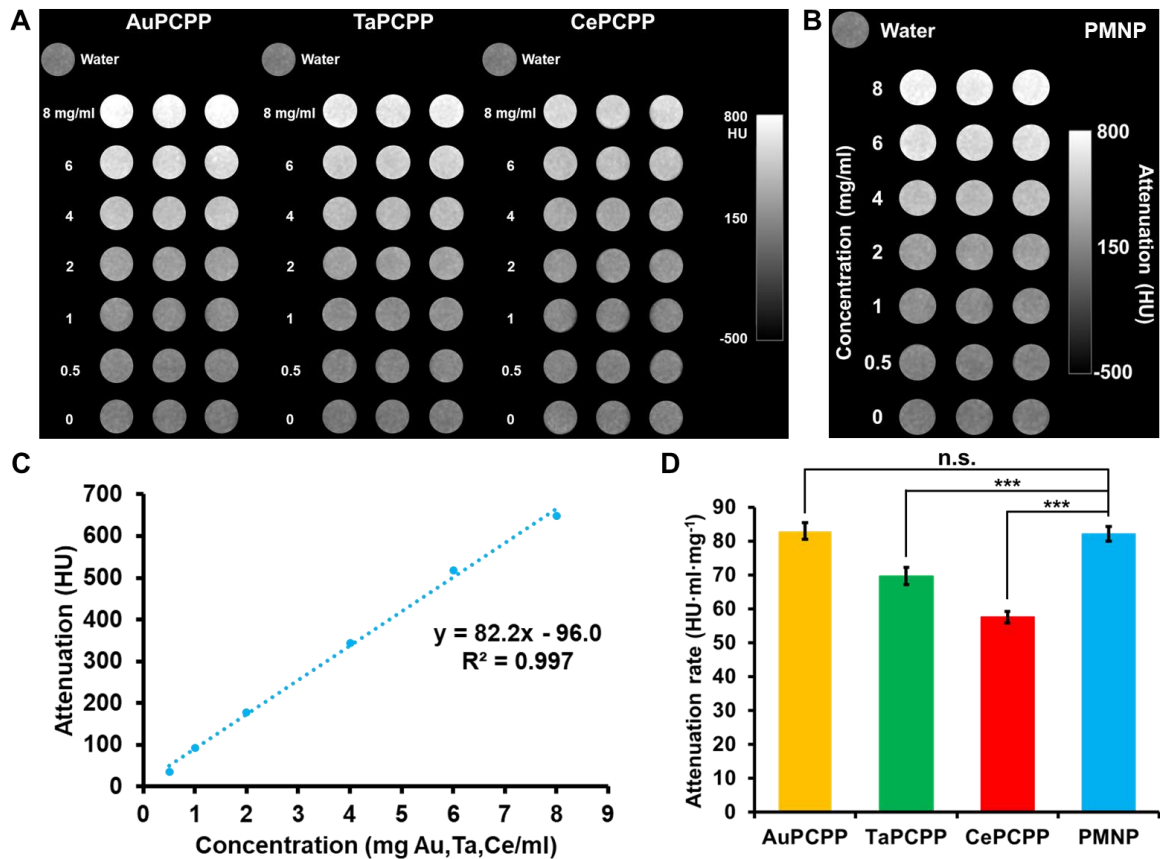


Figure 3.13 *In vitro* contrast generation of PMNP and SMNP in μ CT imaging.

Phantom images of (A) SMNP and (B) PMNP from a MILabs μ CT system. (C) Attenuation of PMNP at a range of concentrations. (D) Attenuation rates of different PCPP formulations (n.s. = not significant or $p > 0.05$, *** = $p \leq 0.001$).

The same PCPP formulations were scanned in a SOMATOM Force clinical CT scanner at four different tube voltages of 80, 100, 120, and 140 kVp. The solutions were scanned in an anthropomorphic phantom body that closely mimics the thorax of a patient (20 cm × 30 cm × 20 cm) to improve the clinical relevance of the data. An axial plane image of the phantom body containing SMNP and PMNP solutions at a tube voltage of 120 kVp is shown in Figure 3.14A and B, in which the increase in attenuation is clearly observed with increasing concentration of the payload. In validation of the images, an excellent linear correlation between the attenuation and the concentration was observed (Figure 3.14C). As expected, we observed that the attenuation rates of both SMNP and PMNP depended heavily on the tube voltage (Figure 3.14D).

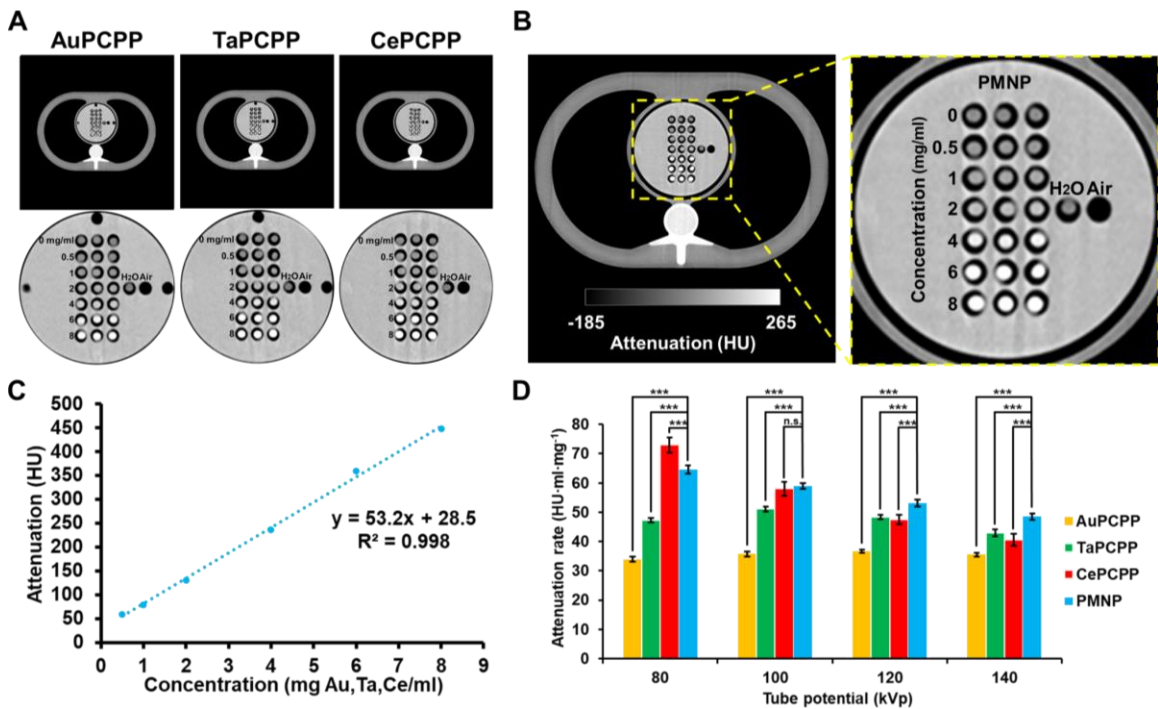


Figure 3.14 *In vitro* contrast generation of PMNP and SMNP in clinical CT imaging.

Phantom images (A) SMNP and (B) PMNP samples from a SOMATOM Force CT scanner and enlarged images centered at the PCPP samples. (C) Attenuation of PMNP at a range of concentrations. (D) Attenuation rates of different PCPP formulations at different tube voltage settings derived from a clinical CT scanner (n.s. = not significant or $p > 0.05$, *** = $p \leq 0.001$).

The attenuation rates of AuPCPP were the lowest across all four tube voltages in this study and the attenuation rates of TaPCPP remained higher than those of AuPCPP across all tube voltages. TaPCPP's attenuation rate slightly increased from 80 to 100 kVp before decreasing again at higher tube voltages of 120 and 140 kVp. Unlike AuPCPP and TaPCPP, a steep decrease in attenuation rate was observed for CePCPP with increasing tube voltage. Its attenuation rate was the highest at 80 kVp; however, due to cerium's comparatively low K-edge energy of 40.4 keV, its attenuation rate sharply decreased to lower than that of TaPCPP at 140 kVp. Interestingly, PMNP also exhibited a decline in attenuation rate with increasing tube voltage. However, the rate of decline was much lower than that of CePCPP, which resulted in its attenuation rate being the second highest after CePCPP at 80 kVp to the highest in both 120 and 140 kVp. Similar trends were observed when attenuation rates were calculated on the basis of molar concentration of the PCPP formulations. Notably, the attenuation rates of PMNP were higher than those of other formulations across all tube voltages used in our study with the exception of TaPCPP at 120 kVp (Figure 3.15).

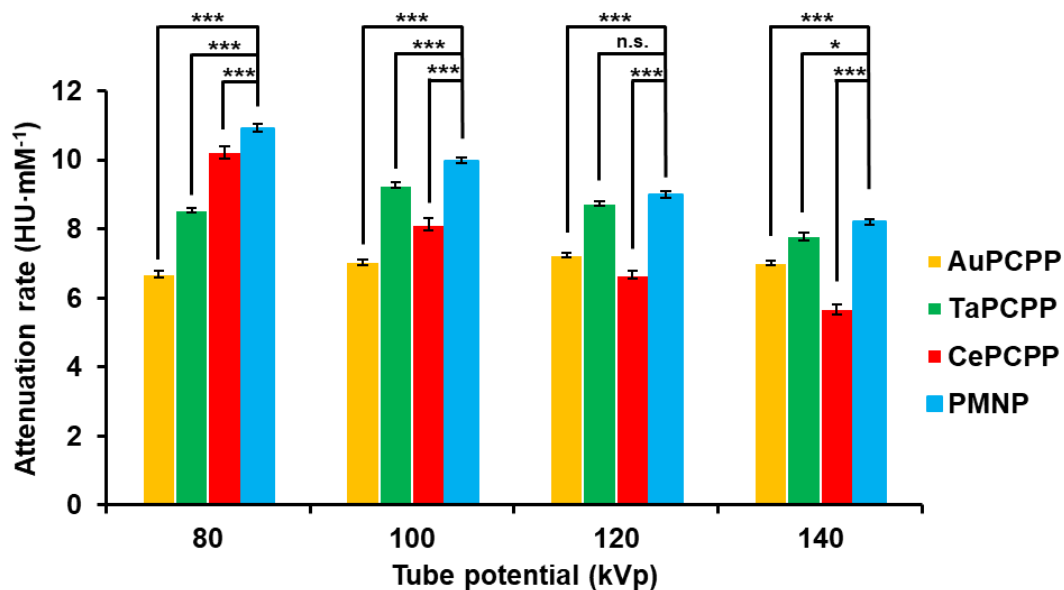


Figure 3.15 CT contrast properties of PCPP formulations.

Attenuation rates of different PCPP formulations derived from a SOMATOM Force CT scanner based on molar concentration (n.s. = not significant or $p > 0.05$, * = $p < 0.05$, ** = $p \leq 0.01$, *** = $p < 0.001$).

3.4.9 Relative contribution to CT attenuation

Using NIST attenuation coefficients of payload elements and X-ray source energy spectra, we calculated the attenuation that was produced by each payload element in PMNP. The relative attenuation contributions from each payload elements were comparable to the differences in attenuation rates between SMNP formulations in our phantom imaging study (Figure 3.16). Attenuation from gold was the largest followed by tantalum and cerium, respectively, in 50 kVp for μ CT imaging simulation. The relative attenuation ratio of cerium decreased and those of gold and tantalum slowly increased as the tube potential increased in clinical CT imaging simulation. Interestingly, the relative ratios of contribution

between gold and tantalum were very similar to one another across all tube potentials used in this study.

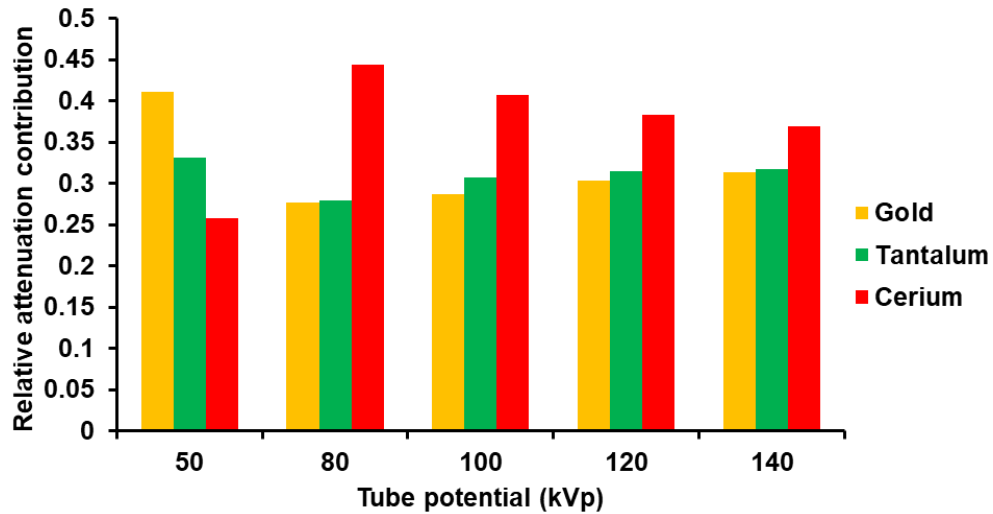


Figure 3.16 Relative attenuation contribution of gold, tantalum, and cerium to PMNP.

Simulated relative contribution from gold, tantalum, and cerium to PMNP's CT attenuation at 8 mg/ml in payload element concentration from μ CT and clinical CT imaging with various tube potential settings used in this study.

3.4.10 *In vivo* contrast generation

In vivo contrast properties of PMNP were assessed by imaging mice that were intramuscularly injected with the same dose and volume (0.1 mg, 40 μ L) of either PMNP or AuPCPP - two formulations that showed the highest attenuation rates in μ CT phantom imaging. As shown in Figure 3.17A–C, ROI of contrast agents surrounding the injection site were isolated and highlighted in both 2D and 3D images, which was possible due to production of strong CT contrast by these contrast agents. The highlighted area could also be accurately depicted in 3D isocontour mapping for better visualization of its volume (Figure 3.17D). To quantify and compare the contrast generation by PMNP and AuPCPP,

total attenuation (summation of CT attenuation values in each voxel) of the isolated 3D ROI was measured. In agreement with our findings in μ CT phantom imaging, the total attenuation generated by PMNP had no statistically significant difference from the total attenuation measurement of AuPCPP (Figure 3.17E).

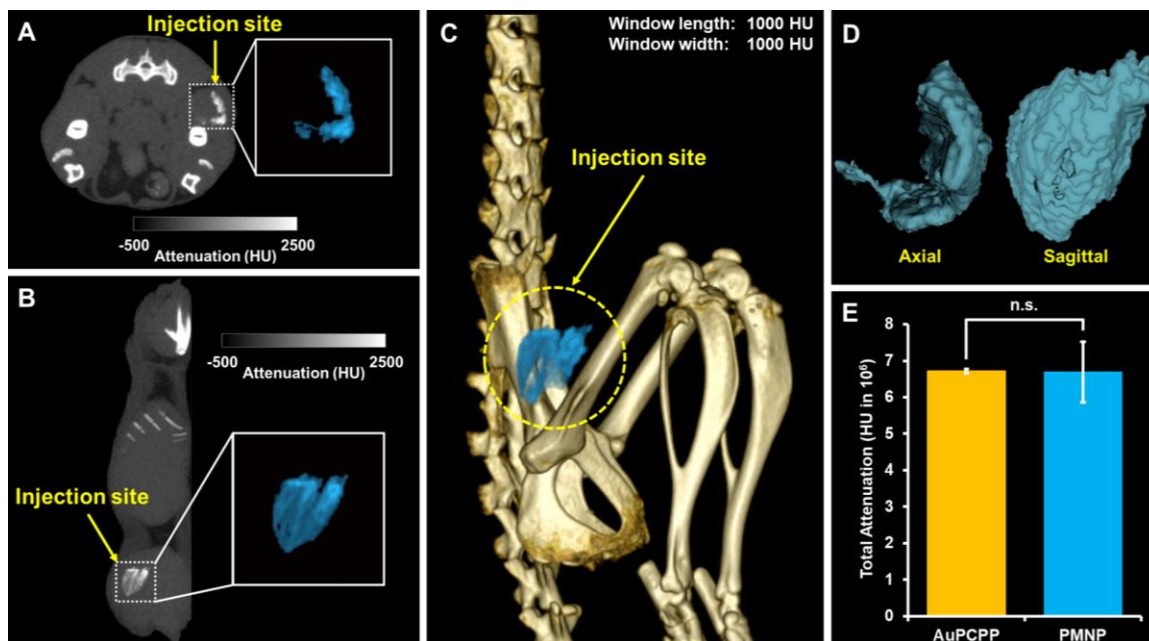


Figure 3.17 *In vivo* images and contrast generation analysis.

CT images of PMNP injected in the thigh muscle viewed in the (A) axial plane and the (B) sagittal plane. Insets represent enlarged images of injected PMNP highlighted in light blue. (C) 3D rendered CT image of a mouse with the PMNP injection site highlighted in light blue. (D) Isocontour depiction of injected PMNP in both axial and sagittal views. (E) Image analysis of the attenuation arising from nanoparticle injections (n.s. = not significant).

3.5 Discussion

In this study, by encapsulating small core nanoparticles made of three different elements (gold, tantalum, and cerium) in PCPP polymer, we developed biodegradable

polymetal nanoparticles that can generate high CT contrast at various tube voltage settings used in both μ CT and clinical CT scanners. Our phantom and *in vivo* mice imaging study results both support that contrast agents made of several elements with suitable K-edge energies can generate consistently high attenuation in CT imaging of various X-ray source spectra, similar to the effects observed in radioprotective garments. In fact, our PMNP formulation generated significantly higher attenuation than well-studied experimental CT contrast payload materials, such as gold and tantalum alone, in different tube potential settings used in this study. The attenuation rates of PMNP observed in our study are also much higher than those of iodinated contrast agents (i.e., iopamidol) reported by Hsu et al.,³⁸ who acquired the data with the identical CT scanner, tube voltage, and other scanning parameters. The high attenuation generation of our PMNP formulation throughout low and high tube voltage settings can offer an advantage over the use of payload elements of low K-edge energies, such as cerium and iodine, in numerous CT imaging applications. These low K-edge energies suffer from deterioration of attenuation generation at high tube voltage (e.g., 140 kVp).³⁹ This indicates that our PMNP formulation can especially be beneficial in CT imaging of obese patients, a rapidly growing patient pool,⁴⁰ which often requires imaging at high tube voltage.^{41,42} Most studies of novel CT contrast agent development focus on either small molecules or nanoparticles made of single element payloads. However, the observations made in this study indicate that the development of CT contrast agents with two or more CT payload elements can potentially improve their CT contrast properties. Future investigation of the amount, ratio, and identification of different payload elements (e.g., gadolinium and ytterbium) will further enhance the CT contrast properties of PMNP. As shown in our simulation, ideal ratios and

choices of payload elements can be predicted with sufficient accuracy to make PMNP suitable for user-specific CT imaging applications.

In our design of PMNP, we have loaded the hydrophilic core nanoparticles in PCPP polymers. However, various kinds of platforms capable of serving as carriers for multiple contrast generating materials are available. These platforms include micelles, liposomes, nano- and micro-emulsions, dendrimers, lipoproteins, and other polymeric nanoparticles (e.g., PLGA, alginate), all of which have previously been demonstrated to be effective carriers of contrast payloads.⁴³⁻⁴⁸ Many of these platforms, such as liposomes and lipoproteins, are also capable of containing both hydrophilic and hydrophobic payloads, further expanding the choices of payload materials for the synthesis of polymetal nanoparticles.

Our previous studies have loaded small gold nanoparticles in PCPP nanoparticles.^{35,49} However, this study was the first attempt to include core nanoparticles of three different elements. This new formulation can lead to increased affordability as compared to other leading experimental CT contrast agents (e.g., AuNP), reduced dose-related cytotoxicity, and most importantly, improved CT attenuation production. As mentioned above, the potential for PMNP to be a contrast agent with excellent CT contrast properties has been demonstrated; however, more work is still needed to develop PMNP into a blood pool agent with desired pharmacokinetics and sufficient excretion of its payloads. The possibility of achieving sufficient excretion is promising, considering the versatility of PCPP-based nanoparticles. By adjusting the amount of PEG-PLL added, the diameter of PMNP could be controlled. The side-chain groups and the molecular weight of PCPP can also be readily adjusted, allowing us to control PMNP's degradation rate and its diameter at ease.⁵⁰ Other components of the synthesis (e.g., cross-linker) can be

changed as well. For instance, spermine (polyamine with four amine groups) can be replaced with alternative polypeptides with less cationic properties for faster degradation. To ensure the feasibility of its use as a safe CT blood pool agent, more extensive studies on long-term cytotoxicity of PMNP will need to be done. Its plausibility for successful injection in human patients will also need to be investigated in the future. Sufficiently high concentration of PMNP could easily be reached for *in vivo* mice injection in our study, but hundreds of mg/mL in payload concentration will be needed for human subject injection. While this is possible, the viscosity and osmolarity of PMNP solutions at these levels of concentrations will need to be assessed. Finding gold, tantalum, and cerium nanoparticle formulations that are coated with surface ligands that result in higher payloads PCPP nanoparticles (i.e., hydrophilic, anionic) will be crucial, as it will decrease the amount of polymer needed in the formulation and subsequently decrease the viscosity.

Widely studied experimental CT contrast agents, such as AuNP, have also been utilized as an X-ray radiosensitizer due to their large X-ray interaction cross section, leading to better energy and radiation deposition for effective induction of local tumor cell death.^{51,52} PMNP's ability to produce higher CT attenuation in various tube voltage settings in the keV region supports the idea that PMNP can potentially be more effective in energy deposition, and therefore can act as a better radiosensitizer than AuNP. Potential use of PMNP is not limited to CT and X-ray based biomedical applications. The payload materials of multiple imaging modalities (e.g., quantum dots for fluorescence imaging and iron oxide nanoparticles for MR imaging) can be loaded in PMNP for multimodal imaging; hydrophilic drugs can be co-loaded with contrast agents for theranostics.

3.6 Conclusion

In summary, we developed a unique design of polymetal nanoparticles by encapsulating hydrophilic, small core metal nanoparticles that are made from three different contrast generating elements - gold, tantalum, and cerium - in PCPP polymer carriers. PMNP demonstrated efficient loading of hydrophilic payloads, encapsulating up to 1 mg of contrast generating materials per mg of PCPP polymer while maintaining its structural stability, biocompatibility, and biodegradability. We have also shown that the PMNP formulation is a robust CT contrast agent that can generate higher attenuation in both μ CT and clinical CT imaging in various scanning conditions, when compared to its single payload counterparts. Our promising results in the contrast properties of PMNP suggest that the development of platforms carrying multiple contrast generating materials can further improve CT contrast, and therefore can benefit CT imaging in various biomedical applications.

3.7 References

1. Cole, L. E.; Ross, R. D.; Tilley, J. M.; Vargo-Gogola, T.; Roeder, R. K., Gold nanoparticles as contrast agents in x-ray imaging and computed tomography. *Nanomedicine (Lond)* **2015**, *10* (2), 321-341.
2. McGinnity, T. L.; Dominguez, O.; Curtis, T. E.; Nallathamby, P. D.; Hoffman, A. J.; Roeder, R. K., Hafnia (HfO₂) nanoparticles as an X-ray contrast agent and mid-infrared biosensor. *Nanoscale* **2016**, *8* (28), 13627-13637.
3. Hernandez-Rivera, M.; Kumar, I.; Cho, S. Y.; Cheong, B. Y.; Pulikkathara, M. X.; Moghaddam, S. E.; Whitmire, K. H.; Wilson, L. J., High-performance hybrid bismuth-carbon nanotube based contrast agent for X-ray CT imaging. *ACS Appl Mater Interfaces* **2017**, *9* (7), 5709-5716.
4. Oh, M. H.; Lee, N.; Kim, H.; Park, S. P.; Piao, Y.; Lee, J.; Jun, S. W.; Moon, W. K.; Choi, S. H.; Hyeon, T., Large-scale synthesis of bioinert tantalum oxide nanoparticles for X-ray computed tomography imaging and bimodal image-guided sentinel lymph node mapping. *J Am Chem Soc* **2011**, *133* (14), 5508-5515.
5. Cormode, D. P.; Naha, P. C.; Fayad, Z. A., Nanoparticle contrast agents for computed tomography: a focus on micelles. *Contrast Media Mol Imaging* **2014**, *9* (1), 37-52.
6. Lee, N.; Choi, S. H.; Hyeon, T., Nano-sized CT contrast agents. *Adv Mater* **2013**, *25* (19), 2641-2660.
7. Liu, Y.; Liu, J.; Ai, K.; Yuan, Q.; Lu, L., Recent advances in ytterbium-based contrast agents for *in vivo* X-ray computed tomography imaging: promises and prospects. *Contrast Media Mol Imaging* **2014**, *9* (1), 26-36.

8. Stacul, F.; van der Molen, A. J.; Reimer, P.; Webb, J. A.; Thomsen, H. S.; Morcos, S. K.; Almen, T.; Aspelin, P.; Bellin, M. F.; Clement, O.; Heinz-Peer, G., Contrast induced nephropathy: updated ESUR contrast media safety committee guidelines. *Eur Radiol* **2011**, *21* (12), 2527-2541.
9. Mehran, R.; Dangas, G. D.; Weisbord, S. D., Contrast-associated acute kidney injury. *N Engl J Med* **2019**, *380* (22), 2146-2155.
10. Faucon, A. L.; Bobrie, G.; Clement, O., Nephrotoxicity of iodinated contrast media: From pathophysiology to prevention strategies. *Eur J Radiol* **2019**, *116*, 231-241.
11. Damman, K.; Testani, J. M., The kidney in heart failure: an update. *Eur Heart J* **2015**, *36* (23), 1437-1444.
12. Yeh, B. M.; FitzGerald, P. F.; Edic, P. M.; Lambert, J. W.; Colborn, R. E.; Marino, M. E.; Evans, P. M.; Roberts, J. C.; Wang, Z. J.; Wong, M. J.; Bonitatibus, P. J., Jr., Opportunities for new CT contrast agents to maximize the diagnostic potential of emerging spectral CT technologies. *Adv Drug Deliv Rev* **2017**, *113*, 201-222.
13. Mieszawska, A. J.; Mulder, W. J.; Fayad, Z. A.; Cormode, D. P., Multifunctional gold nanoparticles for diagnosis and therapy of disease. *Mol Pharm* **2013**, *10* (3), 831-847.
14. Ahmad, M. W.; Xu, W.; Kim, S. J.; Baeck, J. S.; Chang, Y.; Bae, J. E.; Chae, K. S.; Park, J. A.; Kim, T. J.; Lee, G. H., Potential dual imaging nanoparticle: Gd₂O₃ nanoparticle. *Sci Rep* **2015**, *5*, 8549.
15. Al Zaki, A.; Joh, D.; Cheng, Z.; De Barros, A. L.; Kao, G.; Dorsey, J.; Tsourkas, A., Gold-loaded polymeric micelles for computed tomography-guided radiation therapy treatment and radiosensitization. *ACS Nano* **2014**, *8* (1), 104-112.

16. Bonitatibus, P. J., Jr.; Torres, A. S.; Kandapallil, B.; Lee, B. D.; Goddard, G. D.; Colborn, R. E.; Marino, M. E., Preclinical assessment of a zwitterionic tantalum oxide nanoparticle X-ray contrast agent. *ACS Nano* **2012**, *6* (8), 6650-6658.
17. Chhour, P.; Naha, P. C.; O'Neill, S. M.; Litt, H. I.; Reilly, M. P.; Ferrari, V. A.; Cormode, D. P., Labeling monocytes with gold nanoparticles to track their recruitment in atherosclerosis with computed tomography. *Biomaterials* **2016**, *87*, 93-103.
18. Liu, Z.; Li, Z.; Liu, J.; Gu, S.; Yuan, Q.; Ren, J.; Qu, X., Long-circulating Er³⁺-doped Yb₂O₃ up-conversion nanoparticle as an *in vivo* X-Ray CT imaging contrast agent. *Biomaterials* **2012**, *33* (28), 6748-6757.
19. Rabin, O.; Manuel Perez, J.; Grimm, J.; Wojtkiewicz, G.; Weissleder, R., An X-ray computed tomography imaging agent based on long-circulating bismuth sulphide nanoparticles. *Nat Mater* **2006**, *5* (2), 118-122.
20. Kim, J.; Chhour, P.; Hsu, J.; Litt, H. I.; Ferrari, V. A.; Popovtzer, R.; Cormode, D. P., Use of nanoparticle contrast agents for cell tracking with computed tomography. *Bioconjug Chem* **2017**, *28* (6), 1581-1597.
21. Meir, R.; Popovtzer, R., Cell tracking using gold nanoparticles and computed tomography imaging. *Wiley Interdiscip Rev Nanomed Nanobiotechnol* **2018**, *10* (2).
22. Bonitatibus, P. J., Jr.; Torres, A. S.; Goddard, G. D.; FitzGerald, P. F.; Kulkarni, A. M., Synthesis, characterization, and computed tomography imaging of a tantalum oxide nanoparticle imaging agent. *Chem Commun (Camb)* **2010**, *46* (47), 8956-8958.
23. Kim, J.; Bar-Ness, D.; Si-Mohamed, S.; Coulon, P.; Blevis, I.; Douek, P.; Cormode, D. P., Assessment of candidate elements for development of spectral photon-counting CT specific contrast agents. *Sci Rep* **2018**, *8* (1), 12119.

24. Riederer, I.; Bar-Ness, D.; Kimm, M. A.; Si-Mohamed, S.; Noel, P. B.; Rummeny, E. J.; Douek, P.; Pfeiffer, D., Liquid embolic agents in spectral X-Ray photon-counting computed tomography using tantalum K-edge imaging. *Sci Rep* **2019**, *9* (1), 5268.
25. Das, S.; Dowding, J. M.; Klump, K. E.; McGinnis, J. F.; Self, W.; Seal, S., Cerium oxide nanoparticles: applications and prospects in nanomedicine. *Nanomedicine (Lond)* **2013**, *8* (9), 1483-1508.
26. Pirmohamed, T.; Dowding, J. M.; Singh, S.; Wasserman, B.; Heckert, E.; Karakoti, A. S.; King, J. E.; Seal, S.; Self, W. T., Nanoceria exhibit redox state-dependent catalase mimetic activity. *Chem Commun (Camb)* **2010**, *46* (16), 2736-2738.
27. Walkey, C.; Das, S.; Seal, S.; Erlichman, J.; Heckman, K.; Ghibelli, L.; Traversa, E.; McGinnis, J. F.; Self, W. T., Catalytic properties and biomedical applications of cerium oxide nanoparticles. *Environ Sci Nano* **2015**, *2* (1), 33-53.
28. Kazempour, M.; Saeedimoghadam, M.; Shekoohi Shooli, F.; Shokrpour, N., Assessment of the radiation attenuation properties of several lead free composites by monte carlo simulation. *J Biomed Phys Eng* **2015**, *5* (2), 67-76.
29. Livingstone, R. S.; Varghese, A.; Keshava, S. N., A study on the use of radiation-protective apron among interventionists in radiology. *J Clin Imaging Sci* **2018**, *8*, 34.
30. Andrianov, A. K.; Marin, A.; Martinez, A. P.; Weidman, J. L.; Fuerst, T. R., Hydrolytically degradable PEGylated polyelectrolyte nanocomplexes for protein delivery. *Biomacromolecules* **2018**, *19* (8), 3467-3478.
31. Martinez, A. P.; Qamar, B.; Fuerst, T. R.; Muro, S.; Andrianov, A. K., Biodegradable "smart" polyphosphazenes with intrinsic multifunctionality as intracellular protein delivery vehicles. *Biomacromolecules* **2017**, *18* (6), 2000-2011.

32. Nukavarapu, S. P.; Kumbar, S. G.; Brown, J. L.; Krogman, N. R.; Weikel, A. L.; Hindenlang, M. D.; Nair, L. S.; Allcock, H. R.; Laurencin, C. T., Polyphosphazene/nano-hydroxyapatite composite microsphere scaffolds for bone tissue engineering. *Biomacromolecules* **2008**, *9* (7), 1818-1825.
33. Kumbar, S. G.; Bhattacharyya, S.; Nukavarapu, S. P.; Khan, Y. M.; Nair, L. S.; Laurencin, C. T., *In vitro* and *in vivo* characterization of biodegradable poly(organophosphazenes) for biomedical applications. *J Inorg Organomet Polym Mater* **2007**, *16*, 365-385.
34. Asati, A.; Santra, S.; Kaittanis, C.; Nath, S.; Perez, J. M., Oxidase-like activity of polymer-coated cerium oxide nanoparticles. *Angew Chem Int Ed Engl* **2009**, *48* (13), 2308-2312.
35. Cheheltani, R.; Ezzibdeh, R. M.; Chhour, P.; Pulaparthy, K.; Kim, J.; Jurcova, M.; Hsu, J. C.; Blundell, C.; Litt, H. I.; Ferrari, V. A.; Allcock, H. R.; Sehgal, C. M.; Cormode, D. P., Tunable, biodegradable gold nanoparticles as contrast agents for computed tomography and photoacoustic imaging. *Biomaterials* **2016**, *102*, 87-97.
36. Bouche, M.; Puhlinger, M.; Iturmendi, A.; Amirshaghghi, A.; Tsourkas, A.; Teasdale, I.; Cormode, D. P., Activatable hybrid polyphosphazene-AuNP nanoprobe for ROS detection by bimodal PA/CT imaging. *ACS Appl Mater Interfaces* **2019**, *11* (32), 28648-28656.
37. Sethuraman, S.; Nair, L. S.; El-Amin, S.; Farrar, R.; Nguyen, M. T.; Singh, A.; Allcock, H. R.; Greish, Y. E.; Brown, P. W.; Laurencin, C. T., *In vivo* biodegradability and biocompatibility evaluation of novel alanine ester based polyphosphazenes in a rat model. *J Biomed Mater Res A* **2006**, *77* (4), 679-687.

38. Hsu, J. C.; Naha, P. C.; Lau, K. C.; Chhour, P.; Hastings, R.; Moon, B. F.; Stein, J. M.; Witschey, W. R. T.; McDonald, E. S.; Maidment, A. D. A.; Cormode, D. P., An all-in-one nanoparticle (AION) contrast agent for breast cancer screening with DEM-CT-MRI-NIRF imaging. *Nanoscale* **2018**, *10* (36), 17236-17248.
39. Galper, M. W.; Saung, M. T.; Fuster, V.; Roessler, E.; Thran, A.; Proksa, R.; Fayad, Z. A.; Cormode, D. P., Effect of computed tomography scanning parameters on gold nanoparticle and iodine contrast. *Invest Radiol* **2012**, *47* (8), 475-481.
40. Finkelstein, E. A.; Khavjou, O. A.; Thompson, H.; Trogdon, J. G.; Pan, L.; Sherry, B.; Dietz, W., Obesity and severe obesity forecasts through 2030. *Am J Prev Med* **2012**, *42* (6), 563-570.
41. Chen, H.; Danielsson, M.; Xu, C., Size-dependent scanning parameters (kVp and mAs) for photon-counting spectral CT system in pediatric imaging: simulation study. *Phys Med Biol* **2016**, *61* (11), 4105-4126.
42. Modica, M. J.; Kanal, K. M.; Gunn, M. L., The obese emergency patient: imaging challenges and solutions. *Radiographics* **2011**, *31* (3), 811-823.
43. Cormode, D. P.; Roessler, E.; Thran, A.; Skajaa, T.; Gordon, R. E.; Schlomka, J. P.; Fuster, V.; Fisher, E. A.; Mulder, W. J.; Proksa, R.; Fayad, Z. A., Atherosclerotic plaque composition: analysis with multicolor CT and targeted gold nanoparticles. *Radiology* **2010**, *256* (3), 774-782.
44. Geng, J.; Li, K.; Pu, K. Y.; Ding, D.; Liu, B., Conjugated polymer and gold nanoparticle co-loaded PLGA nanocomposites with eccentric internal nanostructure for dual-modal targeted cellular imaging. *Small* **2012**, *8* (15), 2421-2429.

45. Hua, H.; Zhang, N.; Liu, D.; Song, L.; Liu, T.; Li, S.; Zhao, Y., Multifunctional gold nanorods and docetaxel-encapsulated liposomes for combined thermo- and chemotherapy. *Int J Nanomedicine* **2017**, *12*, 7869-7884.
46. Huang, C. H.; Nwe, K.; Al Zaki, A.; Brechbiel, M. W.; Tsourkas, A., Biodegradable polydisulfide dendrimer nanoclusters as MRI contrast agents. *ACS Nano* **2012**, *6* (11), 9416-9424.
47. Kim, J.; Arifin, D. R.; Muja, N.; Kim, T.; Gilad, A. A.; Kim, H.; Arepally, A.; Hyeon, T.; Bulte, J. W., Multifunctional capsule-in-capsules for immunoprotection and trimodal imaging. *Angew Chem Int Ed Engl* **2011**, *50* (10), 2317-2321.
48. Pan, D.; Roessl, E.; Schlomka, J. P.; Caruthers, S. D.; Senpan, A.; Scott, M. J.; Allen, J. S.; Zhang, H.; Hu, G.; Gaffney, P. J.; Choi, E. T.; Rasche, V.; Wickline, S. A.; Proksa, R.; Lanza, G. M., Computed tomography in color: NanoK-enhanced spectral CT molecular imaging. *Angew Chem Int Ed Engl* **2010**, *49* (50), 9635-9639.
49. Chhour, P.; Gallo, N.; Cheheltani, R.; Williams, D.; Al-Zaki, A.; Paik, T.; Nichol, J. L.; Tian, Z.; Naha, P. C.; Witschey, W. R.; Allcock, H. R.; Murray, C. B.; Tsourkas, A.; Cormode, D. P., Nanodisco balls: control over surface versus core loading of diagnostically active nanocrystals into polymer nanoparticles. *ACS Nano* **2014**, *8* (9), 9143-9153.
50. Allcock, H. R., Recent developments in polyphosphazene materials science. *Curr Opin Solid State Mater Sci* **2006**, *10* (5), 231-240.
51. Haume, K.; Rosa, S.; Grellet, S.; Smialek, M. A.; Butterworth, K. T.; Solov'yov, A. V.; Prise, K. M.; Golding, J.; Mason, N. J., Gold nanoparticles for cancer radiotherapy: a review. *Cancer Nanotechnol* **2016**, *7* (1), 8.

52. Her, S.; Jaffray, D. A.; Allen, C., Gold nanoparticles for applications in cancer radiotherapy: Mechanisms and recent advancements. *Adv Drug Deliv Rev* **2017**, *109*, 84-101.

CHAPTER 4: CITRIC ACID COATED CERIUM OXIDE NANOPARTICLES FOR DETECTION AND TREATMENT OF INFLAMMATORY DISEASES

4.1 Abstract

Cerium oxide nanoparticles (CeONP), having potent antioxidant properties, are highly promising for treatment of diseases in which oxidative stress from excessive reactive oxygen species (ROS) plays a critical role in the pathogenesis and progression. However, previously reported CeONP formulations were not cleared from the body, precluding their clinical translation. Herein, we report renally clearable ultrasmall CeONP that can mitigate acute inflammation. It was found that these CeONP can effectively scavenge reactive species, inhibit immune cell activation, and minimize their recruitment and infiltration to the inflammation site, which led to alleviation of persistent inflammatory reaction and pain hypersensitivity. Moreover, we demonstrate that CeONP can be effectively excreted from the body within 24 hours of systemic administration, minimizing long-term toxicity concerns. Cerium's appropriate K-edge energy also makes CeONP suitable contrast agents for CT imaging. Therefore, we also investigated the potential use of CeONP as CT contrast agents by performing phantom imaging studies. Altogether, our findings suggest that CeONP can be used as an effective antioxidant and immunomodulatory agent to reduce collateral healthy tissue damage during acute inflammation with an improved safety profile and as a CT contrast agent for disease diagnosis.

4.2 Introduction

ROS is a natural byproduct of oxygen metabolism that is essential for cell signaling; however, production of excess ROS and other free radicals (i.e., reactive nitrogen species or RNS) can have detrimental effects to cells, causing oxidative damage to various cellular components, such as DNA, proteins and lipids, and subsequently leading to cell death and tissue damage.¹ The elevated production of free radicals (e.g., superoxide, hydroxyl radical and nitric oxide) from the imbalance between their production and their elimination by endogenous catalytic mechanisms is defined as oxidative stress.² ³ Oxidative stress is a key contributor in progression of inflammatory diseases as well as acute injury and inflammation.⁴ It is previously found that oxidative stress promotes inflammation by directly activating the genes that are involved in inflammatory pathways (e.g., NF- κ B/AP-1) to induce secretion of proinflammatory cytokines and inhibit tissue remodeling.⁵ Furthermore, inflammatory processes promote ROS production from phagocytic cells (e.g., macrophages and neutrophils), which can cause additional tissue injury and subsequently initiate further immune response and ROS production as a result.^{4, 6} Therefore, restoration of free radical homeostasis *via* antioxidant treatment is a promising therapeutic approach to modulate collateral tissue damage from oxidative stress and inflammation.

An emerging field that can offer a novel treatment option for oxidative stress-related diseases is the development of nanozymes.⁷ Nanozymes are capable of mimicking the catalytic activities of natural enzymes to efficiently scavenge free radicals in their surroundings. An example of a class of nanozyme is CeONP, which are inorganic nanoparticles that have attracted substantial research interest due to their potent and recyclable ROS scavenging activities.⁸⁻¹³ Cerium ions in CeONP can exist in one of two

oxidation states (Ce^{3+} and Ce^{4+}) on the nanoparticle surface; and highly mobile oxygen vacancies in the lattice allow these cerium ions to freely alternate their oxidation states to either lose or gain oxygen atoms in a reversible manner.¹⁴⁻¹⁶ Through this interchange in redox state, each reactive site on CeONP can interact with numerous ROS and convert them to inert molecules. This allows CeONP to have more potent antioxidative activities than traditional antioxidants (e.g., vitamin C and selenium) that are exhausted after interaction with one molecule of reactive species. In addition, the presence of multiple reactive sites on the nanoparticles surfaces further augments the antioxidant properties of CeONP to allow sustained ROS scavenging activity.

CeONP's strong catalytic activity through the redox reaction has already been well-recognized and widely applied in petrochemical and materials industry as fuel cells, oxygen sensors, ultraviolet absorbents, to name a few.¹⁷⁻¹⁹ More recently, CeONP have been increasingly explored for various biomedical applications in treatment of ROS-related diseases, which include, but are not limited to, neurodegenerative diseases,^{20, 21} autoimmune diseases,²² ocular surface diseases,¹³ and ischemic and acute injuries.²³⁻²⁵ Biomedical applications of CeONP is supported by the fact that the afore-mentioned ROS scavenging mechanisms are analogous to biological processes used by endogenous enzymes in our body, such as superoxide dismutase (dismutation of superoxide anion into molecular oxygen and hydrogen peroxide) and catalase (oxidation of hydrogen peroxide to water and oxygen molecules).²⁶⁻²⁸

By designing our CeONP formulation to be ultras-small, we further improved the feasibility of the formulation's use in biomedical applications and eventual clinical translation. The average hydrodynamic diameter of our CeONP formulation (~ 3 nm) is well-below the putative renal filtration threshold of 5.5 nm, promoting efficient renal

clearance and thereby avoiding toxicity concerns that arise from long-term retention in the reticuloendothelial system (e.g., liver and spleen).^{29, 30} The ultrasmall size also raises the surface area-to-volume ratio, which subsequently increases the number of reactive sites per dose of cerium to enhance the efficacy of ROS scavenging per material used. The surface coating used (i.e. citric acid) was also able to provide stability in biological media without interfering the catalytic activities of CeONP.

Cerium, the main elemental composition of CeONP, is a lanthanide heavy metal element that has a favorable K-edge energy for high contrast generation in CT imaging. Its K-edge energy (40.4 keV) is located in a high X-ray photo flux region, resulting in greater CT contrast production when compared to iodine, whose K-edge energy is at 33.2 keV. Cerium's biocompatibility, low cost (especially when compared to gold, which is the most widely studied element for experimental CT contrast agent development), wide availability also make it practical to use on a large scale with high potential for clinical translation. However, despite these advantages, cerium and cerium-based nanoparticles have not been extensively studied as CT contrast agents.

Herein, we demonstrate that citric acid coated CeONP with strong antioxidant properties can alleviate acute inflammation by reducing secretion of pro-inflammatory cytokines and suppressing macrophage recruitment to the inflammation site. Moreover, we investigate the toxicity and renal clearance of the CeONP formulation, which are key parameters to be considered for eventual clinical translation. We also examine CT contrast generation of citric acid coated CeONP to assess their feasibility to be developed as CT contrast agents.

4.3 Materials and methods

4.3.1 Materials

Cerium(III) nitrate hexahydrate (99.99%) and ammonium hydroxide (28.0–30.0% NH₃ basis) were obtained from Sigma-Aldrich. Citric acid anhydrous, superoxide dismutase colorimetric activity kit, Amplex red hydrogen peroxide/peroxidase assay kit, CM-H2DCFDA, Griess reagent kit, mouse TNF alpha and IL-1 beta ELISA kits were purchased from Thermofisher Scientific. Mouse IL-10 ELISA kit was acquired from Abcam. HepG2, RAW 264.7, Renca, SVEC4-10EHR1 cell lines were purchased from ATCC.

4.3.2 Synthesis of citric acid coated CeONP

Ultrasmall citric acid coated CeONP were synthesized by slight modification of an alkaline-based precipitation method that our group has previously reported.³¹ Briefly, a 4 ml solution containing 217 mg of cerium nitrate precursor was mixed with a 2 ml solution containing 200 mg of citric acid. The resulting mixture was quickly added to 100 ml of 0.4 M ammonium hydroxide. After 24 hours of stirring at room temperature, the resulting clear yellow nanoparticle solution was centrifuged at 2600 g for 30 minutes to remove aggregates. The supernatant of the centrifuged solution was further purified by centrifugation in 3 kDa molecular weight cutoff tubes. This purification step was repeated 5 times by resuspending the concentrated solution in deionized water to remove any unreacted chemicals. The resulting nanoparticle solution was ultra-centrifuged at 15000 g for 10 minutes and was subsequently filtered through a 0.02 µm syringe filter. The final nanoparticle solution was suspended in either deionized water or PBS for further studies.

4.3.3 Nanoparticle characterization

The UV-visible absorbance spectrum of CeONP was obtained using a Genesys UV/visible (ThermoFisher Scientific) spectrophotometer. The core sizes and morphologies of CeONP were determined using transmission electron microscopy (TEM). A Tecnai T12 microscope (FEI) was operated at 100 kV to acquire the micrographs. ImageJ software was used to manually measure the diameters of 500 individual nanoparticles for core size analysis. A Nano-ZS Zetasizer system (Malvern Instruments) was used to measure the hydrodynamic diameters and zeta potentials. The concentration of CeONP solution was measured by using ICP-OES (Spectro Analytical Instruments GmbH). The X-ray diffraction (XRD) pattern of dried CeONP was characterized by a Rigaku GiegerFlex D/Max-B X-ray diffractometer in the range of 20° to 90° at a scan rate of 2° per minute. For energy-dispersive X-ray spectroscopy (EDX), CeONP were dried onto a copper grid before recording their EDX spectra using a Quanta 600 field emission gun scanning electron microscope. A JASCO FT/IR-480 Plus spectrophotometer was used to collect the infrared spectra of CeONP and citric acid powder. The samples were prepared by grinding dried CeONP solution into powder with dried potassium bromide and pressing into a compact pellet.

4.3.4 *In vitro* phantom CT imaging

CeONP, cerium nitrate precursor salt, glutathione-coated gold nanoparticles and iopamidol were suspended in water at a range of concentrations (0.5 to 8 mg Ce/ml) in 0.2 ml flat cap microcentrifuge tubes. For imaging in a SOMATOM Force clinical CT scanner (Siemens Healthineers, Germany), the tubes were placed in a 3D printed tube holder that was designed to fit in the borehole of an anthropomorphic thorax phantom

body (QRM GmbH, Germany). The phantom body mimics human thorax in dimension (20 x 30 x 20 cm), the organ density and CT attenuation. The following parameters were used to acquire the CT images: helical acquisition at tube potentials of 80, 100, 120 and 140 kVp, tube current of 360 mA, beam filtration of 0.3 mm titanium and 0.5 mm aluminum, exposure time of 0.5 s, slice thickness of 0.5 cm, and field of view of 370 × 370 mm. The CT images were analyzed using OsiriX software (Pixmeo, Switzerland). Circular ROIs were drawn on five slices of the axial plane for each tube. The mean attenuation values were normalized to the water tubes. The slope of the linear regression line between attenuation and sample concentration was used as the attenuation rate.

4.3.5 *In vitro* cytocompatibility

The biocompatibility of CeONP with HepG2 (hepatocytes), RAW264.7 (macrophages), Renca (epithelial kidney cells) and SVEC4-10EHR1 (endothelial cells) was assessed by measuring the cell *viability* after CeONP treatment. Each cell line was seeded at 1×10^5 cells/well in 24-well plates and was cultured overnight. After the initial cell culture, the media was exchanged with fresh media with various concentrations of CeONP (0, 0.1, 0.25, 0.5, 1, 2.5 mg Ce/ml). The cells were incubated in the CeONP-treated media for 24 hours prior to media removal and addition of LIVE/DEAD stain. The cells were stained for 20 minutes for fluorescent imaging of cell nuclei, live cells and dead cells at four different fields of view per well. The cell *viability* was calculated by dividing the live cell count by the total cell count.

4.3.6 Superoxide dismutase and catalase mimetic activity assays

SOD-mimetic activity of CeONP was measured with a SOD colorimetric activity kit (Invitrogen). CeONP stock solution was diluted to varying concentrations ranging from 0.01 to 1 mg Ce/ml in PBS. 10 μ l of each concentration were added to the wells of a 96-well plate. Upon subsequent additions of the substrate and xanthine oxidase to the wells per instruction, the mixture was incubated at room temperature for 20 minutes before reading the absorbance at 450 nm. Catalase-mimetic activity of CeONP was conducted with an Amplex red hydrogen peroxide/peroxidase assay kit (Molecular Probes, Inc.). CeONP solutions of varying concentrations ranging from 0.01 to 1 mg Ce/ml were prepared in the reaction buffer. After adding 50 μ l of CeONP to the wells of a 96-well plate, 50 μ l of 40 μ M hydrogen peroxide was subsequently added. After 20 minutes of incubation, 50 μ l of working solution (100 μ M 10-acetyl-3,7-dihydroxyphenoxazine and 0.2 U/ml horseradish peroxidase) was added to each well. The mixture was allowed to react at room temperature for another 30 minutes before reading the absorbance at 560 nm.

4.3.7 Intracellular ROS and RNS (reactive nitrogen species) production level

The cellular levels of ROS in macrophages were measured by using a ROS sensitive dye, chloromethyl 2'7'-dichlorodihydrofluorescein diacetate (CM-H₂DCFHDA). RAW 264.7 macrophage cells were seeded in 96-well plates at a density of 2×10^4 cells/well and were cultured overnight. Then, the cell culture media was exchanged with fresh media for the LPS- group and fresh media with 200 ng/ml of LPS for the LPS+ groups to start lipopolysaccharide (LPS) stimulation. After 1 h, CeONP solutions of different concentrations (i.e., 0 mg/ml for the LPS- group and 0, 0.01, 0.05, 0.1, 0.5 or 1 mg/ml for the LPS+ groups) were added to the cell culture media, and the cells were further

incubated for another 23 hours. To end LPS stimulation and CeONP treatment, the cells were washed twice with PBS before incubating with 10 μ M of CM-H₂DCFHDA solution for 20 minutes at 37 °C. At the end of dye incubation, RAW 264.7 cells were washed with PBS once before being resuspended in PBS to allow cells to recover for 5 minutes at 37 °C. The fluorescence intensity was measured at excitation wavelength of 492 nm and emission wavelength of 527 nm.

The identical cell culture and treatment conditions were used to assess the production levels of RNS (i.e., nitric oxide) by RAW 264.7 macrophages. A Griess Reagent kit (Invitrogen) was used to detect the nitrite concentrations. After the LPS stimulation and CeONP treatment, 100 μ l of cell culture media was collected and mixed with an equal volume of Griess reagent (N-(1-naphthyl)- ethylenediamine, sulfuric acid and deionized water). After 30 minutes of incubation at room temperature, the absorbance was measured at 548 nm.

4.3.8 Pro- and anti-inflammatory mRNA expression

mRNA expression and cytokine release levels of both pro-inflammatory cytokines (TNF α and IL-1 β) and anti-inflammatory cytokine (IL-10) from RAW 264.7 macrophages were assessed. The cells were seeded at a density of 1×10^6 cells/well in 6-well plates and were cultured overnight. At which point, the media was removed and replaced with fresh media with or without LPS to start the LPS stimulation. The LPS and CeONP treatment conditions were identical to the previous setup in ROS and RNS assessment. At the end of the treatment, the media were removed to evaluate the cytokine levels of TNF α , IL-1 β and IL-10 *via* ELISA kits. The cells were also separately collected for the assessment of their mRNA expression levels. Total RNA isolated from RAW 264.7

macrophages using Trizol reagent (Thermo Fisher) were subjected to RT-PCR to assess mRNA expression using the following primers: IL-1beta-Fwd; 5'-ATGGCAACTGTTTCCTG-3', IL-1beta-Rev; 5'-TTAGGAAGACACGGAT-3', TNF-alpha-Fwd; 5'-ATGAGCACAGAAAGCA-3', TNF-alpha-Rev; 5'-TCACAGAGCAATGACT-3', IL-10-Fwd; 5'-ATGCCTGGCTCAGCAC-3', IL-10-Rev; 5'-TTAGCTTTTCATTTTG-3', GAPDH-Fwd; 5'-ATGCTGCCCTTACCCCGG-3', and GAPDH-Rev; 5'-TTACTCCTTGGAGGCCAT-3'.

4.3.9 Macrophage cellular uptake assay

LPS-stimulated, CeONP-treated macrophages were washed in PBS and collected by scraping and centrifuging at 160 rcf for 5 minutes. The cells collected in a pellet were then fixed in a solution that contained 2.5 % glutaraldehyde and 2 % formaldehyde. The fixed cell pellet was cut into thin sections (~ 60 nm), stained, and placed on copper grids for TEM analysis.

4.3.10 Western Blotting Analysis

For Western blotting, proteins were resolved by SDS-PAGE and transferred onto 0.45µm PVDF membranes (Millipore). Membranes were blocked overnight at 4 °C with 5% milk in PBS and 0.5% Tween-20 (PBST). Membranes were incubated for 60 mins with one of the following antibodies: rat monoclonal anti-CD68 (Abcam; 1:1000), rabbit monoclonal TNFα (Cell Signaling; 1:1000), mouse monoclonal IL-1β (Thermo Fisher; 1:1000), and mouse monoclonal IL-10 (Santa Cruz; 1:1000). This was followed by 1h incubation with horseradish peroxidase-coupled goat anti-mouse, anti-rabbit, and anti-rat secondary antibodies (Thermo Fisher; 1:1000). Detections were performed with Pierce™ ECL Western Blotting substrate (Thermo Fisher). Signals were quantified using ImageJ.

4.3.10 *In vivo* studies

All *in vivo* studies were performed on male C57BL/6J mice (Jackson Laboratory) of 12 weeks in age and ~25 g in body weight. All procedures were performed in accordance with the guidelines approved by the University of Pennsylvania Institutional Animal Care and Use Committee.

4.3.10.1 Peripheral inflammation model induction and paw edema thickness

Using digital calipers, basal widths of both hind paws of mice were first measured immediately before the onset of inflammation. Peripheral inflammation was induced by injecting 20 μ l of complete Freund's adjuvant (CFA) (Sigma) subcutaneously in the central plantar region of left hind paws (ipsilateral), as reported in a previous study.³² At 24 h post-CFA, the paw thickness of the ipsilateral (injured) paw, as index of edema, was measured shortly before the start of treatment (0 h time point). The paw thickness of the contralateral (uninjured) paw was also measured to assess off-target effects of CFA. To assess the *in vivo* immunomodulatory effects of CeONP, the mice were randomized to two groups and were administered with either 100 μ l of saline (vehicle) or CeONP (dose of 100 mg Ce/kg). The paw thicknesses of both ipsilateral and contralateral paws of each mouse were measured at 3, 6, 18 and 24 h post-treatment in a blinded fashion. The paw thicknesses at each time point and the net change compared to the basal width at 0 h were compared between vehicle injection group (n=8) and CeONP treatment group (n=7).

4.3.10.2 Behavioral testing: thermal pain hypersensitivity

The thermal pain hypersensitivity test was performed using a heated glass-based plantar analgesiometer (Stoelting). Before the assessment, each mouse was placed in an individual plexiglass cubicle on a glass surface that was warmed to 30 °C daily for 1 h to allow mice to acclimate to the environment. The baseline measurements were taken prior to the CFA injection (-24 h) and to the treatment (0 h) with either saline (n=4) or CeONP (n=4). A light beam was used to produce heat by creating an intense focal spot under the paw. Paw withdrawal latency (PWL), which was defined as the time between the onset of heat stimulus and paw withdrawal in response, was recorded at 3, 6, 18, and 24 h post-treatment. A cut-off of 20 seconds was set to prevent tissue damage. At each time point, each mouse was tested in five sequential trials with an interval of 2-3 minutes. PWL was measured on both ipsilateral (injured) and contralateral (uninjured) hind paws.

4.3.10.3 Biodistribution

At 24 h post-treatment, mice were sacrificed to analyze the biodistribution of CeONP. Blood samples, major organs (i.e., heart, lungs, liver, spleen, kidneys), hind paws, and the remaining carcass from each CeONP-treated mouse were harvested and homogenized for tissue digestion. The concentration of cerium in the digested samples were measured using ICP-OES. The results were analyzed by % injected dose (% ID) and % injected dose per gram of tissue (% ID/g).

4.3.11 Ex vivo studies

4.3.11.1 Renal clearance of CeONP

To further investigate the renal clearance of CeONP, urine samples of mice from CeONP-treatment group were collected 3 h post-injection. The collected urine samples were placed on copper grids for TEM analysis.

4.3.11.2 *In vivo* toxicity

Heart, lungs, liver, spleen, and kidneys from both vehicle and CeONP treatment groups were collected at 24 h post-treatment for histological analysis *via* H&E staining. Each tissue was sliced at thickness of 12 microns for staining.

4.3.11.3 *In vivo* immunomodulatory effect of CeONP

The immunomodulatory effects of CeONP in the paw inflammation model was investigated by performing Western blotting and immunohistochemistry of several biomarkers – CD68 (M1 macrophage), TNF α and IL-1 β (pro-inflammatory cytokines) and IL-10 (anti-inflammatory cytokine). Histological analysis *via* H&E staining was also conducted. The immunomodulatory effect was assessed by comparing the results with hind paws of wild-type (no CFA injection or treatment) and vehicle groups.

4.3.12 Statistical analysis

One-way analysis of variance (ANOVA) and Tukey-Kramer HSD posthoc test were used to examine statistical significance in differences between the groups when there are more than 2 groups to compare (e.g., *in vitro* experiments). A two-sample t-test was used

when there are only 2 groups in comparison (e.g., *in vivo* experiments). Data is presented in mean \pm SD unless indicated otherwise.

4.4 Results

4.4.1 Synthesis and characterization of citric acid coated CeONP

Ultrasmall citric acid coated CeONP were synthesized *via* a one-step coprecipitation of cerium precursor and citric acid in ammonium hydroxide as depicted in Figure 4.1A. As the reaction proceeded, the color of the solution became yellow. The final solution had peak UV-vis absorbance at 265 nm (Figure 4.1B).^{9, 33} The citric acid coating was used to provide hydrophilicity and stability of CeONP in physiological buffer solutions, such as PBS (Figure 4.1C). As shown in the transmission electron micrographs (Figure 4.1D), CeONP are nearly spherical with an average core diameter of 2.8 ± 0.4 nm. The citric acid coating on the surface led to hydrodynamic diameter that is slightly larger (3.4 ± 1.1 nm) than the core diameter and negative ζ -potential (19.5 ± 3.2 mV) as shown in Figure 4.1E. The elemental composition of CeONP was analyzed with further characterization methods with energy-dispersive X-ray spectroscopy (EDX), X-ray diffraction analysis (XRD) and Fourier transform infrared spectroscopy (FT-IR). EDX verified that the main elemental components of the core nanoparticles are cerium and oxygen (Figure 4.1F), and the XRD diffraction pattern confirmed a fluorite lattice structure of CeONP highlighted by a strong (111) peak (Figure 4.1G).³⁴ Similarities in FT-IR spectra of citric acid powder and citric acid coated CeONP demonstrated that the surface coating of citric acid molecules was intact (Figure 4.1H). Notably, the characteristic peak of C=O vibration at 1701 cm^{-1} from the carboxylic acid group of citric acid was shifted to 1579 cm^{-1} in citric acid coated CeONP, indicating successful bindings of citric acid molecules onto

the nanoparticle surfaces.³⁵ The peak at 1396 cm^{-1} from the bending of tertiary hydroxyl group of citric acid was also observed in both FTIR spectra.³⁶

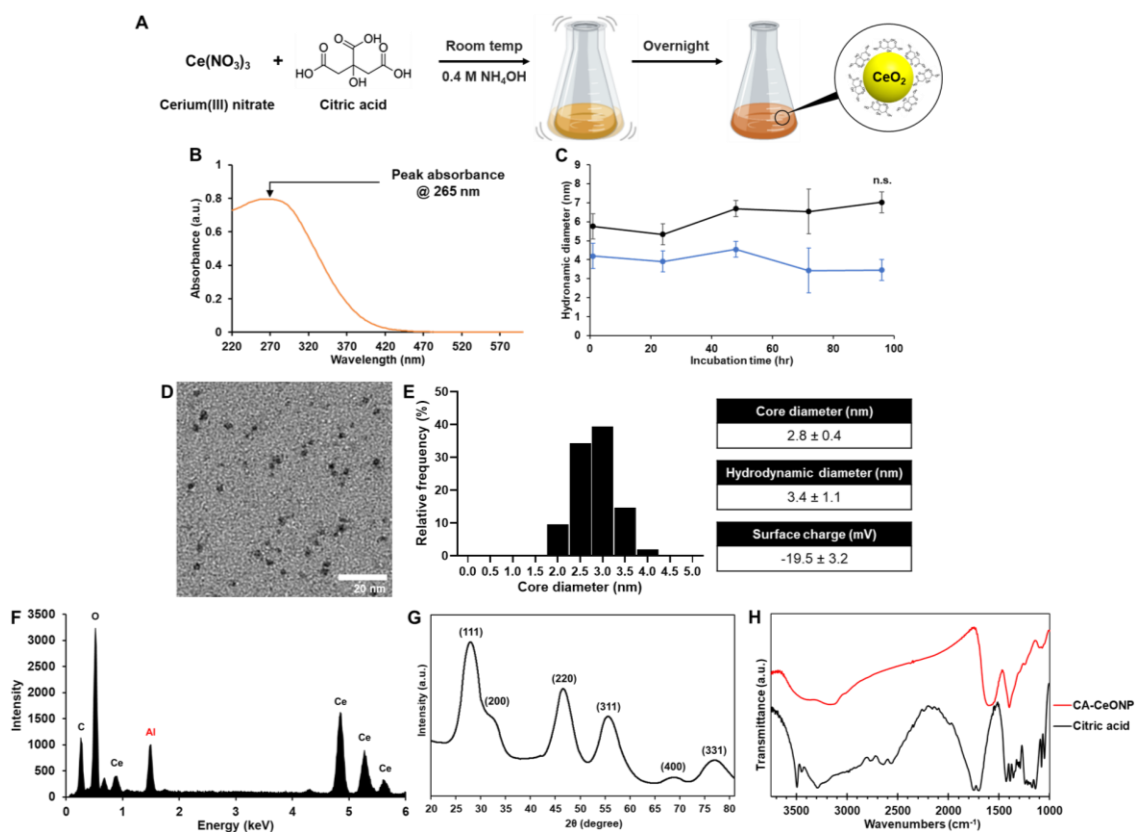


Figure 4.1 Characterization of citric acid coated CeONP.

A) Schematic depiction of CeONP synthesis. B) UV-vis spectrum, C) hydrodynamic diameters in water and PBS, D) micrograph from TEM, E) core and hydrodynamic diameters and surface charge, F) EDX spectrum, and G) XRD pattern of CeONP. H) FTIR spectra of citric acid and CeONP.

4.4.2 *In vitro* cytocompatibility

To evaluate the feasibility of using CeONP for biomedical applications, the safety and cytotoxicity of CeONP were first examined by assessing the *viability* of endothelial

cells, hepatocytes, kidney epithelial cells and macrophages upon CeONP treatment. These cell types will likely have the highest exposure and accumulation once CeONP have entered the systemic circulation *in vivo*. 24 h of CeONP treatment did not substantially decrease the *viability* of any of the cell types in this study even at high dose of 2.5 mg Ce/ml (Figure 4.2). The lowest *viability* observed was $98.5 \pm 1\%$ in hepatocytes that were treated at concentration of 2.5 mg Ce/ml. The lack of substantial reduction in cell *viability* demonstrates the excellent cytocompatibility of the CeONP formulation. As the cytotoxicities of nanoparticles are largely affected by their physiochemical properties, the biocompatible and stable citrate coating likely prevented induction of toxic effects to these cells. Furthermore, we expect the actual exposure of these cells to CeONP to be much lower in both concentration and time than the parameters used in this experiment due to efficient renal excretion.

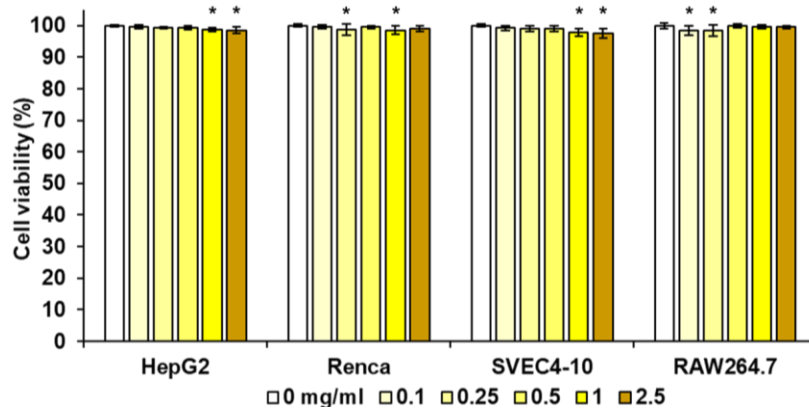


Figure 4.2 *In vitro* cytotoxicity of citric acid coated CeONP.

Cell *viability* of HepG2, Renca, SVEC4-10 and RAW264.7 after 24 h of CeONP treatment normalized to no treatment group. * $p < 0.05$.

4.4.3 *In vitro* contrast generation

The potential to detect CeONP in CT imaging was investigated by assessing the CT contrast properties of CeONP in an *in vitro* phantom study using a SOMATOM Force clinical CT scanner. The attenuation rates of CeONP were compared to those of cerium precursor, AuNP (a leading experimental CT contrast agent) and iodinated contrast agent (iopamidol). A strong linear correlation ($R^2 > 0.997$) between the attenuation values and the cerium concentrations was observed (Figure 4.3A). The attenuation rate of CeONP was the highest at 80 kVp and steadily declined with increasing tube voltages (Figure 4.3B). The decline is due to cerium's K-edge energy of 40.4 keV, at which the number of photons at the energy level is the highest when scanned at 80 kVp, followed by 100 kVp, 120 kVp and 140 kVp, respectively. Despite the decline, CeONP had consistently higher attenuation rate over that of iopamidol, a commonly used CT contrast agent, across all tube potentials tested. The attenuation of CeONP was also much higher than that of AuNP in 80, 100, 120 kVp, demonstrating the potential advantages of using cerium-based nanoparticles for contrast-enhanced CT imaging. However, relatively low elemental density of cerium and of cerium payload in CeONP can limit their use for certain imaging applications, in which high payload delivery may be required.

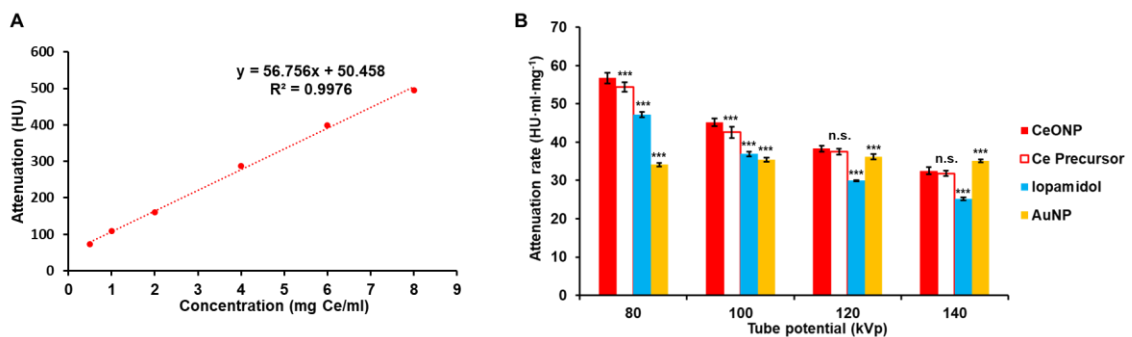


Figure 4.3 *In vitro* contrast generation of CeONP in clinical CT imaging.

A) Attenuation of CeONP at a range of concentrations. B) Attenuation rates of CeONP compared to cerium precursor salt, iopamidol and AuNP. (n.s. = not significant or $p > 0.05$, *** = $p \leq 0.001$ compared to CeONP).

4.4.4 Enzyme-mimetic antioxidative activities

An array of antioxidant enzymes is present in the body to protect cells from oxidative stress.⁴ The main examples of such enzymes are SOD and catalase, which help break down two predominant forms of cell-derived ROS, superoxide and hydrogen peroxide, into oxygen and water molecules.³⁷ The SOD-mimetic and catalase-mimetic activities of CeONP were investigated to determine whether their citric acid coating allowed catalysis to occur. A dose-dependent increase in SOD-mimetic activity was observed, demonstrating effective removal of superoxide ions by CeONP (Figure 4.4A). Similarly, high levels of catalase-mimetic activities of CeONP were observed in a dose-dependent manner, where the conversion rate plateaued at 0.05 mg/ml (Figure 4.4B). These results demonstrate the ability of citric acid coated CeONP to efficiently catalyze the conversion of superoxide anion to hydrogen peroxide, as well as of hydrogen peroxide to oxygen and water molecules.

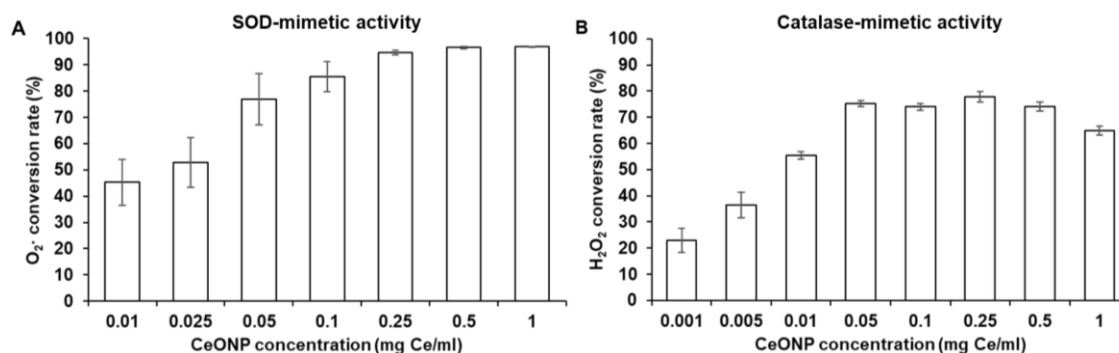


Figure 4.4 ROS scavenging activities of CeONP.

Scavenging efficiency of CeONP against A) superoxide ion and B) hydrogen peroxide.

4.4.5 *In vitro* ROS and RNS scavenging activities

The reactive oxygen species scavenging activities of CeONP were further demonstrated in a cellular environment by examining the intracellular ROS and NO production levels in LPS-stimulated macrophages. ROS and other inflammatory mediators, such as NO, are vigorously produced in macrophages upon LPS stimulation through activation of TLR4 and NADPH oxidase.³⁸⁻⁴⁰ The intracellular ROS levels were evaluated using an ROS-sensitive dye, DCFH-DA, that forms a fluorescent compound once it is oxidized after being cleaved by intracellular esterases. As shown in Figure 4.5B, LPS stimulation caused a significant elevation in intracellular ROS level, and CeONP treatment resulted in marked suppression of intracellular ROS levels in the LPS-stimulated macrophages. The reduction was significant even at the lowest treatment concentration of 0.01 mg or 10 μ g Ce/ml. TEM analysis of CeONP-treated, LPS-stimulated macrophages revealed active cellular uptake of CeONP at both low (0.05 mg Ce/ml) and high (0.5 mg Ce/ml) treatment concentrations (Figure 4.5A), implying that CeONP can scavenge intracellular ROS by directly interacting with ROS molecules in the cellular compartments. The suppression of intracellular ROS levels also demonstrates that ROS-scavenging activity of CeONP is preserved in a cellular environment, specifically of macrophages.

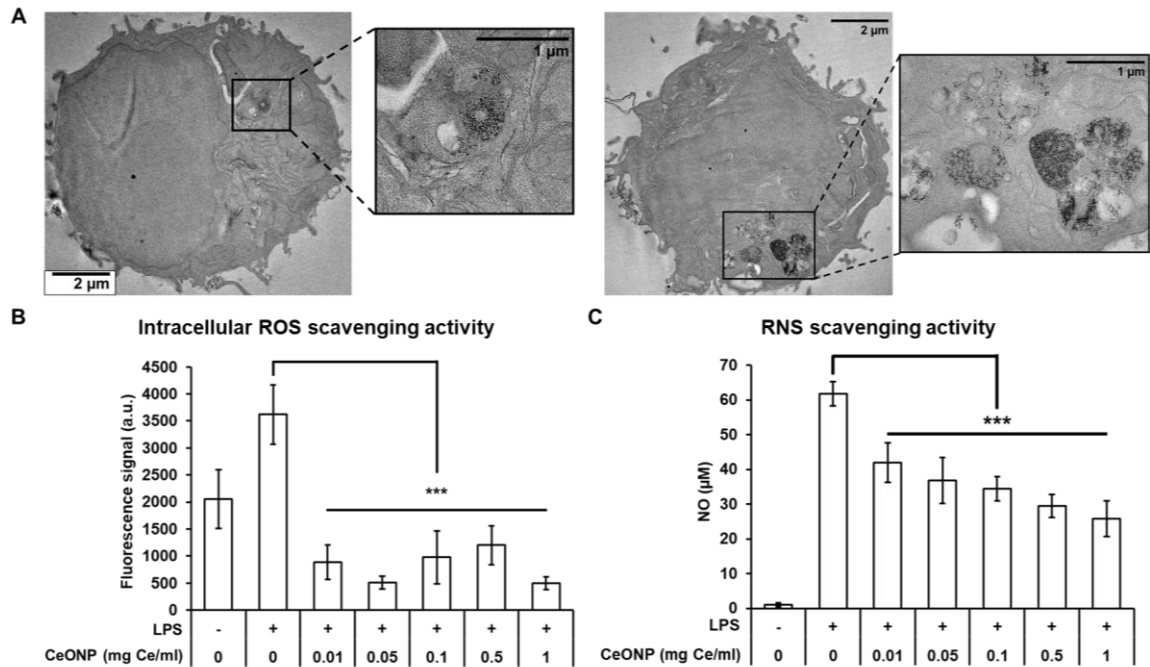


Figure 4.5 Reactive species scavenging activity of CeONP in macrophages.

A) TEM of CeONP-treated macrophages at concentrations of 0.05 mg/ml (left) and 0.5 mg/ml (right). B) Intracellular ROS levels and C) RNS production levels in control and LPS-stimulated macrophages upon CeONP treatment. *** $p < 0.001$.

Another well-established inflammatory mediator is RNS, namely nitric oxide (NO).⁴¹ Overproduction of NO by macrophages in response to inflammatory stimuli can cause damage to healthy tissues through both macrophage-mediated cytotoxicity and formation of peroxynitrite *via* interaction with other ROS in the environment.⁴² Therefore, inhibition of NO production in macrophages was also examined. Similar to intracellular ROS production, LPS stimulation of macrophages significantly elevated NO production when compared to the unstimulated cells (Figure 4.5C). Subsequent CeONP treatment

notably decreased the NO production in a dose-dependent manner. NO production was significantly lowered even at the lowest treatment concentration tested (0.01 mg Ce/ml).

4.4.6 *In vitro* anti-inflammatory effect

Previous studies have shown that both ROS and RNS can regulate LPS-induced signal transduction in phagocytic immune cells, predominantly in macrophages, to induce secretion of proinflammatory cytokines, namely IL-1 β and TNF α .^{5, 39, 43} To examine whether ROS and RNS scavenging activities of CeONP in activated macrophages can translate to suppression of proinflammatory cytokine secretion, we assessed the mRNA expression and cytokine secretion of TNF α and IL-1 β upon CeONP treatment.

LPS-induced activation of macrophages elevated mRNA expression of TNF α by more than 6-fold (Figure 4.6A) and was abated by CeONP treatment. While the downregulation was gradual at lower doses of CeONP, it was significant at higher doses (i.e., 0.5 and 1 mg Ce/ml) when compared to non-treated macrophages. A similar pattern of inhibition was observed in IL-1 β – minor decline at lower dose treatment and significant reduction at higher doses (Fig 5.6B). Interestingly, CeONP treatment reduced the cytokine secretion of both TNF α and IL-1 β much more robustly than it did for their mRNA expression, significantly repressing the secretion at 0.01 mg/ml for TNF α and 0.1 mg/ml for IL-1 β (Fig 5.6D and E).

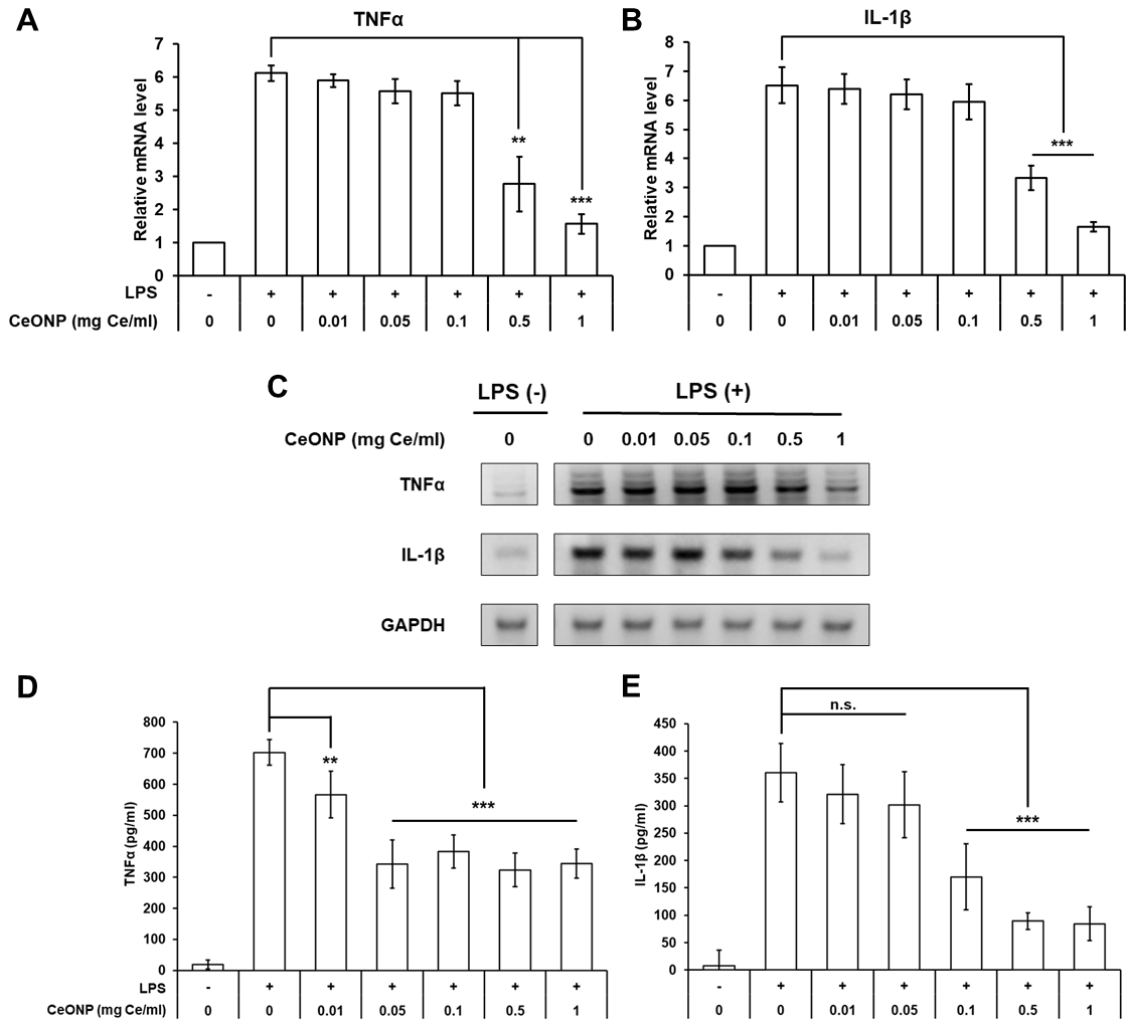


Figure 4.6 *In vitro* anti-inflammatory effect of CeONP in LPS-stimulated macrophage cells. mRNA expression levels of A) TNF α , B) IL-1 β and C) both in gel image normalized to GAPDH. Cytokine secretion of D) TNF α and E) IL-1 β . n.s. not significant, **p < 0.01, ***p < 0.001.

We also investigated the secretion of IL-10 in macrophages upon CeONP treatment. IL-10 is a cytokine with potent anti-inflammatory properties that is known to inhibit expression of proinflammatory cytokines, such as TNF α , IL-1 β , and IL-6, and to

eliminate dysfunctional mitochondria that generate excessive amounts of ROS.⁴⁴ LPS-stimulation resulted in a slight increase in mRNA expression of IL-10 (Figure 4.7A and B). Upon CeONP treatment, mRNA expression of IL-10 was continuously elevated in a dose-dependent manner. A similar pattern of upregulation was observed in cytokine secretion as well. However, the level of secretion declined when the cells were treated with CeONP concentration higher than 0.1 mg/ml (Figure 4.7C).

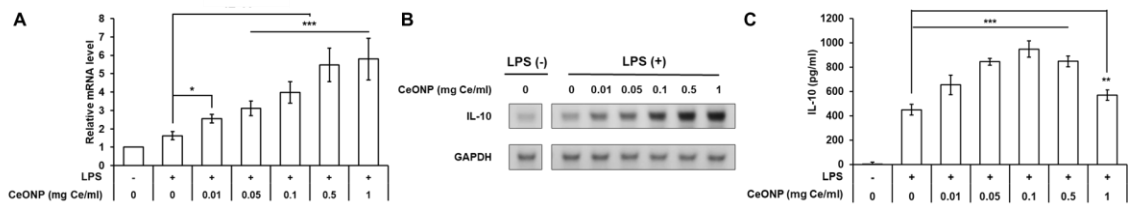


Figure 4.7 IL-10 expression of LPS-stimulated RAW 264.7 cells.

A) mRNA expression level, B) corresponding gel electrophoresis image, and C) cytokine release level of IL-10 in LPS-stimulated RAW 264.7 cells.

4.4.7 *In vivo* immunomodulatory effect

Paw edema reduction. To evaluate the immunomodulatory effect of CeONP *in vivo*, we studied whether CeONP can reduce edema and decrease pain hypersensitivity in mice that suffer from acute hind paw inflammation. CFA injections directly in the left paws of mice induced local inflammation, causing noticeable redness and swelling that significantly increased the paw thickness (Figure 4.8).

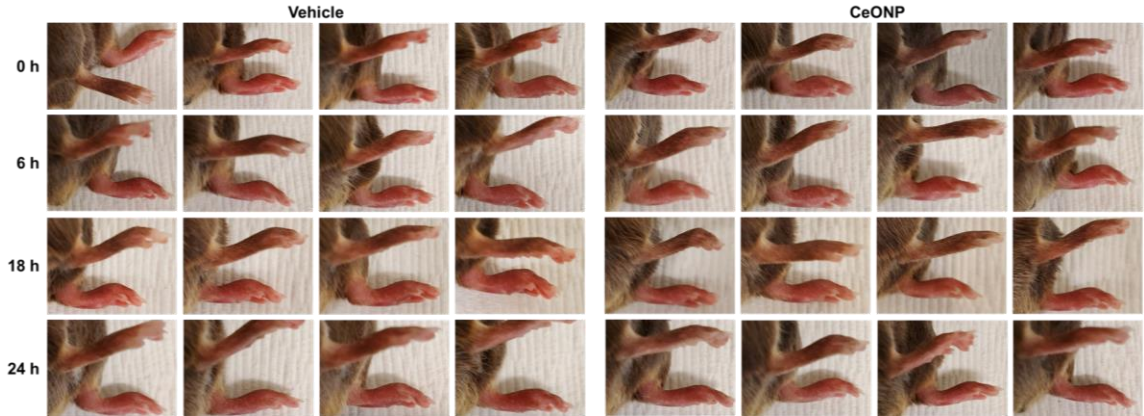


Figure 4.8 Images of inflamed paws of vehicle injected and CeONP treated mice over 24 h period.

After a single dose injection of CeONP *via* the tail vein, the edema in the left paw was quickly alleviated, as shown by a rapid decline in paw thickness over the 24 h post-injection period, demonstrating the efficacy of CeONP in modulation of acute inflammatory response. (Figure 4.9A). Vehicle (saline) injection, on the other hand, did not cause any significant reduction in paw thickness. When comparing the changes in paw thickness between CeONP-treated and vehicle-injected groups over the monitored time, a significant difference was observed as early as 6 h post-injection, and the difference continued to grow over the next 18 h. No significant change in contralateral paw thickness and body weight was observed in both treatment groups during the monitoring (Figure 4.10).

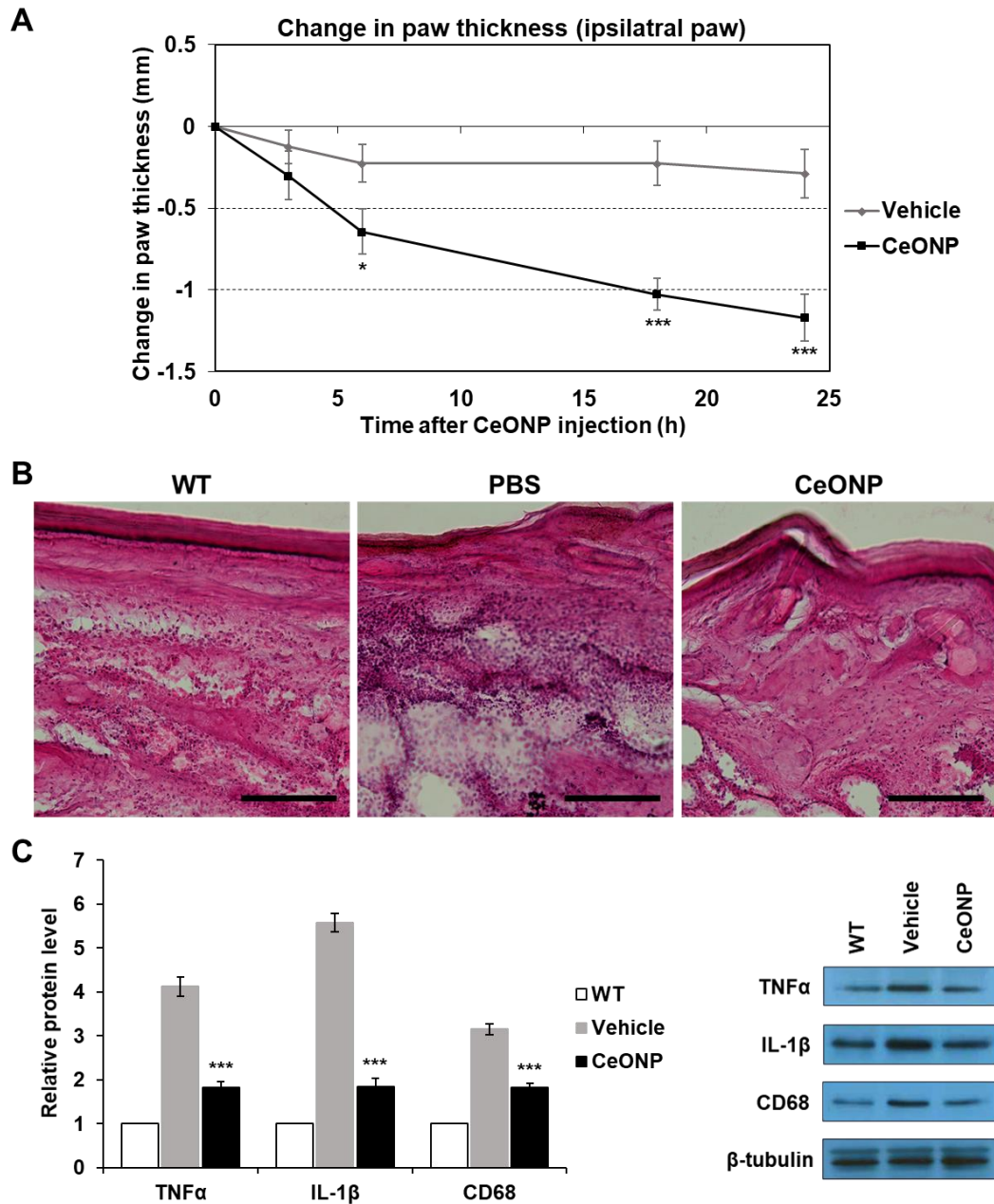


Figure 4.9 *In vivo* edema reduction and suppression of proinflammatory cytokines and macrophage recruitment in acute hind paw inflammation.

A) Change in paw thickness over 24 h post-injection period in comparison to immediately before the treatment (0 h). B) H&E staining of acute inflammation site from wild type,

vehicle and CeONP treatment group. Scale bar = 50 μm . C) Western blot analysis of TNF α , IL-1 β and CD68 in inflamed paws of each group. No inflammation was induced in wild-type mice. Data presented as mean \pm SEM. * $p < 0.05$, ** $p < 0.01$, *** $p < 0.001$.

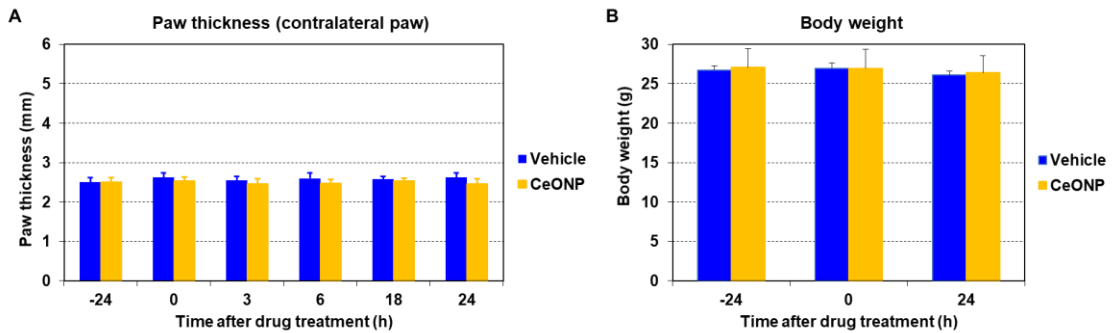


Figure 4.10 Off-site effect of CeONP treatment.

A) Paw thickness of contralateral paws (no inflammation induction *via* CFA injection). B) body weight of mice during CFA injection and CeONP treatment.

Reduction in macrophage recruitment and proinflammatory cytokine expression.

The modulation of acute inflammation in the paw was further examined *via* histologic analyses and western blotting. H&E staining of inflamed paws of mice that were injected with saline clearly showed histopathologic alterations and elevated cell density in the region when compared to the paws of the wild-type mice (no CFA injection), suggesting damage related to inflammatory cell infiltration (Figure 4.9B). Both alteration and cell density were significantly reduced in mice that were treated with CeONP, indicating lessening degree of inflammatory response within 24 h. Western blot analyses of pro-inflammatory cytokines (i.e., TNF α and IL-1 β) and a macrophage biomarker (i.e., CD68) also showed elevated levels of all three markers in inflamed paws of vehicle injected mice compared to those of wild-type counterparts (Figure 4.9C). 24 h after CeONP treatment

markedly reduced the cytokine expression and CD68 levels when compared to the vehicle group. Reduction in CD68 implies that the reduction in cell density is possibly due to abatement in macrophage cell recruitment and infiltration to the inflammation site. Western blotting further showed that the immunomodulation in CeONP-treated group was also influenced by increased IL-10 expression (Figure 4.11).

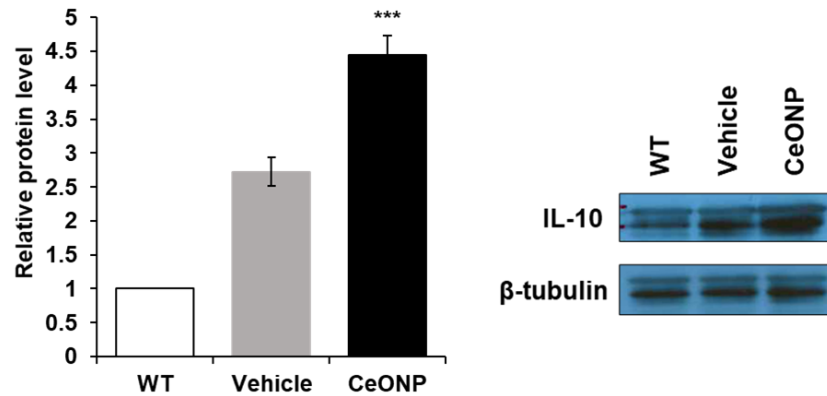


Figure 4.11 *In vivo* IL-10 expression in mice.

Western blot analysis of IL-10 in inflamed paws of each treatment group. No inflammation induction in WT.

Suppression in pro-inflammatory cytokines and macrophage recruitment and upregulation of an anti-inflammatory cytokine were further investigated by immunofluorescence staining. As shown in Figure 4.12, secretion of both TNF α and IL-1 β at the inflammation site were much lower in CeONP-treated group than saline group. The recruitment of CD68-positive macrophages to the inflamed region was also less in the CeONP treatment group. The yellow areas in the merged images where the cytokines and CD68 markers are co-localized indicate that significant amounts of TNF α and IL-1 β were secreted by CD68-positive macrophages. Staining of IL-10 anti-inflammatory cytokine

also revealed that CeONP treatment promoted higher IL-10 expression at the inflammation site (Figure 4.13). Strong fluorescence signals of IL-10 were also detected in areas where CD68 markers were not prominent, indicating the possibility of upregulation of IL-10 expression by other immune cells, namely regulatory T cells.

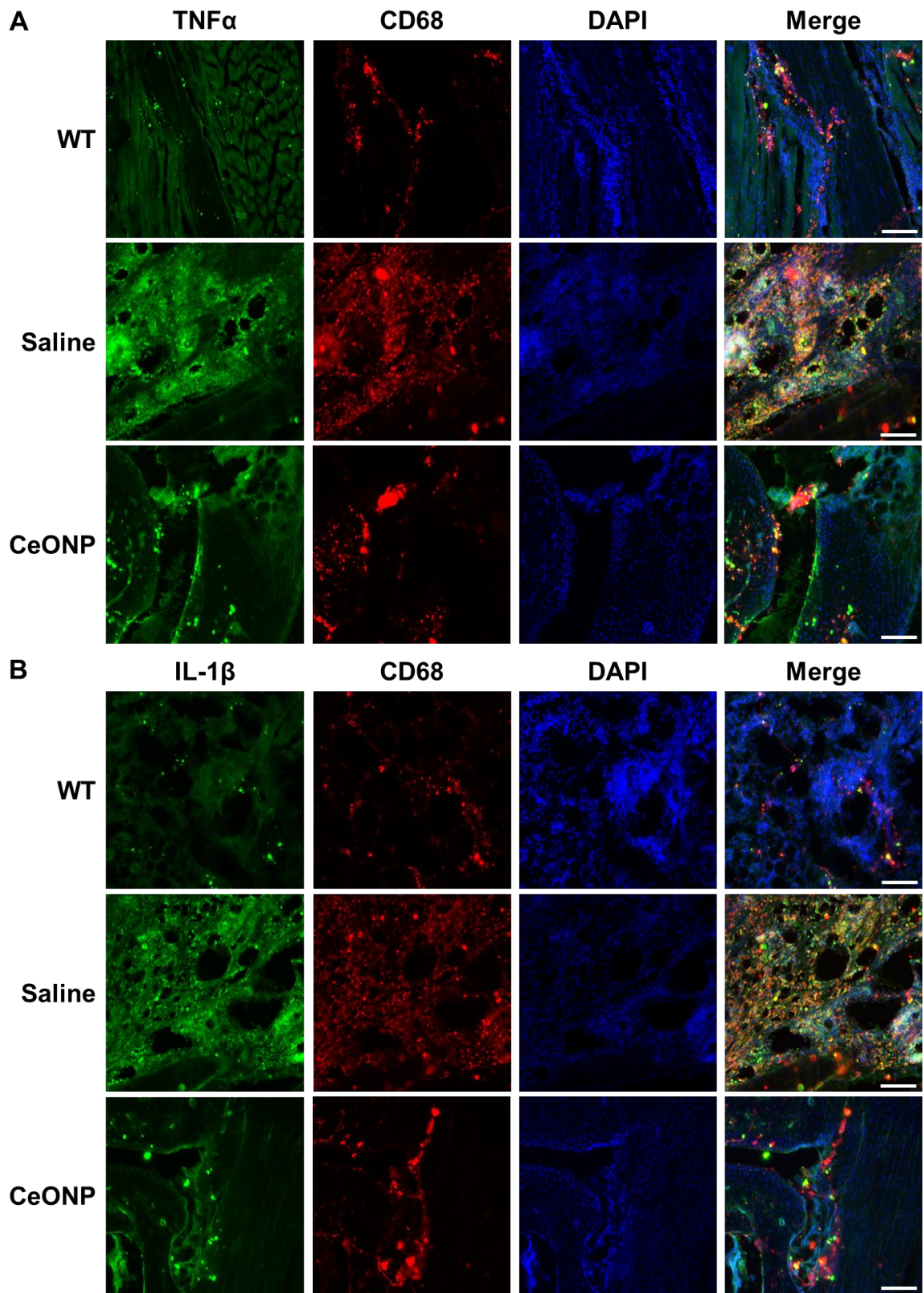


Figure 4.12 Immunofluorescence analysis of pro-inflammatory cytokines and a macrophage marker.

Immunofluorescence images of CD68 and DAPI markers in paw tissues merged with A) TNF α and B) IL-1 β markers. Scale bar = 200 μ m.

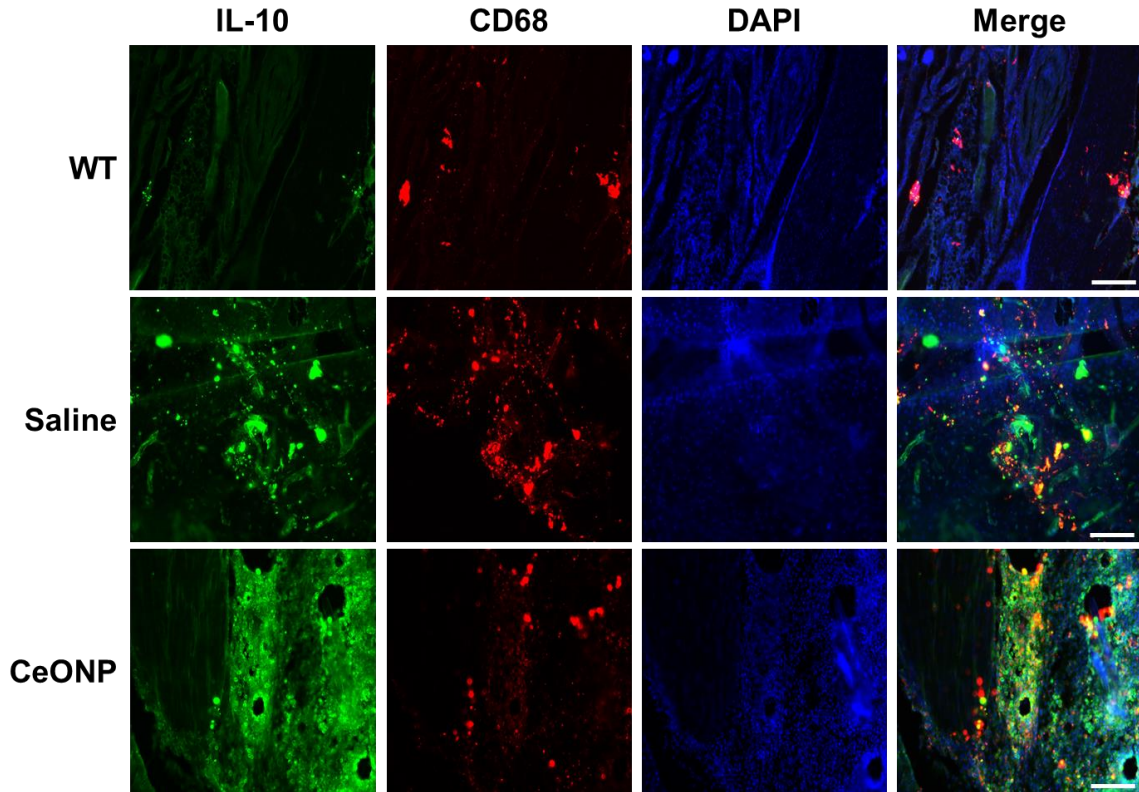


Figure 4.13 Immunofluorescence analysis of IL-10 and a macrophage marker.

Immunofluorescence staining of CD68 and DAPI markers in paw tissues merged with IL-10 marker. Scale bar = 200 μ m.

In vivo analgesic effect. CeONP treatment also resulted in significantly reduced pain hypersensitivity, measured by the increase in PWL (paw withdrawal latency defined by the time between the onset of heat stimulus and paw withdrawal in response), when compared

to the saline group over the 24 h of post-injection monitoring (Figure 4.14). A significant difference between the two groups was observed as early as 3 h post-injection, which was the earliest time point. The PWL of CeONP-treated mice at 3 h post-injection was also significantly higher than PWL immediately before the treatment (0 h timepoint), indicating fast-acting analgesic effect of CeONP. Furthermore, the PWL of CeONP-treated mice at 18 h became comparable to that of before the CFA injection (-24 h timepoint), further indicating that CeONP can alleviate pain hypersensitivity.

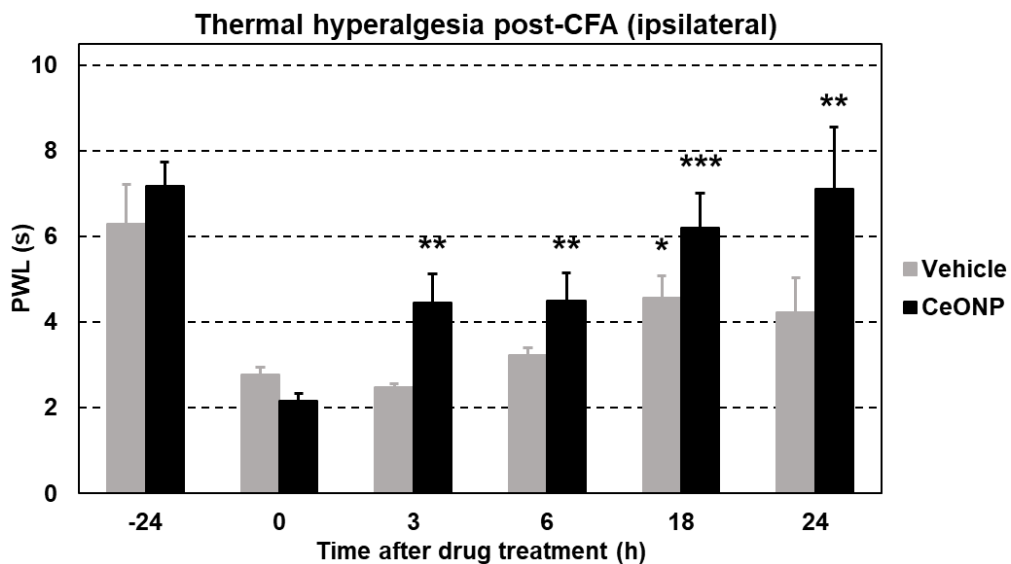


Figure 4.14 Thermal pain hypersensitivity in the hind paw acute inflammation.

PWL of individual mouse injected with vehicle and CeONP over 24 h post-injection. Data presented as mean \pm SEM. * $p < 0.05$, ** $p < 0.01$, *** $p < 0.001$.

4.4.8 Biodistribution and renal clearance

The biodistribution of CeONP was also investigated in the acute paw inflammation mouse model at 24 h post-injection to examine the efficacy of CeONP clearance and to analyze the accumulation of CeONP at the inflamed paw. ICP-OES analysis demonstrated

that less than 16 %ID was found in the body at 24 hours post-injection (Figure 4.15A). This suggests that more than 84 %ID was excreted from the body *via* urine and feces. Micrographs from TEM of CeONP found in urine samples collected at 2 h post-injection further support efficient excretion (Figure 4.15C). The average retention of ~16 %ID is comparable or lower than other reports of renally clearable nanoparticles.^{29, 45, 46} Such low retention can be explained by the low hydrodynamic size of CeONP, which is considerably lower than the widely accepted size threshold for renal clearance (i.e., ~ 5.5 nm) and their favorable surface chemistry.^{30, 47} Most of the CeONP retention were observed in liver and spleen. Small amounts of CeONP were also found in kidney (0.7 %ID, 1.6 %ID/g), lungs (0.3 %ID, 0.7 %ID/g), and the remaining carcass (1.2 %ID, 0.0 %ID/g). A considerable amount of CeONP was also found in the inflamed paw, which was about 10-fold higher than that of contralateral paw without inflammation (Figure 4.15B). The significantly higher accumulation in the inflamed paw can be explained by enhanced permeability and retention effect due to increased vascular permeability of the capillaries at the inflammation site.⁴⁸

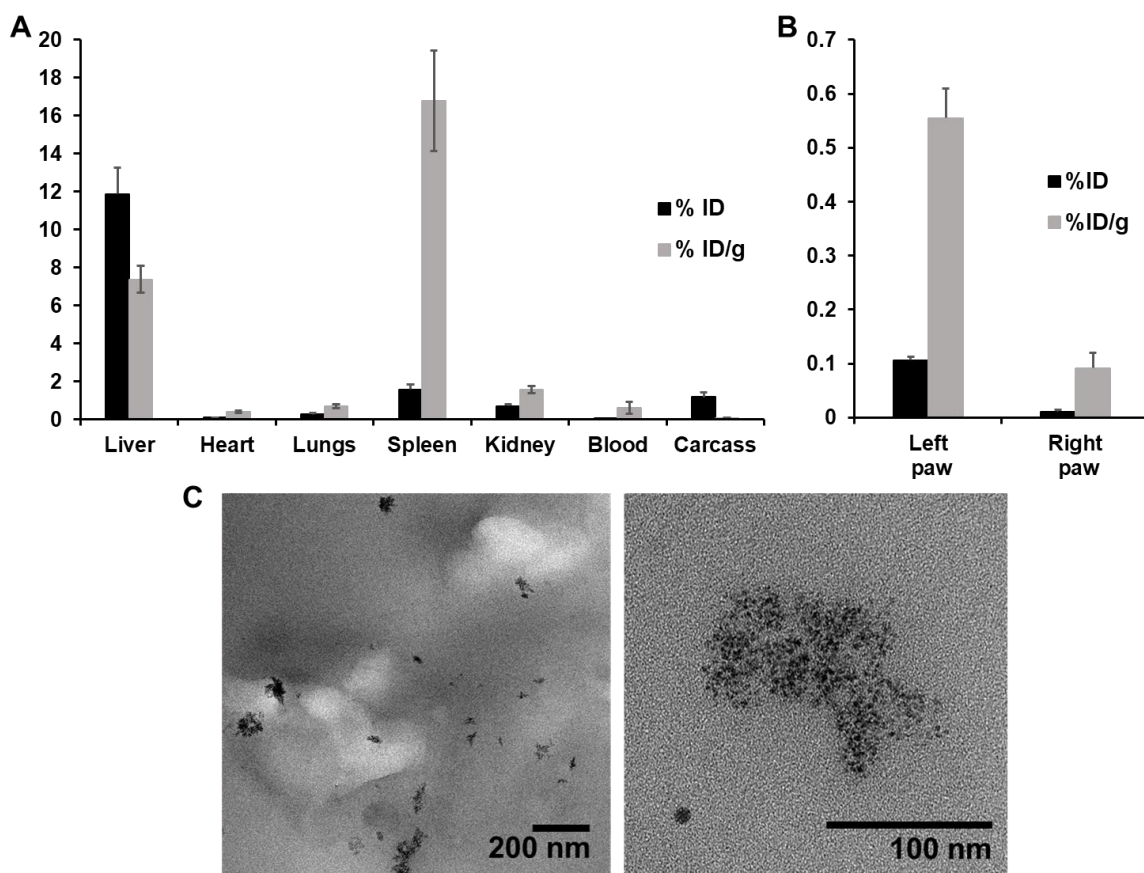


Figure 4.15 Biodistribution and renal clearance of CeONP.

A) Accumulation of CeONP in the major organs and the remaining carcass and B) ipsilateral and contralateral paws of mice at 24 h post-injection as measured by ICP-OES. C) TEM of urine samples from CeONP-treated mice collected at 2 h post-injection.

4.4.9 *In vivo* toxicity

Our *in vivo* results thus far demonstrated that CeONP can have beneficial effects at the inflammation site and be effectively cleared from the body within 24 hours; however, it is still unclear whether they have toxic effects in other major organs (e.g., heart, lung, liver, spleen, and kidney) as a portion of the dose was retained at this time point. Therefore, the major organs were harvested at the end of the *in vivo* studies for histological

analysis. H&E staining of these organs revealed no noticeable acute pathological toxicity or adverse effects in both control (saline) and CeONP-treated groups (Figure 4.16).

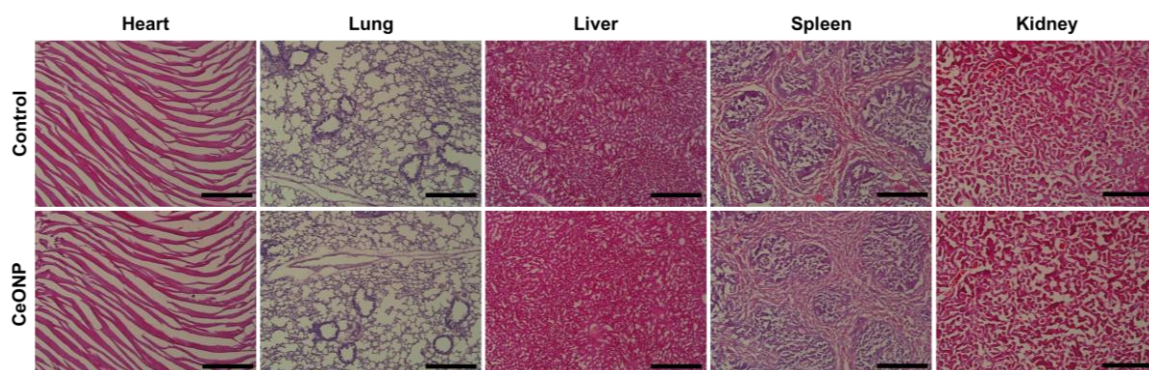


Figure 4.16 *In vivo* safety of citric acid coated CeONP.

Micrographs of H&E stained major organs (heart, lung, liver, spleen, and kidney) from mice 24 h after injection with saline (control) or CeONP at 100 mg/kg. Scale bar = 50 μ m.

4.5 Discussion

Nanoparticle characterization demonstrated stable CeONP with unimpaired citric acid surface coating. Similarly to magnetite nanoparticles, citric acid coating on CeONP surfaces provided electrostatic and steric stability to allow CeONP to retain its ultrasmall nanoparticle size and water solubility.⁴⁹ These physical and chemical properties are of importance to promote renal clearance while maintaining its immunomodulatory properties. The citric acid surface coating also did not interfere with the nanoparticles' ability to efficiently catalyze the conversion of superoxide anion to hydrogen peroxide, as well as of hydrogen peroxide to oxygen and water molecules.

CeONP's catalytic activity was extensively tested in macrophages, since they are specialized in elimination of pathogens by producing an excessive amount of reactive species.⁴ More studies are suggesting that ROS have a close relationship in activating

macrophage cells by directly promoting expression of proinflammatory genes and polarization of macrophages to proinflammatory M1.^{1, 50} While M1 macrophages function in uptake and clearance of apoptotic cells, their excessive and prolonged ROS and RNS production can cause collateral damage to healthy tissue and may even be harmful to macrophages themselves. Therefore, modulation of macrophage activation can be of promising therapeutic focus in inflammatory diseases. Our findings suggest that CeONP can prevent excessive production of ROS and NO in macrophages; therefore, can potentially modulate inflammatory responses and alleviate tissue damage from activated macrophages at the inflammation site.

In fact, our *in vitro* and *in vivo* results indicate that CeONP with strong antioxidant properties can have potent anti-inflammatory effect in activated macrophages, downregulating proinflammatory cytokines, TNF α and IL-1 β , and upregulating anti-inflammatory cytokine, IL-10. The suppression of secretion of TNF α and IL-1 β were sustained at higher CeONP doses, whereas IL-10 expression declined at the highest doses. It suggests there may be an optimal dose of CeONP that can yield the most effective immunomodulation of activated macrophages, which is supported by the findings of previous studies.^{25, 51} It also implies that CeONP can reduce macrophage polarization towards M1-like macrophages, which can secrete both excessive amounts of reactive species and pro-inflammatory cytokines, and promote polarization towards M2-like macrophages, which can regulate inflammation and promote wound healing by secreting anti-inflammatory cytokine.⁵²

In our animal model, we initially observed a significant elevation in TNF α and IL-1 β secretion in the inflamed paw from CFA injection, as previously demonstrated.³² Mainly produced by macrophages, these pro-inflammatory cytokines are key participants in the

increase in vessel permeability, edema formation and oxidative stress at the inflammation site.⁵³ Our results suggest that CeONP can alleviate these key processes in acute inflammatory response *via* suppression of the pro-inflammatory cytokines. Another important development in acute inflammation is rapid recruitment of circulating monocytes, which is well-known to be facilitated by ROS.⁵⁴ Activation of these recruited monocytes transforms them into CD68-positive macrophages, which contribute to the inflammatory responses *via* removal of apoptotic cells.⁵⁵ However, excessive activation of the macrophages at the inflammation site can cause collateral damage to healthy tissue, necrosis and fibrosis. Since the phagocytic activity of macrophages is significantly affected by mitochondrial or intracellular ROS, ROS scavenging activities of CeONP can have therapeutic benefits in decreasing lesion development by moderating pro-inflammatory cytokine secretion and reducing macrophage recruitment.⁵⁶ Modulation of pro-inflammatory cytokines also can lead to the alleviation in pain hypersensitivity, as both ROS and pro-inflammatory cytokines are known to be involved in the process of pathological pain.⁵⁷

In assessment of the safety of CeONP, effective renal clearance and biocompatible surface coating of CeONP led to no detection of any adverse effects as demonstrated by histological analyses and observation of stable body weight. Rapid and efficient renal clearance of CeONP can also reduce long-term cytotoxicity concern and increase the translational potential of the nanoparticle formulation. The importance of size, surface chemistry, coating integrity in nanoparticle toxicity is emphasized as nanoparticle toxicity is heavily dependent on its physiochemical properties.⁵⁸ Our findings suggest that citric acid coated CeONP can be biocompatible and highly tolerable even at a high

injection dose (100 mg/kg). However, more extensive studies are needed in future to further prove their clearance and safety, as is standard for approval of a new agent.

While the clearance of CeONP has been demonstrated in this study, more extensive studies on the safety and clearance of our nanoparticles will need to be performed, such as at multiple timepoints out to a month or longer and in larger animal models than mice. Monitoring of organ functions *via* blood markers (e.g., AST and ALT blood levels for liver function assessment), especially for the liver where we observed the highest nanoparticle accumulation will need to be further examined for a prolonged period of time. Treatment dose is another important parameter to consider in evaluating the safety of CeONP. Previous reports of CeONP formulations with poor particle stability and renal clearance have shown that they can cause organ damages when injected at high doses.^{59, 60} Although the rapid clearance and stable coating integrity of our CeONP formulation resulted in no noticeable toxicity issues from the treatment, optimal dose regimen and administration route can further improve the safety profile while preserving the immunomodulatory effects in acute inflammation. It is also expected that potential adverse effects from ROS scavenging activities in non-target areas will be minimal as their catalytic activity is limited by the low oxygen concentration inside our body, scavenging free radicals only when they are elevated.⁵¹ Furthermore, significant amounts of CeONP accumulated at the inflammation site despite the lack of active targeting moieties,.

The close connection between oxidative stress and inflammation has led to numerous studies that also have reported immunomodulatory effects of nanozymes in treatment of inflammatory diseases.^{61, 62} The potent modulation of immune response in acute inflammation shown in our study also encourages the use of CeONP for treatment of diseases affected by chronic inflammation, such as autoimmune diseases, rheumatoid

arthritis, chronic open wounds, and atherosclerosis. For effective management of such diseases, the timing of CeONP therapy is expected to be vital in addition to dose and administration route. The efficacy of antioxidant treatment in the onset and the advanced forms of chronic inflammation will also need to be investigated.

Apart from therapeutic efficacy and safety profile of citric acid coated CeONP, our phantom imaging results suggest that CeONP can be promising CT contrast agents that can generate higher CT contrast than iodinated contrast agents in all tube potential settings. CeONP also produced higher CT attenuation when compared to gold nanoparticles in lower tube potential settings, ranging from 80 to 120 kVp. Combined with their ability to accumulate at the inflammation site, CeONP can potentially be used for target imaging of inflammatory diseases.

4.6 Conclusion

In this study, we synthesized ultras-small CeONP with strong antioxidant properties that can be used for immunomodulation of inflammatory response. These nanoparticles were efficient in ROS scavenging and suppression of inflammatory cytokine secretion in macrophages *in vitro*, which translated to reduction in edema, suppression of macrophage recruitment and alleviation of pain hypersensitivity *in vivo*. They were also biocompatible and showed rapid excretion from the body to reduce the long-term toxicity concern. Our findings demonstrate that CeONP are highly promising material for effective modulation of immune response with higher potential for clinical translation.

4.7 References

1. Tan, H. Y.; Wang, N.; Li, S.; Hong, M.; Wang, X.; Feng, Y., The reactive oxygen species in macrophage polarization: reflecting its dual role in progression and treatment of human diseases. *Oxid Med Cell Longev* **2016**, *2016*, 2795090.
2. Rzigalinski, B. A.; Carfagna, C. S.; Ehrich, M., Cerium oxide nanoparticles in neuroprotection and considerations for efficacy and safety. *Wiley Interdiscip Rev Nanomed Nanobiotechnol* **2017**, *9* (4).
3. Grulke, E.; Reed, K.; Beck, M.; Huang, X.; Cormack, A.; Seal, S., Nanocerium: factors affecting its pro- and anti-oxidant properties. *Environ Sci Nano* **2014**, *1* (5), 429-444.
4. Mittal, M.; Siddiqui, M. R.; Tran, K.; Reddy, S. P.; Malik, A. B., Reactive oxygen species in inflammation and tissue injury. *Antioxid Redox Signal* **2014**, *20* (7), 1126-1167.
5. Hussain, T.; Tan, B.; Yin, Y.; Blachier, F.; Tossou, M. C.; Rahu, N., Oxidative stress and inflammation: what polyphenols can do for us? *Oxid Med Cell Longev* **2016**, *2016*, 7432797.
6. Vaziri, N. D.; Rodriguez-Iturbe, B., Mechanisms of disease: oxidative stress and inflammation in the pathogenesis of hypertension. *Nat Clin Pract Nephrol* **2006**, *2* (10), 582-593.
7. Liang, M.; Yan, X., Nanozymes: from new Concepts, mechanisms, and standards to applications. *Acc Chem Res* **2019**, *52* (8), 2190-2200.
8. Zhang, D. Y.; Liu, H.; Li, C.; Younis, M. R.; Lei, S.; Yang, C.; Lin, J.; Li, Z.; Huang, P., Cerium nanozymes with preferential renal uptake for acute kidney injury alleviation. *ACS Appl Mater Interfaces* **2020**, *12* (51), 56830-56838.

9. Naha, P. C.; Hsu, J. C.; Kim, J.; Shah, S.; Bouche, M.; Si-Mohamed, S.; Rosario-Berrios, D. N.; Douek, P.; Hajfathalian, M.; Yasini, P.; Singh, S.; Rosen, M. A.; Morgan, M. A.; Cormode, D. P., Dextran-coated cerium oxide nanoparticles: a computed tomography contrast agent for imaging the gastrointestinal tract and inflammatory bowel disease. *ACS Nano* **2020**, *14* (8), 10187-10197.
10. Jansman, M. M. T.; Liu, X.; Kempen, P.; Clergeaud, G.; Andresen, T. L.; Thulstrup, P. W.; Hosta-Rigau, L., Hemoglobin-based oxygen carriers incorporating nanozymes for the depletion of reactive oxygen species. *ACS Appl Mater Interfaces* **2020**, *12* (45), 50275-50286.
11. Pinna, A.; Toriki Baghbaderani, M.; Vigil Hernandez, V.; Naruphontjirakul, P.; Li, S.; McFarlane, T.; Hachim, D.; Stevens, M. M.; Porter, A. E.; Jones, J. R., Nanoceria provides antioxidant and osteogenic properties to mesoporous silica nanoparticles for osteoporosis treatment. *Acta Biomater* **2021**, *122*, 365-376.
12. Bao, Q.; Hu, P.; Xu, Y.; Cheng, T.; Wei, C.; Pan, L.; Shi, J., Simultaneous blood-brain barrier crossing and protection for stroke treatment based on edaravone-loaded ceria nanoparticles. *ACS Nano* **2018**, *12* (7), 6794-6805.
13. Choi, S. W.; Cha, B. G.; Kim, J., Therapeutic contact lens for scavenging excessive reactive oxygen species on the ocular surface. *ACS Nano* **2020**, *14* (2), 2483-2496.
14. Dutta, P.; Pal, S.; Seehra, M. S.; Shi, Y.; Eyring, E. M.; Ernst, R. D., Concentration of Ce³⁺ and oxygen vacancies in cerium oxide nanoparticles. *Chem Mater* **2006**, *18* (21), 5144-5146.

15. Aneggi, E.; Boaro, M.; Leitenburg, C. d.; Dolcetti, G.; Trovarelli, A., Insights into the redox properties of ceria-based oxides and their implications in catalysis. *J Alloys Compd* **2006**, 408-412, 1096-1102.
16. Korsvik, C.; Patil, S.; Seal, S.; Self, W. T., Superoxide dismutase mimetic properties exhibited by vacancy engineered ceria nanoparticles. *Chem Commun* **2007**, (10), 1056-1058.
17. Izu, N.; Shin, W.; Matsubara, I.; Murayama, N., Development of resistive oxygen sensors based on cerium oxide thick film. *J Electroceramics* **2004**, 13 (1), 703-706.
18. Eguchi, K.; Setoguchi, T.; Inoue, T.; Arai, H., Electrical properties of ceria-based oxides and their application to solid oxide fuel cells. *Solid State Ion* **1992**, 52 (1), 165-172.
19. Dao, N. N.; Luu, M. D.; Nguyen, Q. K.; Kim, B. S., UV absorption by cerium oxide nanoparticles/epoxy composite thin films. *Nanosci and Nanotechnol* **2011**, 2 (4), 045013.
20. Kwon, H. J.; Kim, D.; Seo, K.; Kim, Y. G.; Han, S. I.; Kang, T.; Soh, M.; Hyeon, T., Ceria nanoparticle systems for selective scavenging of mitochondrial, intracellular, and extracellular reactive oxygen species in parkinson's disease. *Angew Chem Int Ed Engl* **2018**, 57 (30), 9408-9412.
21. Kwon, H. J.; Cha, M. Y.; Kim, D.; Kim, D. K.; Soh, M.; Shin, K.; Hyeon, T.; Mook-Jung, I., Mitochondria-targeting ceria nanoparticles as antioxidants for alzheimer's disease. *ACS Nano* **2016**, 10 (2), 2860-2870.
22. Jeong, H. G.; Cha, B. G.; Kang, D. W.; Kim, D. Y.; Yang, W.; Ki, S. K.; Kim, S. I.; Han, J.; Kim, C. K.; Kim, J.; Lee, S. H., Ceria nanoparticles fabricated with 6-aminohexanoic acid that overcome systemic inflammatory response syndrome. *Adv Healthc Mater* **2019**, 8 (9), e1801548.

23. Park, I. S.; Mahapatra, C.; Park, J. S.; Dashnyam, K.; Kim, J. W.; Ahn, J. C.; Chung, P. S.; Yoon, D. S.; Mandakhbayar, N.; Singh, R. K.; Lee, J. H.; Leong, K. W.; Kim, H. W., Revascularization and limb salvage following critical limb ischemia by nanoceria-induced Ref-1/APE1-dependent angiogenesis. *Biomaterials* **2020**, *242*, 119919.
24. Kim, C. K.; Kim, T.; Choi, I. Y.; Soh, M.; Kim, D.; Kim, Y. J.; Jang, H.; Yang, H. S.; Kim, J. Y.; Park, H. K.; Park, S. P.; Park, S.; Yu, T.; Yoon, B. W.; Lee, S. H.; Hyeon, T., Ceria nanoparticles that can protect against ischemic stroke. *Angew Chem Int Ed Engl* **2012**, *51* (44), 11039-11043.
25. Ni, D.; Wei, H.; Chen, W.; Bao, Q.; Rosenkrans, Z. T.; Barnhart, T. E.; Ferreira, C. A.; Wang, Y.; Yao, H.; Sun, T.; Jiang, D.; Li, S.; Cao, T.; Liu, Z.; Engle, J. W.; Hu, P.; Lan, X.; Cai, W., Ceria nanoparticles meet hepatic ischemia-reperfusion injury: the perfect imperfection. *Adv Mater* **2019**, *31* (40), e1902956.
26. Heckert, E. G.; Karakoti, A. S.; Seal, S.; Self, W. T., The role of cerium redox state in the SOD mimetic activity of nanoceria. *Biomaterials* **2008**, *29* (18), 2705-2709.
27. Karakoti, A.; Singh, S.; Dowding, J. M.; Seal, S.; Self, W. T., Redox-active radical scavenging nanomaterials. *Chem Soc Rev* **2010**, *39* (11), 4422-4432.
28. Celardo, I.; Pedersen, J. Z.; Traversa, E.; Ghibelli, L., Pharmacological potential of cerium oxide nanoparticles. *Nanoscale* **2011**, *3* (4), 1411-1420.
29. Hsu, J. C.; Cruz, E. D.; Lau, K. C.; Bouche, M.; Kim, J.; Maidment, A. D. A.; Cormode, D. P., Renally excretable and size-tunable silver sulfide nanoparticles for dual-energy mammography or computed tomography. *Chem Mater* **2019**, *31* (19), 7845-7854.

30. Choi, H. S.; Liu, W.; Misra, P.; Tanaka, E.; Zimmer, J. P.; Ipe, B.; Bawendi, M. G.; Frangioni, J. V., Renal clearance of quantum dots. *Nat Biotechnol* **2007**, *25* (10), 1165-1170.
31. Kim, J.; Silva, A. B.; Hsu, J. C.; Maidment, P. S. N.; Shapira, N.; Noel, P. B.; Cormode, D. P., Radioprotective garment-inspired biodegradable polymetal nanoparticles for enhanced CT contrast production. *Chem Mater* **2020**, *32* (1), 381-391.
32. Chen, L.; Yang, G.; Cormode, D. P.; Saigal, A.; Madhavan, S.; Mazaleuskaya, L. L.; Grant, G. R.; FitzGerald, G. A.; Grosser, T., Myeloid cell mPGES-1 mediates inflammatory pain hypersensitivity in mice. *bioRxiv* **2020**, 929422.
33. Lee, S. S.; Song, W.; Cho, M.; Puppala, H. L.; Nguyen, P.; Zhu, H.; Segatori, L.; Colvin, V. L., Antioxidant properties of cerium oxide nanocrystals as a function of nanocrystal diameter and surface coating. *ACS Nano* **2013**, *7* (11), 9693-9703.
34. Heckman, K. L.; DeCoteau, W.; Estevez, A.; Reed, K. J.; Costanzo, W.; Sanford, D.; Leiter, J. C.; Clauss, J.; Knapp, K.; Gomez, C.; Mullen, P.; Rathbun, E.; Prime, K.; Marini, J.; Patchefsky, J.; Patchefsky, A. S.; Hailstone, R. K.; Erlichman, J. S., Custom cerium oxide nanoparticles protect against a free radical mediated autoimmune degenerative disease in the brain. *ACS Nano* **2013**, *7* (12), 10582-10596.
35. Patel, U.; Chauhan, K.; Gupte, S., Synthesis, characterization and application of lipase-conjugated citric acid-coated magnetic nanoparticles for ester synthesis using waste frying oil. *3 Biotech* **2018**, *8* (4), 211.
36. Samavini, R.; Sandaruwan, C.; De Silva, M.; Priyadarshana, G.; Kottegoda, N.; Karunaratne, V., Effect of citric acid surface modification on solubility of hydroxyapatite nanoparticles. *J Agric Food Chem* **2018**, *66* (13), 3330-3337.

37. Kanzaki, H.; Wada, S.; Narimiya, T.; Yamaguchi, Y.; Katsumata, Y.; Itohiya, K.; Fukaya, S.; Miyamoto, Y.; Nakamura, Y., Pathways that regulate ROS scavenging enzymes, and their role in defense against tissue destruction in periodontitis. *Front Physiol* **2017**, *8*, 351.
38. Lu, Y. C.; Yeh, W. C.; Ohashi, P. S., LPS/TLR4 signal transduction pathway. *Cytokine* **2008**, *42* (2), 145-151.
39. Hsu, H. Y.; Wen, M. H., Lipopolysaccharide-mediated reactive oxygen species and signal transduction in the regulation of interleukin-1 gene expression. *J Biol Chem* **2002**, *277* (25), 22131-22139.
40. Park, H. S.; Jung, H. Y.; Park, E. Y.; Kim, J.; Lee, W. J.; Bae, Y. S., Cutting edge: direct interaction of TLR4 with NAD(P)H oxidase 4 isozyme is essential for lipopolysaccharide-induced production of reactive oxygen species and activation of NF-kappa B. *J Immunol* **2004**, *173* (6), 3589-3593.
41. Korhonen, R.; Lahti, A.; Kankaanranta, H.; Moilanen, E., Nitric oxide production and signaling in inflammation. *Curr Drug Targets Inflamm Allergy* **2005**, *4* (4), 471-479.
42. Li, H.; Horke, S.; Forstermann, U., Vascular oxidative stress, nitric oxide and atherosclerosis. *Atherosclerosis* **2014**, *237* (1), 208-219.
43. Bulua, A. C.; Simon, A.; Maddipati, R.; Pelletier, M.; Park, H.; Kim, K.-Y.; Sack, M. N.; Kastner, D. L.; Siegel, R. M., Mitochondrial reactive oxygen species promote production of proinflammatory cytokines and are elevated in TNFR1-associated periodic syndrome (TRAPS). *J Exp Med* **2011**, *208* (3), 519-533.
44. Zhang, J. M.; An, J., Cytokines, inflammation, and pain. *Int Anesthesiol Clin* **2007**, *45* (2), 27-37.

45. Loynachan, C. N.; Soleimany, A. P.; Dudani, J. S.; Lin, Y.; Najer, A.; Bekdemir, A.; Chen, Q.; Bhatia, S. N.; Stevens, M. M., Renal clearable catalytic gold nanoclusters for *in vivo* disease monitoring. *Nat Nanotechnol* **2019**, *14* (9), 883-890.
46. Yu, M.; Xu, J.; Zheng, J., Renal clearable luminescent gold nanoparticles: from the bench to the clinic. *Angew Chem Int Ed Engl* **2019**, *58* (13), 4112-4128.
47. Liu, J.; Yu, M.; Zhou, C.; Zheng, J., Renal clearable inorganic nanoparticles: a new frontier of bionanotechnology. *Mater Today* **2013**, *16* (12), 477-486.
48. Filewod, N. C.; Lee, W. L., Inflammation without vascular leakage. science fiction no longer? *Am J Respir Crit Care Med* **2019**, *200* (12), 1472-1476.
49. de Sousa, M. E.; Fernández van Raap, M. B.; Rivas, P. C.; Mendoza Zélis, P.; Girardin, P.; Pasquevich, G. A.; Alessandrini, J. L.; Muraca, D.; Sánchez, F. H., Stability and relaxation mechanisms of citric acid coated magnetite nanoparticles for magnetic hyperthermia. *J Phys Chem C* **2013**, *117* (10), 5436-5445.
50. Kohchi, C.; Inagawa, H.; Nishizawa, T.; Soma, G., ROS and innate immunity. *Anticancer Res* **2009**, *29* (3), 817-821.
51. Casals, E.; Zeng, M.; Parra-Robert, M.; Fernandez-Varo, G.; Morales-Ruiz, M.; Jimenez, W.; Puentes, V.; Casals, G., Cerium oxide nanoparticles: advances in biodistribution, toxicity, and preclinical exploration. *Small* **2020**, *16* (20), e1907322.
52. Atri, C.; Guerfali, F. Z.; Laouini, D., Role of human macrophage polarization in inflammation during infectious diseases. *Int J Mol Sci* **2018**, *19* (6).
53. Zelova, H.; Hosek, J., TNF-alpha signalling and inflammation: interactions between old acquaintances. *Inflamm Res* **2013**, *62* (7), 641-651.

54. Hackel, D.; Pflucke, D.; Neumann, A.; Viebahn, J.; Mousa, S.; Wischmeyer, E.; Roewer, N.; Brack, A.; Rittner, H. L., The connection of monocytes and reactive oxygen species in pain. *PLoS One* **2013**, *8* (5), e63564.
55. Kang, D.-W.; Kim, C. K.; Jeong, H.-G.; Soh, M.; Kim, T.; Choi, I.-Y.; Ki, S.-K.; Kim, D. Y.; Yang, W.; Hyeon, T.; Lee, S.-H., Biocompatible custom ceria nanoparticles against reactive oxygen species resolve acute inflammatory reaction after intracerebral hemorrhage. *Nano Res* **2017**, *10* (8), 2743-2760.
56. Forrester, S. J.; Kikuchi, D. S.; Hernandez, M. S.; Xu, Q.; Griendling, K. K., Reactive oxygen species in metabolic and inflammatory signaling. *Circ Res* **2018**, *122* (6), 877-902.
57. Vanderwall, A. G.; Milligan, E. D., Cytokines in pain: harnessing endogenous anti-inflammatory signaling for improved pain management. *Front Immunol* **2019**, *10*, 3009.
58. Sukhanova, A.; Bozrova, S.; Sokolov, P.; Berestovoy, M.; Karaulov, A.; Nabiev, I., Dependence of nanoparticle toxicity on their physical and chemical properties. *Nanoscale Res Lett* **2018**, *13* (1), 44.
59. Ma, J. Y.; Mercer, R. R.; Barger, M.; Schwegler-Berry, D.; Scabilloni, J.; Ma, J. K.; Castranova, V., Induction of pulmonary fibrosis by cerium oxide nanoparticles. *Toxicol Appl Pharmacol* **2012**, *262* (3), 255-264.
60. Tseng, M. T.; Lu, X.; Duan, X.; Hardas, S. S.; Sultana, R.; Wu, P.; Unrine, J. M.; Graham, U.; Butterfield, D. A.; Grulke, E. A.; Yokel, R. A., Alteration of hepatic structure and oxidative stress induced by intravenous nanoceria. *Toxicol Appl Pharmacol* **2012**, *260* (2), 173-182.

61. Hirst, S. M.; Karakoti, A. S.; Tyler, R. D.; Sriranganathan, N.; Seal, S.; Reilly, C. M., Anti-inflammatory properties of cerium oxide nanoparticles. *Small* **2009**, *5* (24), 2848-2856.
62. Selvaraj, V.; Nepal, N.; Rogers, S.; Manne, N. D.; Arvapalli, R.; Rice, K. M.; Asano, S.; Fankhanel, E.; Ma, J. J.; Shokuhfar, T.; Maheshwari, M.; Blough, E. R., Inhibition of MAP kinase/NF- κ B mediated signaling and attenuation of lipopolysaccharide induced severe sepsis by cerium oxide nanoparticles. *Biomaterials* **2015**, *59*, 160-171.

CHAPTER 5: LABELING SOLID TUMOR TARGETING CAR-T CELLS FOR CT AND SPCCT CELL TRACKING IN CANCER IMMUNOTHERAPY

5.1 Abstract

The clinical success of FDA-approved CAR-T cell therapies against hematologic malignancies has created substantial interest in further improving their safety and efficacy as well as in developing new CAR-T cell therapies for solid tumor treatment. While there have been some promising results, most clinical trials to date report severe toxicities, poor tumor specificity and limited persistence. A method that can directly monitor the administered CAR-T cells can greatly facilitate the development of new CAR-T cell therapies by providing information on cell biodistribution and persistence. In this study, we labeled primary human CAR-T cells with gold nanoparticles (AuNP) to allow monitoring of the CAR-T cells with both CT and photon-counting CT (SPCCT) imaging. We found that our labeling method that utilizes a commercially available transfection reagent can promote sufficient internalization of AuNP by CAR-T cells without significantly affecting their *viability* and main cellular functions. We also demonstrate that the cellular uptake of AuNP by CAR-T cells was sufficient to visualize the labeled cells in both CT and SPCCT imaging.

5.2 Introduction

Chimeric antigen receptor (CAR)-T cell therapy has resulted in unprecedented clinical responses in patients with certain forms of hematologic malignancies.^{1, 2} Recent FDA approvals of CD19-targeting CAR-T cells and their subsequent clinical successes have motivated a plethora of studies to develop CAR-T cell therapies with improved efficacy and safety. One of the main directions of these CAR-T cell therapies is to develop them for solid tumor treatment. Numerous approaches are under clinical investigation to achieve this, such as new CAR designs and the use of new tumor antigens.³⁻⁶ The safety and feasibility of these innovative CAR-T cell therapies are being demonstrated in some studies.⁷⁻¹⁰ However, despite the recent advances, solid tumor treatment remains challenging as solid tumors present additional hurdles, such as lack of antigens that are truly tumor-specific and immunosuppressive tumor microenvironments. To develop CAR-T cell therapies with desirable therapeutic efficacy and safety, many aspects of CAR-T cells, such as their trafficking, persistence, and target tumor specificity, need to be closely examined. However, these vital parameters, especially the full extent of CAR-T cell biodistribution, are often poorly understood, and conventional monitoring methods from biopsies and biomarker analyses only provide indirect information on such parameters. Therefore, a reliable method to track and monitor infused CAR-T cells *in vivo* will provide invaluable insights and facilitate the progression of CAR-T cell therapy in solid tumor treatment.

X-ray computed tomography (CT) could be used to track labeled CAR-T cells in a non-invasive and real-time manner. Our group has previously demonstrated the feasibility of monitoring the recruitment of monocytes that are labeled with gold nanoparticles (AuNP) to atherosclerotic plaques with CT imaging.¹¹ Furthermore, we have recently

demonstrated for the first time that spectral photon-counting CT (SPCCT), a new CT technology under clinical development, can specifically detect macrophages labeled with AuNP *in vivo*.¹² The AuNP signals from the SPCCT system were also linearly correlated with AuNP biodistribution determined by analytical tools, allowing accurate quantification of the AuNP labels, and therefore, the number of localized cells.^{13, 14} Moreover, we also found that SPCCT can detect AuNP accumulation in the bone marrow,¹³ which serves as a marker of the persistence in patient response to CAR-T cell therapies. All of these features are highly attractive in CAR-T cell monitoring, allowing specific visualization of the labeled cells and analyses of biodistribution and patient response at multiple time points without tumor resection.

Herein, we develop a labeling method to track CAR-T cells with both CT and SPCCT imaging in an effort to facilitate the advancement of novel CAR-T cell therapy for solid tumor treatment with better monitoring of infused cell behaviors. We demonstrate that small AuNP encapsulated in lipid-based transfection reagent can be used for labeling CAR-T cells without significant effects on the cell *viability* and functions and can allow visualization of the labeled CAR-T cells in CT and SPCCT imaging.

5.3 Materials and methods

5.3.1 Materials

Gold(III) chloride trihydrate (>99.9% trace metals basis) was purchased from Sigma-Aldrich (St. Louis, MO). Lipofectamine 2000 transfection reagent, human T-activator CD3/CD28 Dynabeads, LIVE/DEAD assay kits were acquired from Life Technologies (Grand Island, NY). Primary human CAR-T cells were a gift from Avery Posey's lab at the University of Pennsylvania.

5.3.2 Gold nanoparticle transfection agent synthesis

Glutathione-coated, sub-5 nm AuNP were synthesized by the same method used in Chapter 3. Briefly, gold(III) chloride salt in water was reduced by dropwise addition of sodium borohydride solution, and 10 mg of glutathione was subsequently added to the solution after 30 minutes. The resulting solution was washed in deionized water by centrifugation in molecular cut-off centrifugation tubes. Immediately before labeling the cells, AuNP of desired concentration was mixed with lipofectamine (mass ratio of 6:1).

5.3.3 Nanoparticle characterization

Transmission electron microscopy (TEM) was used to determine the core sizes and morphologies of glutathione-coated small AuNP and lipofectamine-encapsulated AuNP. The images were acquired using a Tecnai T12 microscope (FEI, Hillsboro, OR) or a JEOL 1010 microscope (JEOL Ltd., Japan).

5.3.4 CAR-T cell culture and labeling

Primary human CAR-T cells were cultured in RPMI media supplemented with 30 U/ml of IL-2. After thawing, the cells were allowed to be activated by adding CD3/CD28 Dynabeads in 1:1 bead-to-cell ratio. The activated cells were expanded by adding extra volume of media to maintain the cell density at 1×10^6 cells/ml. To label the cells, AuNP that were encapsulated by lipofectamine was added to CAR-T cells (2×10^6 cells in 6-well plate) immediately after the mixing step in section 4.3.2.

5.3.5 Cellular uptake

The amounts of internalized AuNP in CAR-T cells were assessed by collecting labeled CAR-T cells and performing ICP-OES analysis. CAR-T cells were collected in a pellet by centrifuging at 160 x g for 5 minutes. The cell pellet was then digested in aqua regia for gold measurement by ICP-OES.

5.3.6 *In vitro* viability and CAR-T cell function assays

The LIVE/DEAD assay was performed using the same method described in earlier chapters. Tumor cytotoxicity and cytokine production of Jurkat E6-1 cell targeting 5E5 CAR-T cells were tested before and after AuNP labeling. For cytotoxicity assays, 1×10^5 tumor cells were seeded in 48-well plates, and after 24 hours, different amounts of CAR-T cells were added (effector/target ratio ranging from 0.25 to 3:1). For cytokine production assays, supernatants were collected 24 hours after the co-culture to analyze the production levels of CD107a, TNF α , IL-2, BzmB and IFN γ using the human cytokine 30-plex panel on the Luminex system (Thermo Fisher Scientific) and DuoSet ELISA Development Kit (R&D Systems).¹⁵ For both assays, CD19 targeting CAR-T cells were used as a control.

5.3.7 CT and SPCCT phantom imaging of labeled CAR-T cells

AuNP-labeled CAR-T cells were collected as pellets at the bottom of 1.5 ml microcentrifuge tubes for *in vitro* phantom imaging in a SOMATOM Force clinical CT system (Siemens Healthineers, Germany) and a MARS-12 v.5 commercially-available preclinical spectral CT system (MARS Bioimaging Ltd., New Zealand) located at the University of Notre Dame.

5.4 Results

5.4.1 CAR-T cell transfecting gold nanoparticle synthesis and characterization

Small AuNP were synthesized and capped with glutathione that can provide stability in biological fluids and render negative surface potential to allow facile encapsulation in the lipofectamine transfection reagent, which consists of cationic lipids that can form liposomes and other lipid-based structures. As shown in Figure 5.1A, glutathione-capped small AuNP were uniform in size and spherical in morphologies. Upon mixing with lipofectamine in hydrophilic conditions, AuNP were successfully complexed with the transfection reagent to form large lipid-coated structures (Figure 5.1B).

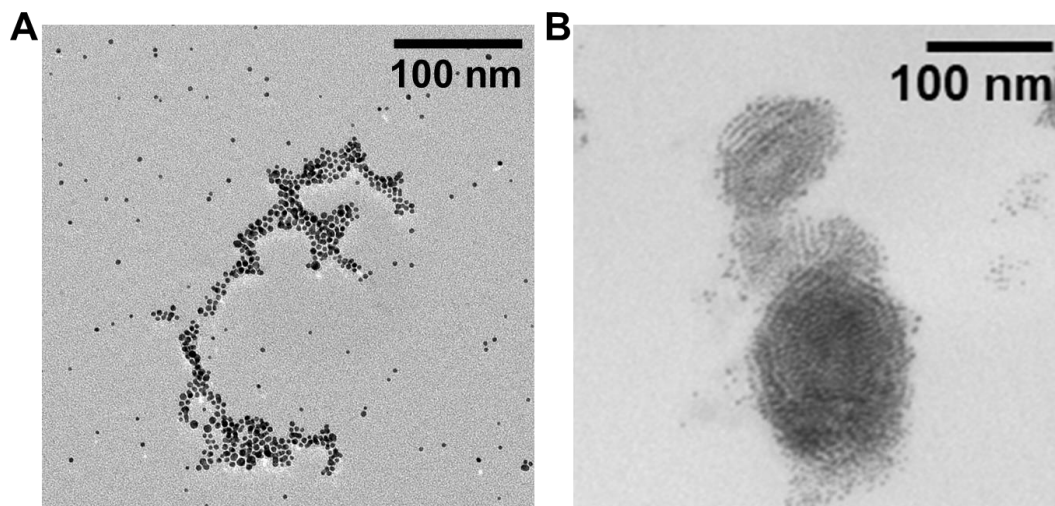


Figure 5.1 Morphologies of small AuNP and lipofectamine-encapsulated AuNP.

TEM of A) small AuNP and B) AuNP encapsulated in lipofectamine transfection reagent.

5.4.2 Selection of CAR-T cell labeling conditions

We treated CAR-T cells with lipofectamine-coated AuNP to label the cells. We assessed both *viability* and AuNP uptake by CAR-T cells after treating the cells with a range of concentrations (0.05, 0.1 and 0.25 mg Au/ml) and duration (1, 8, 24 hours) to

select a treatment condition that yields the highest cellular uptake without significant disruption in CAR-T cell *viability*. As shown in Figure 5.2A, the cellular uptake of AuNP were heavily dependent on AuNP treatment concentration, resulting in higher cellular uptake with increasing treatment concentration. The treatment duration did not noticeably affect the uptake; however, it greatly affected the CAR-T cell *viability*. At 1 hr of treatment, cell *viability* was not reduced significantly when compared to the control (no AuNP treatment) across all treatment concentrations (Figure 5.2B). Numbers of *viable* CAR-T cells started to diminish at longer treatment times, resulting in a significant reduction in *viability* in treatment concentrations of 0.1 and 0.25 mg Au/ml at 24 hr of treatment. With both AuNP uptake and cell *viability* in consideration, we decided that the best treatment condition for our primary human CAR-T cells is the treatment concentration of 0.25 mg Au/ml and duration of 1 hour. We used this labeling condition for further studies.

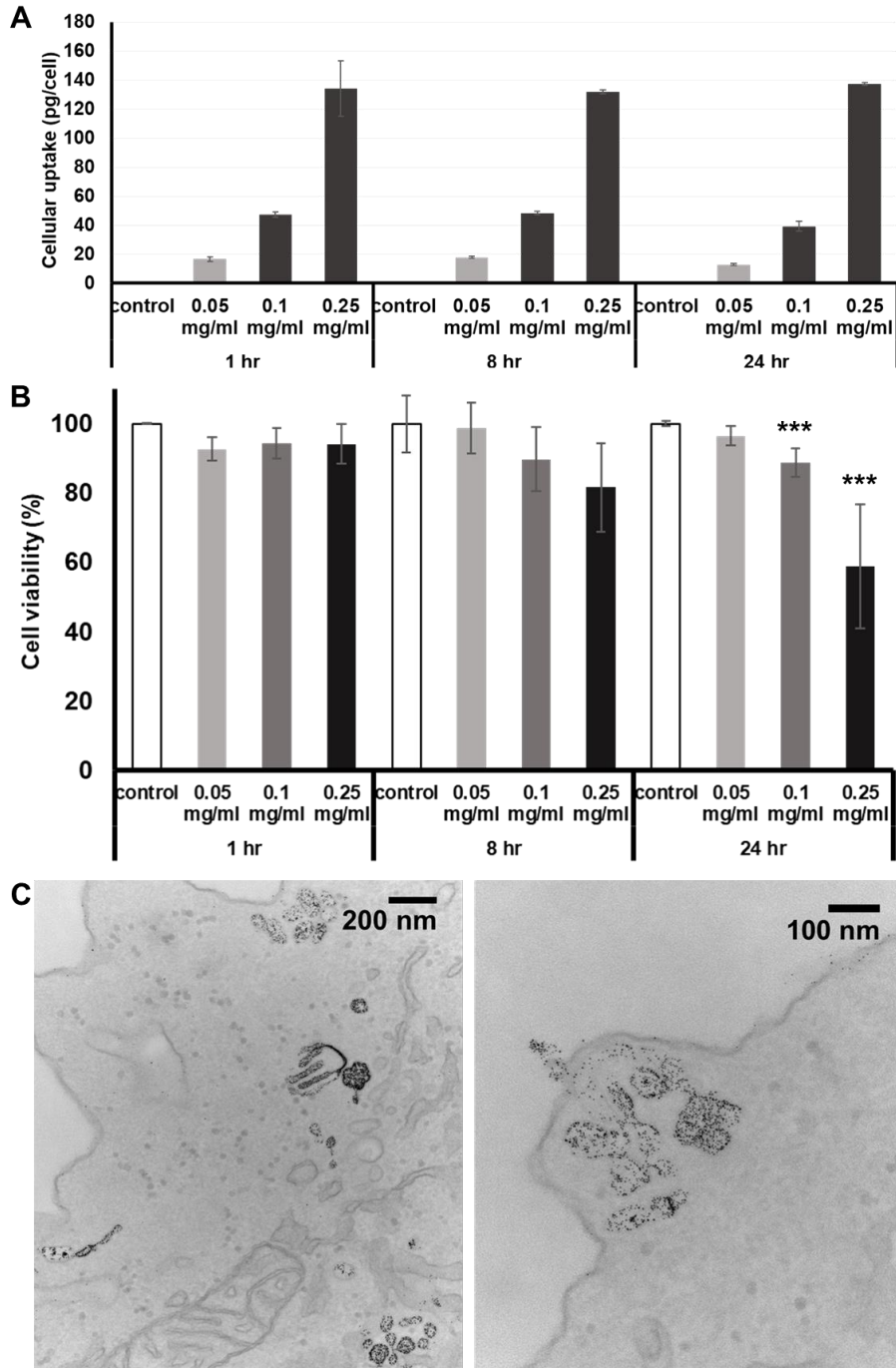


Figure 5.2 Labeling of AuNP and its effect in CAR-T cell *viability*

A) AuNP uptake by CAR-T cells at varying treatment concentrations and durations. B) *In vitro* cell *viability* of AuNP-labeled CAR-T cells. C) TEM of AuNP-labeled CAR-T cells.

5.4.3 *In vitro* cellular functions

To confirm that the AuNP labeling conditions do not affect the main CAR-T cell functions in cancer immunotherapy, we assessed the cells' cytotoxicity against their target tumor cells and inflammatory cytokine production. As shown in Figure 5.3A, both labeled and unlabeled Jurkat E6-1 cell targeting 5E5 CAR-T cells had nearly 100 % tumor lysis level across all effector to target cell ratios. Moreover, both labeled and unlabeled CD19-targeting CAR-T cells did not actively bind to Jurkat E6-1 CAR-T cells had low lytic effects. AuNP labeling also did not affect the cytokine production of 5E5 CAR-T cells, demonstrated by similar cytokine production profiles of important cytokines, such as TNF α and IL-2, between labeled and unlabeled cells (Figure 5.3B).

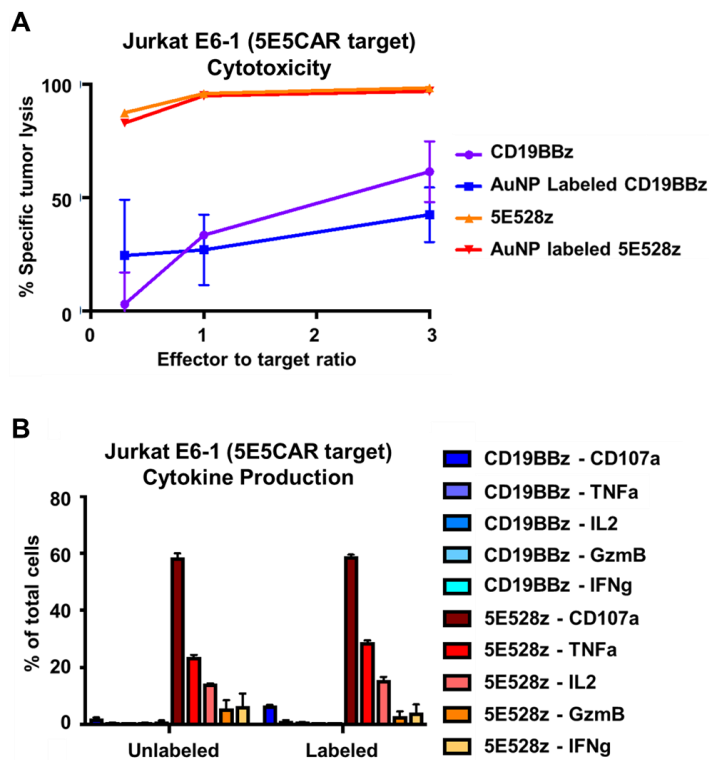


Figure 5.3 Cellular functions of labeled CAR-T cells

Effect of AuNP labeling on the A) cytotoxicity of CAR-T cells against target tumor cells and B) cytokine production.

5.4.4 *In vitro* CT and SPCCT phantom imaging of labeled CAR-T cells

We assessed CT contrast production of labeled cell pellets in CT imaging and material differentiation in SPCCT imaging to ensure that CAR-T cells were labeled with sufficient amount of gold payload to allow visualization in CT- and SPCCT-based cell tracking. CT imaging of CAR-T cells labeled with 0.25 mg/ml of AuNP for 1 hour indicated that the labeled cells can generate sufficient CT attenuation, shown by clear delineation of the cell pellet (Figure 5.4A). The cell pellets were also scanned with a preclinical SPCCT system, which showed high CT attenuation in conventional CT images. The sufficient CT contrast production also led to accurate material differentiation of gold, as depicted in gold-specific K-edge images in Figure 5.4B. We could clearly distinguish the locations of AuNP-labeled pellets in the image and also quantify the amount of AuNP at the location.

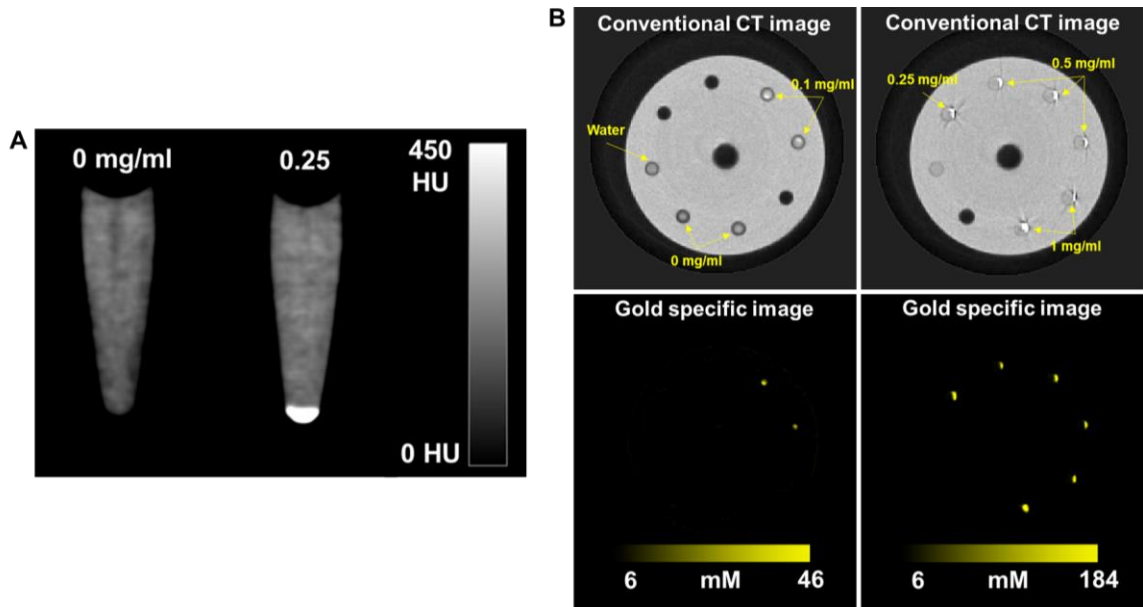


Figure 5.4 *In vitro* phantom images of labeled CAR-T cells.

Labeled cell pellet images from A) a clinical CT system and B) a preclinical SPCCT system (Top left: conventional CT-like image of tubes that contain water and labeled cell pellets from 0 and 0.1 mg/ml treatment concentration, bottom left: corresponding K-edge image, top right: conventional CT-like image of tubes that contain labeled cell pellets from 0.25, 0.5, 1 mg/ml treatment concentration, bottom right: corresponding K-edge image)

5.5 Discussion

In cell tracking applications using CT and SPCCT imaging, it is important to maximize the cellular uptake of the payload to overcome the relatively low sensitivity of CT. However, such high payloads may lead to cytotoxic effects to the labeled cells. Thus, the payload material first needs to be biocompatible and bioinert.¹⁶ As the most widely studied experimental nanoparticles-based contrast agents for CT imaging, AuNP has been known to have excellent biocompatibility as well as high elemental density, making it suitable for cell tracking application. In fact, internalization of more than 100 pg of gold per cell did not noticeably diminish the *viability* of CAR-T cells or alter their main cellular functions in our study.

In addition to the payload materials, parameters used for cell labeling, such as treatment concentration and time, also play important roles in maximizing the cellular uptake with minimal disruption of cell *viability* and functions. As suggested by our results, when using cationic transfection reagents to promote cellular uptake, short treatment times may be ideal to label non-phagocytic cells, such as CAR-T cells, as longer treatment times can lead to cell death. A range of treatment concentrations will also need to be examined as overloading the cells can cause a decrease in cell *viability* as well. These treatment parameters will need to be optimized for specific cell tracking applications as

different nanoparticle formulations will be used to label different cell types. Since the physiochemical properties of nanoparticles significantly affect the cellular interaction and internalization, cellular uptake of the nanoparticles will vary.¹⁷ Moreover, unlike CAR-T cells, cells that are phagocytic in nature (e.g., macrophages and neutrophils) can internalize much higher amounts of nanoparticles and have better tolerance to the presence of foreign materials.

The likelihood of visualizing the labeled CAR-T cells with CT and SPCCT imaging has been demonstrated by *in vitro* phantom imaging in this chapter. However, further studies are needed to confirm the feasibility of *in vivo* cell tracking, which depends on numerous parameters, such as tumor size in animal models and dose and target specificity of CAR-T cells. To maximize the potential for cell tracking, we will optimize CT imaging parameters (e.g., energy bin threshold, reconstruction algorithm and radiation dose) and treatment regimen (e.g., cell dose and administration route).

5.6 Conclusion

In this study, we discovered a AuNP formulation and a method to label CAR-T cells with sufficient amount of AuNP payload to visualize the labeled cells with CT and SPCCT imaging systems. Our labeling approach achieved this with minimal disruption in CAR-T cell *viability* and their functions.

5.7 References

1. Grupp, S. A.; Kalos, M.; Barrett, D.; Aplenc, R.; Porter, D. L.; Rheingold, S. R.; Teachey, D. T.; Chew, A.; Hauck, B.; Wright, J. F.; Milone, M. C.; Levine, B. L.; June, C. H., Chimeric antigen receptor-modified T cells for acute lymphoid leukemia. *N Engl J Med* **2013**, *368* (16), 1509-1518.
2. Maude, S. L.; Frey, N.; Shaw, P. A.; Aplenc, R.; Barrett, D. M.; Bunin, N. J.; Chew, A.; Gonzalez, V. E.; Zheng, Z.; Lacey, S. F.; Mahnke, Y. D.; Melenhorst, J. J.; Rheingold, S. R.; Shen, A.; Teachey, D. T.; Levine, B. L.; June, C. H.; Porter, D. L.; Grupp, S. A., Chimeric antigen receptor T cells for sustained remissions in leukemia. *N Engl J Med* **2014**, *371* (16), 1507-17.
3. Castellarin, M.; Watanabe, K.; June, C. H.; Kloss, C. C.; Posey, A. D., Jr., Driving cars to the clinic for solid tumors. *Gene Ther* **2018**, *25* (3), 165-175.
4. Knochelmann, H. M.; Smith, A. S.; Dwyer, C. J.; Wyatt, M. M.; Mehrotra, S.; Paulos, C. M. CAR T cells in solid tumors: blueprints for building effective therapies. *Front Immunol* **2018**, *9*, 1740.
5. Martinez, M.; Moon, E. K., CAR T cells for solid tumors: new strategies for finding, infiltrating, and surviving in the tumor microenvironment. *Front Immunol* **2019**, *10*, 128.
6. Watanabe, K.; Kuramitsu, S.; Posey, A. D., Jr.; June, C. H., Expanding the therapeutic window for CAR T cell therapy in solid tumors: the knowns and unknowns of CAR T cell biology. *Front Immunol* **2018**, *9*, 2486.
7. Ahmed, N.; Brawley, V.; Hegde, M.; Bielanowicz, K.; Kalra, M.; Landi, D.; Robertson, C.; Gray, T. L.; Diouf, O.; Wakefield, A.; Ghazi, A.; Gerken, C.; Yi, Z.; Ashoori, A.; Wu, M. F.; Liu, H.; Rooney, C.; Dotti, G.; Gee, A.; Su, J.; Kew, Y.; Baskin, D.; Zhang, Y. J.; New, P.; Grilley, B.; Stojakovic, M.; Hicks, J.; Powell, S. Z.; Brenner, M. K.; Heslop,

H. E.; Grossman, R.; Wels, W. S.; Gottschalk, S., HER2-specific chimeric antigen receptor-modified virus-specific T cells for progressive glioblastoma: a phase 1 dose-escalation trial. *JAMA Oncol* **2017**, *3* (8), 1094-1101.

8. Brown, C. E.; Alizadeh, D.; Starr, R.; Weng, L.; Wagner, J. R.; Naranjo, A.; Ostberg, J. R.; Blanchard, M. S.; Kilpatrick, J.; Simpson, J.; Kurien, A.; Priceman, S. J.; Wang, X.; Harshbarger, T. L.; D'Apuzzo, M.; Ressler, J. A.; Jensen, M. C.; Barish, M. E.; Chen, M.; Portnow, J.; Forman, S. J.; Badie, B., Regression of glioblastoma after chimeric antigen receptor T-cell therapy. *N Engl J Med* **2016**, *375* (26), 2561-9.

9. Brown, C. E.; Badie, B.; Barish, M. E.; Weng, L.; Ostberg, J. R.; Chang, W. C.; Naranjo, A.; Starr, R.; Wagner, J.; Wright, C.; Zhai, Y.; Bading, J. R.; Ressler, J. A.; Portnow, J.; D'Apuzzo, M.; Forman, S. J.; Jensen, M. C., Bioactivity and safety of IL13Ralpha2-redirected chimeric antigen receptor CD8+ T Cells in patients with recurrent glioblastoma. *Clin Cancer Res* **2015**, *21* (18), 4062-72.

10. Shah, M. H.; Lorigan, P.; O'Brien, M. E.; Fossella, F. V.; Moore, K. N.; Bhatia, S.; Kirby, M.; Woll, P. J., Phase I study of IMGN901, a CD56-targeting antibody-drug conjugate, in patients with CD56-positive solid tumors. *Invest New Drugs* **2016**, *34* (3), 290-9.

11. Chhour, P.; Naha, P. C.; O'Neill, S. M.; Litt, H. I.; Reilly, M. P.; Ferrari, V. A.; Cormode, D. P., Labeling monocytes with gold nanoparticles to track their recruitment in atherosclerosis with computed tomography. *Biomaterials* **2016**, *87*, 93-103.

12. Cuccione, E.; Chhour, P.; Si-Mohamed, S.; Dumot, C.; Kim, J.; Hubert, V.; Da Silva, C. C.; Vandamme, M.; Chereul, E.; Balegamire, J.; Chevalier, Y.; Berthezene, Y.; Bousset, L.; Douek, P.; Cormode, D. P.; Wiart, M., Multicolor spectral photon counting CT

monitors and quantifies therapeutic cells and their encapsulating scaffold in a model of brain damage. *Nanotheranostics* **2020**, 4 (3), 129-141.

13. Cormode, D. P.; Si-Mohamed, S.; Bar-Ness, D.; Sigovan, M.; Naha, P. C.; Balegamire, J.; Lavenne, F.; Coulon, P.; Roessler, E.; Bartels, M.; Rokni, M.; Blevis, I.; Bousset, L.; Douek, P., Multicolor spectral photon-counting computed tomography: *in vivo* dual contrast imaging with a high count rate scanner. *Sci Rep* **2017**, 7 (1), 4784.

14. Si-Mohamed, S.; Cormode, D. P.; Bar-Ness, D.; Sigovan, M.; Naha, P. C.; Langlois, J. B.; Chalabreysse, L.; Coulon, P.; Blevis, I.; Roessler, E.; Erhard, K.; Bousset, L.; Douek, P., Evaluation of spectral photon counting computed tomography K-edge imaging for determination of gold nanoparticle biodistribution *in vivo*. *Nanoscale* **2017**, 9 (46), 18246-18257.

15. Guedan, S.; Madar, A.; Casado-Medrano, V.; Shaw, C.; Wing, A.; Liu, F.; Young, R. M.; June, C. H.; Posey, A. D., Jr., Single residue in CD28-costimulated CAR-T cells limits long-term persistence and antitumor durability. *J Clin Investig* **2020**, 130 (6), 3087-3097.

16. Kim, J.; Chhour, P.; Hsu, J.; Litt, H. I.; Ferrari, V. A.; Popovtzer, R.; Cormode, D. P., Use of nanoparticle contrast agents for cell tracking with computed tomography. *Bioconjug Chem* **2017**, 28 (6), 1581-1597.

17. Gong, N.; Chen, S.; Jin, S.; Zhang, J.; Wang, P. C.; Liang, X.-J., Effects of the physicochemical properties of gold nanostructures on cellular internalization. *Regen Biomater* **2015**, 2 (4), 273-280.

Chapter 6: Overall discussion and future directions

6.1 Overall discussion

6.1.1 Overview

In the work presented herein, we specifically designed and synthesized various nanoparticle formulations to develop either novel CT contrast agents that can overcome the limitations of currently used iodinated small molecules or functional nanoparticles that can be used to expand CT imaging applications to targeted imaging of inflammatory diseases and cell tracking.

In chapter 2, we first screened and identified candidate elements for the development of nanoparticle-based SPCCT-specific contrast agents. We assessed CT contrast generation properties (i.e., attenuation and contrast-to-noise ratio) of the selected elements and concluded that tantalum is a suitable element to develop into SPCCT-specific contrast agents. We then demonstrated the feasibility of our conclusion by synthesizing sub-5 nm tantalum-based nanoparticles and confirming the nanoparticles' *in vitro* biocompatibility and accurate differentiation of tantalum in SPCCT imaging. We were encouraged by our findings in tantalum's high CT contrast production and *in vitro* safety and explored its development for conventional CT contrast agents.

In examination of this idea, we hypothesized that combining tantalum-based nanoparticles with nanoparticles made of other suitable elements, namely cerium and gold, can lead to production of higher CT attenuation since these elements have their K-edge energies evenly spread out in high photon flux regions of X-ray spectra used in clinical settings. In chapter 3, we were able to successfully synthesize sub-5 nm nanoparticles formulations, each made of cerium, tantalum, and gold, and encapsulate them in polymeric nanoparticles of larger sizes (can be controlled to be 50 to 500 nm). In validation

of our hypothesis, we found that the polymeric nanoparticles, or PMNP, were able to produce consistently high CT attenuation across multiple clinical settings (i.e., tube potential ranging from 80 to 140 kvP). In this study, we also observed that cerium nanoparticles were able to attenuate X-ray photons much better than AuNP, especially at low tube potentials. Concurrently, we realized that cerium has not been explored as CT contrast agents and that CeONP are actively being investigated by researchers for their antioxidant and potential anti-inflammatory properties at inflammation site.¹⁻³

Thus, we developed citric acid coated CeONP for their application in CT imaging of inflammatory diseases. In chapter 4, we examined and demonstrated their potential as CT contrast agents as well as their capabilities to modulate inflammation. Our findings in this study indicate that CeONP can be developed as theranostic agents for inflammatory diseases, enabling both CT-based diagnosis and treatment of such diseases.

As established by our CeONP work, nanoparticles can be developed to have additional functionalities to expand CT imaging applications. One CT imaging application that our group has been actively pursuing is cell tracking. Despite high CT production of CeONP and TaONP, both low elemental density of cerium and tantalum and the presence of other constituents in the core of nanoparticles limit the delivery of the payload materials into the cells of interest. For this reason, we sought to use AuNP for cell tracking of CAR-T cells in cancer immunotherapy. As shown in chapter 5, we implemented a specific labeling method for CAR-T cells with transfection reagent-associated AuNP to deliver high amounts of gold payload non-phagocytic cells. In this work, we successfully demonstrated the feasibility to promote internalization of sufficient amounts of AuNP into CAR-T cells for CT and SPCCT imaging with minimal disruption of the cell functions *in vitro*. However, more work is needed to advance this study for *in vivo* cell tracking.

Here we discuss the potential of these nanoparticle contrast agents for clinical translation and considerations to be made. We also discuss the current limitations and strategies in expanding CT imaging application in targeted imaging and cell tracking.

6.1.2 Road to clinical translation for nanoparticle-based CT and SPCCT contrast agents

Despite the advances in nanoparticle-based CT contrast agents, there has not been a formulation that has been FDA approved for this application. The biggest barrier to their clinical translation is the potential long-term toxicity from retention in the body.⁴ As we did for our nanoparticle design, the most widely adapted strategy is to develop nanoparticle formulations whose hydrodynamic diameter is less than the renal filtration threshold of approximately 5.5 nm for rapid renal clearance from the body, minimizing or even eliminating the retention. However, small nanoparticle size shortens the blood circulation time, which is not ideal for CT image acquisition and localization to target sites (e.g., tumor). This issue can be overcome by using polymers or lipids that can initially hold the small nanoparticles together in larger-sized entities and slowly degrade over time. We demonstrated this with PCPP polymers in PMNP formulations; however, other biodegradable polymers, such as poly lactic-co-glycolic acid (PLGA) or chitosan, can be explored.^{5,6} Beside polymers, lipid structures (e.g., micelles and liposomes) can be formed to pack small nanoparticles into larger nanoparticles. As an example, Higbee-Dempsey et al. developed pH-sensitive gold-loaded polymeric micelles that can be destabilized and release the small gold nanoparticles in acidic environments.⁷ With improving designs of nanoparticle formulations and discoveries of nanoparticles made of novel heavy elements, clinical translation of nanoparticle contrast agents for CT and SPCCT imaging seems favorable.

Although it still may be a long process for them to get to FDA approval, these experimental contrast agents would especially benefit SPCCT imaging by taking advantage of its full potential for K-edge imaging, producing higher CNR and providing clearer material decomposition from the underlying tissue (e.g., bones). For this to happen, more comprehensive studies will need to be completed in order to evaluate the long-term safety of novel agents. The most promising elements for the development of SPCCT-specific contrast agents are gold, tantalum, ytterbium, bismuth, and gadolinium. Gold has been the most extensively studied element for its use as a nanoparticle-based SPCCT contrast agent, and its biocompatibility and high-contrast generation have already been demonstrated in small animals. However, its high cost could limit its potential uses. Tantalum and ytterbium both have K-edge energies near the mean photon energy spectrum, which can lead to higher CNR production.⁸ The efficacy in X-ray CT imaging and the biocompatibility of nanoparticle formulations that are based on these two elements have also been demonstrated in several studies.⁹⁻¹¹ However, the safety profiles of agents based on both of these elements are still poorly understood and more comprehensive studies are needed in order to consider clinical use. Bismuth's high K-edge energy is considerably greater than the mean photon energy of spectra typically used, which is a disadvantage when considering its use as a SPCCT contrast agent. Yet, because of its chemical inertness and affordability, it may continue to gather significant interest. Gadolinium has been broadly studied for its delineation from other elements in phantom imaging due to the fact that its chelates are already FDA approved for MRI. Because of this, gadolinium chelates have potential to be used for SPCCT imaging applications as well, although recent findings of their retention in brains and other organs raise a concern.¹²

Potentially the most attractive novel SPCCT agent for clinical translation would be a vascular agent that is based on a higher Z element than iodine (to allow its detection *via* K-edge imaging and to allow it to be distinguished from iodine agents, so that both iodine and the novel agent can be simultaneously imaged). In addition, longer lasting vascular contrast, such as larger nanoparticles that breaks down to smaller nanoparticles as described earlier would address a shortcoming of the currently FDA-approved iodinated agents, that is, very rapid blood clearance and therefore very narrow imaging window. Nanoparticles or other types of structures in the 1-5 nm size range can also still address the shortcomings as well, since they still should have longer circulation times than iodine-based small molecules due to less extravasation and larger size.

6.1.3 Expanding CT applications: targeted CT and SPCCT imaging

In our work, we demonstrated high accumulation of CeONP at the inflammation site *via* passive targeting, despite its ultrasmall size. By designing our nanoparticles to have initial sizes in the range of 5 to 200 nm, we can further promote the nanoparticle accumulation to the diseased sites, such as tumor and inflammation, from the EPR (enhanced permeability and retention) effect while escaping filtration by the RES organs.¹³ This will allow us to do targeted imaging with both CT and SPCCT, which can provide a significant diagnostic value.

Targeted accumulation of nanoparticles *via* passive targeting for CT imaging has been demonstrated in numerous studies so far, especially for tumor imaging. Findings from a study by Smilowitz *et al.* suggests that it may be feasible for 15 nm AuNP to accumulate in intracerebral tumor masses by injecting the nanoparticles intravenously as determined from a rat glioma model.¹⁴ Another study by Ashton *et al.* also investigated

and demonstrated that PEGylated, 30 nm AuNP can have high tumor accumulation *via* passive targeting, although a large amount was also detected in liver and spleen.¹⁵ In imaging with dual-energy CT, the authors also showed that iodinated contrast agents and AuNP could be accurately separated from one another *in vivo*, validating that developing nanoparticles from elements of high atomic number can lead to its material differentiation from both iodine and soft tissues.

Targeted CT imaging can also benefit from the development of nanoparticles that can actively target specific sites *via* functionalization of the nanoparticle surface with targeting moieties, such as antibodies. binding to specific surface markers of tumor cells, for example. A study by Hainfeld *et al.* demonstrated the feasibility of improving the specificity of AuNP tumor accumulation by conjugating anti-Her2 antibody on 15 nm AuNP. Upon intravenous injection, 16 % of AuNP accumulated to subcutaneously inoculated human Her2+ breast tumors, which allowed successful detection of tumor masses as small as 1.5 mm in thickness in micro-CT imaging.¹⁶ Peptides can also be conjugated onto the nanoparticle surfaces to promote accumulation in the brain, which is difficult to achieve due to the blood-brain barrier (BBB). Bao *et al.* conjugated angiopep-2 oligopeptide to facilitate BBB penetration of sub-5 nm CeONP *via* receptor-mediated transport.¹⁷ The authors demonstrated that CeONP helped treat and protect the brain against stroke induced by ischemic injury after crossing the BBB. Although CT imaging was not performed in this specific example, the amount of accumulation in the brain was enough that detection *via* CT imaging should be possible, which indicates the potential of utilizing CeONP as a theranostic agent for disorders in the brain (e.g., Alzheimer's and Parkinson's).

Nanoparticle-guided targeted imaging is not limited to vascular contrast agents; inflammation sites in the gastrointestinal tract can be detected in CT imaging by oral intake of nanoparticle contrast agents. Naha *et al.* recently demonstrated that it is possible to selectively image inflammation sites in the large intestines in colitis animal models with dextran coated cerium oxide nanoparticles (Dex-CeNP).¹⁸ After an oral administration of Dex-CeNP, a significant amount of the nanoparticles were accumulated in the colitis area while the rest were cleared out from the body at 24 h post-injection, clearly visualizing the inflammation site.

6.1.4 Expanding CT applications: cell tracking

Thus far, the use of CT for cell tracking has been limited, due in part to the low sensitivity of CT, requiring internalization of high payloads in the cells (hundreds of pg/cell) to produce sufficient attenuation for detection.¹⁹ This need for very high contrast agent payloads increases the possibility of affecting cell *viability* or function, which could result in misleading observations of cell migration and fate in the body. Furthermore, at such high concentrations, contrast agent that is released from the cells or is degraded could conceivably cause local tissue damage or systemic toxicity. Advances in nanoparticle formulations for cell labeling, as well as cell labeling techniques, could help address these issues. For example, techniques that have been used for labeling cells for other modalities, such as electroporation or antibody attachment, have not been explored. Furthermore, the development of new CT technology that allows better sensitivity and specificity of detection would be beneficial, and such technologies are emerging. For example, model-based iterative reconstruction techniques can suppress noise by a factor of 10, considerably increasing the sensitivity of contrast agent detection.²⁰ SPCCT

imaging in cell tracking can also eliminate the need for laborious and error-prone pre- and post-injection image analysis.²¹ In fact, the first study published a year ago used SPCCT imaging for cell tracking and demonstrated that the labeled cells can be monitored in a material-specific and quantitative manner with low detection limit of ~ 5000 cells in a voxel.²²

Recent studies of nanoparticle protein coronas and their effects on colloidal stability and on nanoparticle–cell interaction (i.e., internalization, intracellular transportation, cytotoxicity upon protein degradation) reveal the significance of surrounding the nanoparticles with the “right” composition of proteins.^{23,24} For cell tracking purposes, protein corona-dependent nanoparticle–cell interaction can be crucial to increase cellular uptake efficiency. Future studies may identify optimal protein compositions to improve cellular uptake while minimizing disruption of cell functionality. Improved uptake efficiency will also enable labeling of other non-phagocytic cells, besides CAR-T cells, such as epithelial cells, endothelial cells, and fibroblasts, to broaden CT cell tracking applications.

For CT cell tracking, AuNP are by far the most widely studied class of contrast agent for labeling cells, due to biocompatibility, easily tailorable size and surface chemistry, and high attenuation in CT.²⁵ A potential issue for gold contrast agents is their cost; however, when scaling up from the mouse, only around a gram of gold will be needed for *in vivo* cell tracking in patients. Since the current price of gold is about \$40/gram, CT cell tracking contrast agents based on this element will be affordable. Nevertheless, studies with labels synthesized from cheaper elements, such as cerium and tantalum, would be of great interest and could further reduce the price of CT cell tracking, given that we can formulate nanoparticles of high composition of the payload elements. Methods to

achieve nanoparticle clearance would be a further design improvement. For example, nanoparticles based on bismuth can be designed to degrade for eventual excretion.²⁶ SPCCT cell tracking will also allow simultaneous *in vivo* monitoring of multiple cell types by labeling them using contrast agents with different K-edge energies, which would further broaden the use of CT as a cell tracking imaging modality.

6.2 Future directions

6.2.1 Overview

In our work, we demonstrated the feasibility to develop specifically designed nanoparticles as SPCCT and CT imaging contrast agents (chapter 2 and 3) and for CT imaging applications of targeted imaging and cell tracking (chapter 3, 4, 5). Here, we discuss how we could expand on the findings in this work for potential future projects and the future direction of our CAR-T cell tracking work for *in vivo* monitoring.

6.2.2 Renally clearable CeONP as SPCCT contrast agents

As mentioned in our discussion, one of the biggest barriers in clinical translation of nanoparticle-based CT contrast agents is potential cytotoxic effects from long-term retention in the body.⁴ Our findings suggest that citric acid coated CeONP can be effectively cleared from the body *via* the kidneys pathway, which can reduce long-term cytotoxicity concerns. Moreover, cerium's K-edge energy at 40.4 keV is sufficiently distinguishable from that of iodine and is located in a high photon region, which results in high CT contrast generation, as demonstrated in chapter 3 and 4. This makes CeONP suitable for the development as SPCCT contrast agents. Moreover, cerium has advantages other than its favorable K-edge energy over other heavy metal elements that

are being investigated for contrast agent development (e.g., tantalum and ytterbium). These are CeONP's familiarity in biomedical research, its small core size, ease of bulk synthesis and its versatility in surface coating (i.e., PEG, citric acid, polyacrylic acid, ascorbic acid and other small molecules with carboxylic acid groups and hydroxy groups). Its antioxidant and immunomodulatory effects can potentially be utilized in simultaneous targeted CT imaging and treatment of inflammatory diseases, which include atherosclerosis, stroke, injuries in various organs (e.g., liver, kidney and brain), neurodegenerative diseases, as well as cancer. Using the capabilities of SPCCT imaging in quantification of exogenous contrast agents, it may also be possible to predict the outcome of CeONP treatment for aforementioned diseases from imaging alone.

6.2.3 *In vivo* CAR-T cell tracking in cancer immunotherapy

In our work in chapter 5, we have demonstrated the feasibility to label CAR-T cells with AuNP without disrupting the cell *viability* and cytotoxic and inflammatory functions *in vitro*. However, before moving the study forward to *in vivo* studies, we would like to confirm that other cellular functions have not been disturbed significantly from AuNP labeling. We will first evaluate proliferation, which a critical mechanism that is directly correlated to the persistence and efficacy of the therapy. For this assessment, we will stain labeled and unlabeled cells with carboxyfluorescein succinimidyl ester and be allowed to incubate for 1, 3 and 5 days in cell culture medium with CD3/CD28 Dynabeads. At each timepoint, the cells will be collected and fixed for flow cytometry analysis. We will also assess migration of the labeled cells to confirm that their ability to localize and penetrate the tumor mass is not affected by examining the migratory behavior in Chemotaxis plate.

In vivo tracking of AuNP-labeled CAR-T cells will be performed in a murine orthotopic model of human breast cancer to test the feasibility using SPCCT imaging for CAR-T cell tracking. Specifically, we will monitor 5E5 CAR-T cells (gifted by Dr. Avery Posey) that target Tn-MUC1 (an aberrantly glycosylated MUC1 epitope) found in most adenocarcinomas, including breast cancers.^{27, 28} The accuracy in differentiation and quantification of AuNP labeled cells in SPCCT imaging will be assessed and corroborated by *ex vivo* analyses such as ICP-OES and electron microscopy. The antitumor therapeutic efficacy and cytotoxicity of labeled CAR-T cells also will be examined and correlated with the biodistribution at different times points as determined by SPCCT imaging.

6.3 Concluding remarks

The findings in this work highlight some of the most important criteria in the development of CT and SPCCT-specific contrast agents and the potential use of these nanoparticles beyond blood pool contrast agents for broadening CT imaging applications. Simultaneously, the use of numerous core elements, coating materials and encapsulating components reflect the versatility of nanoparticles that will allow them to be continuously explored for various CT imaging and other biomedical applications. With ever-growing research interest in nanotechnology and newly emerging CT technologies, nanoparticles will play a significant role in CT diagnostics in the future.

6.4 References

1. Hirst, S. M.; Karakoti, A. S.; Tyler, R. D.; Sriranganathan, N.; Seal, S.; Reilly, C. M., Anti-inflammatory properties of cerium oxide nanoparticles. *Small* **2009**, *5* (24), 2848-2856.
2. Jeong, H. G.; Cha, B. G.; Kang, D. W.; Kim, D. Y.; Yang, W.; Ki, S. K.; Kim, S. I.; Han, J.; Kim, C. K.; Kim, J.; Lee, S. H., Ceria nanoparticles fabricated with 6-aminohexanoic acid that overcome systemic inflammatory response syndrome. *Adv Healthc Mater* **2019**, *8* (9), e1801548.
3. Ni, D.; Wei, H.; Chen, W.; Bao, Q.; Rosenkrans, Z. T.; Barnhart, T. E.; Ferreira, C. A.; Wang, Y.; Yao, H.; Sun, T.; Jiang, D.; Li, S.; Cao, T.; Liu, Z.; Engle, J. W.; Hu, P.; Lan, X.; Cai, W., Ceria nanoparticles meet hepatic ischemia-reperfusion injury: the perfect imperfection. *Adv Mater* **2019**, *31* (40), 1902956.
4. Soo Choi, H.; Liu, W.; Misra, P.; Tanaka, E.; Zimmer, J. P.; Itty Ipe, B.; Bawendi, M. G.; Frangioni, J. V., Renal clearance of quantum dots. *Nat Biotechnol* **2007**, *25* (10), 1165-1170.
5. Landriscina, A.; Rosen, J.; Friedman, A. J., Biodegradable chitosan nanoparticles in drug delivery for infectious disease. *Nanomedicine (Lond)* **2015**, *10* (10), 1609-1619.
6. Rezvantalab, S.; Drude, N. I.; Moraveji, M. K.; Güvener, N.; Koons, E. K.; Shi, Y.; Lammers, T.; Kiessling, F., PLGA-based nanoparticles in cancer treatment. *Front Pharmacol* **2018**, *9* (1260).
7. Higbee-Dempsey, E. M.; Amirshaghghi, A.; Case, M. J.; Bouché, M.; Kim, J.; Cormode, D. P.; Tsourkas, A., Biodegradable gold nanoclusters with improved excretion due to pH-triggered hydrophobic-to-hydrophilic transition. *J Am Chem Soc* **2020**, *142* (17), 7783-7794.

8. Kim, J.; Bar-Ness, D.; Si-Mohamed, S.; Coulon, P.; Blevis, I.; Douek, P.; Cormode, D. P., Assessment of candidate elements for development of spectral photon-counting CT specific contrast agents. *Sci Rep* **2018**, *8* (1), 12119.
9. Liu, Y.; Ai, K.; Liu, J.; Yuan, Q.; He, Y.; Lu, L., A high-performance ytterbium-based nanoparticulate contrast agent for *in vivo* X-ray computed tomography Imaging. *Angew Chem Int Ed* **2012**, *51* (6), 1437-1442.
10. Oh, M. H.; Lee, N.; Kim, H.; Park, S. P.; Piao, Y.; Lee, J.; Jun, S. W.; Moon, W. K.; Choi, S. H.; Hyeon, T., Large-scale synthesis of bioinert tantalum oxide nanoparticles for X-ray computed tomography imaging and bimodal image-guided sentinel lymph node mapping. *J Am Chem Soc* **2011**, *133* (14), 5508-5515.
11. FitzGerald, P. F.; Butts, M. D.; Roberts, J. C.; Colborn, R. E.; Torres, A. S.; Lee, B. D.; Yeh, B. M.; Bonitatibus, P. J., Jr., A proposed computed tomography contrast agent using carboxybetaine zwitterionic tantalum oxide nanoparticles: imaging, biological, and physicochemical performance. *Invest Radiol* **2016**, *51* (12), 786-796.
12. Rogosnitzky, M.; Branch, S., Gadolinium-based contrast agent toxicity: a review of known and proposed mechanisms. *Biometals* **2016**, *29* (3), 365-376.
13. Blanco, E.; Shen, H.; Ferrari, M., Principles of nanoparticle design for overcoming biological barriers to drug delivery. *Nat Biotechnol* **2015**, *33* (9), 941-951.
14. Smilowitz, H. M.; Meyers, A.; Rahman, K.; Dymant, N. A.; Sasso, D.; Xue, C.; Oliver, D. L.; Lichtler, A.; Deng, X.; Ridwan, S. M.; Tarmu, L. J.; Wu, Q.; Salner, A. L.; Bulsara, K. R.; Slatkin, D. N.; Hainfeld, J. F., Intravenously-injected gold nanoparticles (AuNPs) access intracerebral F98 rat gliomas better than AuNPs infused directly into the tumor site by convection enhanced delivery. *Int J Nanomedicine* **2018**, *13*, 3937-3948.

15. Ashton, J. R.; Clark, D. P.; Moding, E. J.; Ghaghada, K.; Kirsch, D. G.; West, J. L.; Badea, C. T., Dual-energy micro-CT functional imaging of primary lung cancer in mice using gold and iodine nanoparticle contrast agents: a validation study. *PLoS One* **2014**, *9* (2), e88129.
16. Hainfeld, J. F.; O'Connor, M. J.; Dilmanian, F. A.; Slatkin, D. N.; Adams, D. J.; Smilowitz, H. M., Micro-CT enables microlocalisation and quantification of Her2-targeted gold nanoparticles within tumour regions. *Br J Radiol* **2011**, *84* (1002), 526-533.
17. Bao, Q.; Hu, P.; Xu, Y.; Cheng, T.; Wei, C.; Pan, L.; Shi, J., Simultaneous blood-brain barrier crossing and protection for stroke treatment based on edaravone-loaded ceria nanoparticles. *ACS Nano* **2018**, *12* (7), 6794-6805.
18. Naha, P. C.; Hsu, J. C.; Kim, J.; Shah, S.; Bouché, M.; Si-Mohamed, S.; Rosario-Berrios, D. N.; Douek, P.; Hajfathalian, M.; Yasini, P.; Singh, S.; Rosen, M. A.; Morgan, M. A.; Cormode, D. P., Dextran-coated ceriumoxide nanoparticles: a computed tomography contrast agent for imaging the gastrointestinal tract and inflammatory bowel disease. *ACS Nano* **2020**, *14* (8), 10187-10197.
19. Chhour, P.; Kim, J.; Benardo, B.; Tovar, A.; Mian, S.; Litt, H. I.; Ferrari, V. A.; Cormode, D. P., Effect of gold nanoparticle size and coating on labeling monocytes for CT tracking. *Bioconjug Chem* **2017**, *28* (1), 260-269.
20. Bernstein, A. L.; Dhanantwari, A.; Jurcova, M.; Cheheltani, R.; Naha, P. C.; Ivanc, T.; Shefer, E.; Cormode, D. P., Improved sensitivity of computed tomography towards iodine and gold nanoparticle contrast agents *via* iterative reconstruction methods. *Sci Rep* **2016**, *6*, 26177.
21. Muenzel, D.; Bar-Ness, D.; Roessl, E.; Blevis, I.; Bartels, M.; Fingerle, A. A.; Ruschke, S.; Coulon, P.; Daerr, H.; Kopp, F. K.; Brendel, B.; Thran, A.; Rokni, M.;

- Herzen, J.; Boussel, L.; Pfeiffer, F.; Proksa, R.; Rummeny, E. J.; Douek, P.; Noël, P. B., Spectral photon-counting CT: initial experience with dual-contrast agent K-edge colonography. *Radiology* **2017**, *283* (3), 723-728.
22. Cuccione, E.; Chhour, P.; Si-Mohamed, S.; Dumot, C.; Kim, J.; Hubert, V.; Da Silva, C. C.; Vandamme, M.; Chereul, E.; Balegamire, J.; Chevalier, Y.; Berthezène, Y.; Boussel, L.; Douek, P.; Cormode, D. P.; Wiart, M., Multicolor spectral photon counting CT monitors and quantifies therapeutic cells and their encapsulating scaffold in a model of brain damage. *Nanotheranostics* **2020**, *4* (3), 129-141.
23. Mirshafiee, V.; Kim, R.; Park, S.; Mahmoudi, M.; Kraft, M. L., Impact of protein pre-coating on the protein corona composition and nanoparticle cellular uptake. *Biomaterials* **2016**, *75*, 295-304.
24. Wan, S.; Kelly, P. M.; Mahon, E.; Stöckmann, H.; Rudd, P. M.; Caruso, F.; Dawson, K. A.; Yan, Y.; Monopoli, M. P., The "sweet" side of the protein corona: effects of glycosylation on nanoparticle-cell interactions. *ACS Nano* **2015**, *9* (2), 2157-2166.
25. Mieszawska, A. J.; Mulder, W. J.; Fayad, Z. A.; Cormode, D. P., Multifunctional gold nanoparticles for diagnosis and therapy of disease. *Mol Pharm* **2013**, *10* (3), 831-847.
26. Swy, E. R.; Schwartz-Duval, A. S.; Shuboni, D. D.; Latourette, M. T.; Mallet, C. L.; Parys, M.; Cormode, D. P.; Shapiro, E. M., Dual-modality, fluorescent, PLGA encapsulated bismuth nanoparticles for molecular and cellular fluorescence imaging and computed tomography. *Nanoscale* **2014**, *6* (21), 13104-13112.
27. Lavrsen, K.; Madsen, C. B.; Rasch, M. G.; Woetmann, A.; Ødum, N.; Mandel, U.; Clausen, H.; Pedersen, A. E.; Wandall, H. H., Aberrantly glycosylated MUC1 is

expressed on the surface of breast cancer cells and a target for antibody-dependent cell-mediated cytotoxicity. *Glycoconj J* **2013**, *30* (3), 227-236.

28. Posey, A. D., Jr.; Schwab, R. D.; Boesteanu, A. C.; Steentoft, C.; Mandel, U.; Engels, B.; Stone, J. D.; Madsen, T. D.; Schreiber, K.; Haines, K. M.; Cogdill, A. P.; Chen, T. J.; Song, D.; Scholler, J.; Kranz, D. M.; Feldman, M. D.; Young, R.; Keith, B.; Schreiber, H.; Clausen, H.; Johnson, L. A.; June, C. H., Engineered CAR T cells targeting the cancer-associated Tn-glycoform of the membrane mucin MUC1 control adenocarcinoma. *Immunity* **2016**, *44* (6), 1444-1454.

LIST OF PUBLICATION

- Shapira N, Scheuermann J, Perkins AE, Kim J, Liu LP, Karp JS, Noël PB. (2021) Quantitative positron emission tomography imaging in the presence of iodinated contrast media using electron density quantifications from dual-energy computed tomography. *Medical Physics*. 48(1): 273 – 286.
- Naha P, Hsu JC, Kim J, Shah S, Bouché M, Si-mohamed S, Rosario-Berrios DN, Douek P, Hajfathalian M, Yasini P, Singh S, Rosen MA, Morgan MA, Cormode DP. (2020) Dextran coated cerium oxide nanoparticles: a computed tomography contrast agent for imaging the gastrointestinal tract and inflammatory bowel disease. *ACS Nano*. 14(8): 10187–10197.
- Higbee-Dempsey EM, Amirshaghghi A, Case MJ, Bouché M, Kim J, Cormode DP, Tsourkas A. (2020) Biodegradable gold nanoclusters with improved excretion due to pH-triggered hydrophobic-to-hydrophilic transition. *Journal of American Chemical Society*. 142(17): 7783 – 7794.
- Cuccione E, Chhour P, Si-Mohamed S, Dumot C, Kim J, Violaine H, Crola Da Silva C, Vandamme M, Chereul E, Balegamire J, Chevalier Y, Berthezène Y, Bousset L, Douek P, Cormode DP, Wiart M. (2020) Multicolor spectral photon-counting CT monitors and quantifies therapeutic cells and their encapsulating scaffold in a model of brain damage. *Nanotheranostics*. 4(3):129-141.
- Kim J, Naha P, Cormode DP. (2020) Contrast agents for spectral photon counting computed tomography. Book Chapter in *Spectral Computed Tomography: Technology and Applications*. CRC Press. pp 139-156.

- Bouché M, Hsu JC, Dong Y, Kim J, Taking K, Cormode DP. (2019) Recent advances in molecular imaging with gold nanoparticles. *Bioconjugate chemistry*. 31(2): 303 – 314.
- Kim J, Silva A, Hsu JC, Maidment PN, Shapira N, Noël PB, Cormode DP. (2019) Radioprotective garment-inspired biodegradable polymetal nanoparticles for enhanced CT contrast production. *Chemistry of Materials*. 32(1): 381–391.
- Hsu JC, Cruz E, Naha P, Lau K, Bouché M, Kim J, Maidment A, Cormode DP. (2019) Renally excretable and size-tunable silver sulfide nanoparticles for dual-energy mammography or computed tomography. *Chemistry of Materials*. 31(19): 7845 – 7854.
- Dong Y, Hajfathalian M, Maidment PN, Hsu JC, Naha P, Si-Mohamed S, Breuilly M, Kim J, Chhour P, Douek P, Litt HI, Cormode DP. (2019) Effect of gold nanoparticle size on their properties as contrast agents for computed tomography. *Scientific Reports*, 9, 14912.
- Kim J, Bar-Ness D, Si-Mohamed S, Coulon P, Blevis I, Douek P, Cormode DP. (2018) Assessment of candidate elements for development of spectral photon-counting CT specific contrast agents. *Scientific Reports*. 8, 12119.
- Guo L, Akahori H, Harari E, Smith SL, Polavarapu R, Karmali V, Otsuka F, Gannon RL, Braumann RE, Dickinson MH, Gupta A, Jenkins AL, Lipinski MJ, Kim J, Chhour P, de Vries PS, Jinnouchi H, Kutys R, Mori H, Kutyna MD, Torii S, Sakamoto A, Choi CU, Cheng Q, Grove ML, Sawan MA, Zhang Y, Cao Y, Kolodgie FD, Cormode DP, Arking DE, Boerwinkle E, Morrison AC, Erdmann J, Sotodehnia N, Virmani R, Finn AV. (2018) CD163⁺ macrophages promote angiogenesis and vascular permeability

accompanied by inflammation in atherosclerosis. *Journal of Clinical Investigation*. 128(3): 1106–1124.

- Cheheltani R, Kim J, Cormode DP. (2018) Nanoparticle Contrast Agents for Medical Imaging. Book chapter in *Nanobiotechnology: Human Health and the Environment*. CRC Press. pp 219–250.
- Kim J, Chhour P, Hsu JC, Litt HI, Ferrari VA, Popovtzer R, Cormode DP. (2017) Use of nanoparticle contrast agents for cell tracking with computed tomography. *Bioconjugate Chemistry*. 28(6): 1581–1597.
- Chhour P, Kim J, Benardo B, Tovar A, Mian S, Litt HI, Ferrari VA, Cormode DP. (2017) Effect of gold nanoparticle size and coating on labeling monocytes for CT tracking. *Bioconjugate Chemistry*, 28(1): 260-269.
- Cheheltani R, Ezzibdeh RM, Chhour P, Chandrika K, **Kim J**, Jurcova M, Hsu JC, Blundell C, Litt HI, Ferrari VA, Allcock HA, Sehgal CM, Cormode DP. (2016) Tunable, biodegradable gold nanoparticles as contrast agents for computed tomography and photoacoustic imaging. *Biomaterials*. 102, 87-97.